BEILSTEIN JOURNAL OF NANOTECHNOLOGY

Microneedles for vaccination and drug delivery

Edited by Philip Prewett, Graham Davies and Zahra Faraji Rad

Generated on 09 November 2026, 00:20

Imprint

Beilstein Journal of Nanotechnology
www.bjnano.org
ISSN 2190-4286
Email: journals-support@beilstein-institut.de

The *Beilstein Journal of Nanotechnology* is published by the Beilstein-Institut zur Förderung der Chemischen Wissenschaften.

Beilstein-Institut zur Förderung der Chemischen Wissenschaften
Trakehner Straße 7–9
60487 Frankfurt am Main
Germany
www.beilstein-institut.de

The copyright to this document as a whole, which is published in the *Beilstein Journal of Nanotechnology*, is held by the Beilstein-Institut zur Förderung der Chemischen Wissenschaften. The copyright to the individual articles in this document is held by the respective authors, subject to a Creative Commons Attribution license.

BEILSTEIN JOURNAL OF NANOTECHNOLOGY

Microneedle patches – the future of drug delivery and vaccination?

Zahra Faraji Rad[1], Philip D. Prewett*[2,3] and Graham J. Davies[4,5]

Editorial

Open Access

Address:
[1]School of Mechanical and Electrical Engineering, University of Southern Queensland, Springfield Central, QLD 4300, Australia, [2]Department of Mechanical Engineering, University of Birmingham, Birmingham B15 2TT, United Kingdom, [3]Oxacus Ltd, Dorchester-on-Thames, OX10 7HN, United Kingdom, [4]Faculty of Engineering, UNSW Sydney, Sydney, NSW 2052, Australia and [5]College of Engineering & Physical Sciences, School of Engineering, University of Birmingham, Birmingham, B15 2TT, United Kingdom

Email:
Philip D. Prewett* - p.d.prewett@oxscicon.co.uk

* Corresponding author

Beilstein J. Nanotechnol. **2023,** *14,* 494–495.
https://doi.org/10.3762/bjnano.14.40

Received: 27 March 2023
Accepted: 05 April 2023
Published: 14 April 2023

This article is part of the thematic issue "Microneedles for vaccination and drug delivery".

Editor-in-Chief: G. Wilde

© 2023 Faraji Rad et al.; licensee Beilstein-Institut.
License and terms: see end of document.

Hypodermic needles and cannulas have been in clinical use since the 17th century. The first bevelled metal hypodermic needles were introduced by Francis Reed in 1844, followed by the syringe and needle combination, due to Alexander Wood, in 1853. Needles for a single intravenous dose (IV push) or bolus normally use a fixed intravenous hollow needle. Hypodermic syringe injections are, of course, ubiquitous in modern medicine for drug therapy and vaccination, where oral administration is either not desirable or not possible. Delivery may be intravenous, intramuscular or percutaneous. Hypodermic needles of various dimensions are also used to extract venous blood for diagnostic tests. Other tests, such as blood glucose monitoring in diabetics [1], release blood by a pinprick from the capillaries immediately beneath the skin.

Microneedles (MNs), typically less than 1 mm long, are a late 20th century development with significant promise for the above applications [2]. Recent research has also revealed a growing interest in diagnostic testing using the interstitial fluid (ISF) transdermally extracted, for example using suction devices [3], and there is increasing recognition by doctors and biomedical scientists of the potential role of the ISF in medical diagnostics. Microneedles provide shallow transdermal access to the ISF and are an excellent match to these and other developments when integrated into arrays on a substrate to form a patch.

The possibility of inexpensive mass-manufactured MN patches for drug delivery, vaccination, and diagnostic testing is a highly desirable clinical objective for the above reasons. They have the added advantage of being short, not stimulating nerve endings, therefore painless in use and attractive for patients prone to needle phobia. Indeed, patient self-administration is an option.

The commercial availability at scale of inexpensive disposable MN patches has been heralded for some years as a paradigm shift. Patches without MNs are already used for analgesic and anti-inflammatory treatments, nicotine addiction, and hormone replacement therapies. However, the combination of drug-loaded patches with MNs is still in its infancy, and MN patch

diagnostic systems barely appear on the research landscape. Microneedle vaccination patches are closer to clinical acceptance and have enormous promise, given the demand for high volume, low cost, rapidly deployable vaccination in response to pandemics like COVID-19 [4], and companies dedicated to MN patch vaccination are already established. The key to the future of MN patches is the development and commercial availability of reliable, inexpensive, and biocompatible MNs with regulatory approval for clinical use.

The earliest MNs were made by adapting microfabrication technology originally developed for the microelectronics industry; they were inevitably made from silicon. Since then, silicon MNs have been largely abandoned in favour of polymer versions because of their superior mechanical properties, biocompatibility, ease of manufacture, and ultimate scalability [5,6]. Polymer MNs tailored to penetrate the skin and provide access to blood capillaries or the ISF have been the subject of a rapidly growing number of research publications over the last decade, and the trend continues [7]. Several key issues discussed in these papers are also considered in this thematic issue [8,9]. Recent progress may be broadly categorised as MN design, fabrication, skin penetration studies, and applications, ranging from drug delivery and vaccination to diagnostics. The first two of these have received most attention, but considerable work is still to be done in all categories – more in vivo studies for example. In the meantime, progress towards large-scale manufacture of moulded polymer MNs is progressing at pace, with the aid of new advanced 3D mould fabrication tools [10].

This special edition provides a snapshot of current research into MNs and their applications. It focuses on vaccination and drug delivery, but there is growing evidence of future potential in diagnostics and even in plant science [11]. If the thematic issue helps to inform existing researchers and to encourage others to join them, as editors, we will meet our objectives, the ultimate goal being the acceptance and availability of regulatory-approved MN patches for a wide range of clinical and biomedical applications.

We are grateful to the authors for their excellent contributions to this thematic issue; we are very aware of the demands on their time. We also thank the Beilstein-Institut editorial team for their highly professional support and the editorial board for approving this thematic issue.

Zahra Faraji Rad, Philip Prewett, and Graham Davies

Springfield, Birmingham and Sydney, March 2023

ORCID® iDs

Zahra Faraji Rad - https://orcid.org/0000-0001-6528-5965

References

1. Liu, Y.; Yu, Q.; Luo, X.; Yang, L.; Cui, Y. *Microsyst. Nanoeng.* **2021,** *7,* 75. doi:10.1038/s41378-021-00302-w
2. Faraji Rad, Z.; Prewett, P. D.; Davies, G. J. *Beilstein J. Nanotechnol.* **2021,** *12,* 1034–1046. doi:10.3762/bjnano.12.77
3. Saifullah, K. M.; Faraji Rad, Z. *Adv. Mater. Interfaces* **2023,** *10,* 2201763. doi:10.1002/admi.202201763
4. Yin, Y.; Su, W.; Zhang, J.; Huang, W.; Li, X.; Ma, H.; Tan, M.; Song, H.; Cao, G.; Yu, S.; Yu, D.; Jeong, J. H.; Zhao, X.; Li, H.; Nie, G.; Wang, H. *ACS Nano* **2021,** *15,* 14347–14359. doi:10.1021/acsnano.1c03252
5. Ebrahiminejad, V.; Faraji Rad, Z.; Prewett, P. D.; Davies, G. J. *Beilstein J. Nanotechnol.* **2022,** *13,* 629–640. doi:10.3762/bjnano.13.55
6. Malek-Khatabi, A.; Faraji Rad, Z.; Rad-Malekshahi, M.; Akbarijavar, H. *Mater. Lett.* **2023,** *330,* 133328. doi:10.1016/j.matlet.2022.133328
7. Ahmed Saeed AL-Japairai, K.; Mahmood, S.; Hamed Almurisi, S.; Reddy Venugopal, J.; Rebhi Hilles, A.; Azmana, M.; Raman, S. *Int. J. Pharm.* **2020,** *587,* 119673. doi:10.1016/j.ijpharm.2020.119673
8. Gadziński, P.; Froelich, A.; Wojtyłko, M.; Białek, A.; Krysztofiak, J.; Osmałek, T. *Beilstein J. Nanotechnol.* **2022,** *13,* 1167–1184. doi:10.3762/bjnano.13.98
9. Abdelghany, S.; Alshaer, W.; Al Thaher, Y.; Al Fawares, M.; Al-Bakri, A. G.; Zuriekat, S.; Mansour, R. S. *Beilstein J. Nanotechnol.* **2022,** *13,* 517–527. doi:10.3762/bjnano.13.43
10. Faraji Rad, Z.; Prewett, P. D.; Davies, G. J. *Addit. Manuf.* **2022,** *56,* 102953. doi:10.1016/j.addma.2022.102953
11. Faraji Rad, Z. *Adv. Eng. Mater.* **2023,** *25,* 2201194. doi:10.1002/adem.202201194

License and Terms

This is an open access article licensed under the terms of the Beilstein-Institut Open Access License Agreement (https://www.beilstein-journals.org/bjnano/terms), which is identical to the Creative Commons Attribution 4.0 International License (https://creativecommons.org/licenses/by/4.0). The reuse of material under this license requires that the author(s), source and license are credited. Third-party material in this article could be subject to other licenses (typically indicated in the credit line), and in this case, users are required to obtain permission from the license holder to reuse the material.

The definitive version of this article is the electronic one which can be found at:
https://doi.org/10.3762/bjnano.14.40

BEILSTEIN JOURNAL OF NANOTECHNOLOGY

Design and characterization of polymeric microneedles containing extracts of Brazilian green propolis

Camila Felix Vecchi, Rafaela Said dos Santos, Jéssica Bassi da Silva and Marcos Luciano Bruschi*

Full Research Paper

Open Access

Address:
Laboratory of Research and Development of Drug Delivery Systems, Postgraduate Program in Pharmaceutical Sciences, Department of Pharmacy, State University of Maringa, Maringa, Brazil

Email:
Marcos Luciano Bruschi* - mlbruschi@uem.br

* Corresponding author

Keywords:
development; mechanical; microneedles; propolis extract; technology

Beilstein J. Nanotechnol. **2022,** *13,* 503–516.
https://doi.org/10.3762/bjnano.13.42

Received: 16 January 2022
Accepted: 17 May 2022
Published: 08 June 2022

This article is part of the thematic issue "Microneedles for vaccination and drug delivery".

Guest Editor: P. D. Prewett

© 2022 Vecchi et al.; licensee Beilstein-Institut.
License and terms: see end of document.

Abstract

Microneedles (MNs) are a means to break the protective skin barrier in a minimally invasive way. By creating temporary micropores, they make biologically active agents available in the skin layers. Propolis (PRP) is a gum resin with a complex chemical composition, produced by bees *Apis mellifera* L. and showing several therapeutic properties (i.e., antibacterial, antiviral, antifungal, anti-inflammatory, healing, and immunomodulatory properties). The administration of PRP extracts by conventional routes has some disadvantages, such as running off over the skin in liquid or emulsion form. When taken orally, the extracts have a strong and unpleasant taste. The aim of this work was to fabricate and characterize microneedles containing polyvinyl alcohol, polyvinylpyrrolidone, poloxamer P407, and an ethanolic or glycolic extract of PRP. Also, the obtained structures were microscopically and mechanically characterized. The results of the mechanical analysis showed that formulations containing 3% of P407 presented the highest compression values in a hard surface, which was also confirmed by the height and base values of the morphological analysis and by the microscopy images. It was possible to design MNs and select the best formulations for future tests. MNs containing an ethanolic extract of PRP showed to be better structured than MNs containing a glycolic extract of PRP. The MNs obtained in these studies proved to be a promising platform for the topical application of PRP.

Introduction

In recent decades, microneedle devices have been widely used for non-invasive dermal delivery of various drugs [1-3]. Microneedles (MNs) are large enough to penetrate and open small holes only in the stratum corneum and the viable epidermis, without reaching the nerve endings that are in the dermis [4,5]. The perforation of the stratum corneum enables

the release of bioactive molecules in the epidermis, which then reach the dermis and blood capillaries by diffusion [6]. This entire process occurs in a non-invasive, painless, and bleeding-free way [7]. MNs can be organized into single structures or arranged in small arrays to mediate the localized release of therapeutic molecules [8]. Regarding the design, MNs can be categorized into solid, hollow, dissolvable, and coated MNs, according to the differences in the permeation mechanism [6,9,10].

Nanocarriers can be used together with polymeric MNs in a synergistic therapy. The nanocarriers can immediately come into contact with the stratum corneum with the help of polymeric MNs, enhancing the transdermal drug delivery of the drugs. Furthermore, these polymeric MNs can encapsulate several types of nanocarriers, making it a unique system with different activities [11]. Solid MNs are used for pre-treatment of the skin. They serve only to create micropores, increasing permeability and facilitating the administration of the drug. The drug will be inserted over the holes created and will be taken, by diffusion, to the innermost layers to have its systemic action [5,12]. Coated microneedles are solid MNs made of inert material and coated with a formulation containing the drug to be administered [5,13]. After skin perforation, this lining is retained in the epidermis and, after a period, the MN system is removed [6].

Dissolvable MNs are composed of a biodegradable matrix containing the bioactive agent. When they come in contact with aqueous fluids in the skin, these needles dissolve, releasing the drug and degrading. As they are dissolvable, they do not need to be removed and do not generate residues, eliminating the risk of infections and local irritations when the microneedles are broken or incompletely removed. Hollow MNs have a reservoir inside, which contains the bioactive agent. They are used to penetrate the skin, inject their charge through the epidermis, and are later removed [6,14].

The application of MNs creates a transport pathway for the delivery of molecules, crossing external barriers that limit the introduction of molecules into the target tissue. Furthermore, MNs are very versatile and are considered less painful, less harmful, and more safe than conventional needles [5]. In general, MNs cause less damage than other larger, more invasive devices, such as hypodermic needles [15]. The creation of micropores is a physical technique that can be used to increase transdermal drug delivery by creating micropores in the stratum corneum before or during application, which can increase the permeation of certain molecules by up to 200 times [16]. In addition to being a minimally invasive route, transdermal drug delivery has low drug absorption variability among patients, since the cutaneous metabolism is significantly lower than the gastrointestinal one. Despite the great therapeutic potential, the use of this pathway is limited by the low permeation of molecules through the stratum corneum, the outermost layer of the skin, which works as a barrier, blocking the transport of drugs through the subcutaneous tissue. To overcome this difficulty, microneedles have been developed to cross the stratum corneum and enable the use of the transdermal route in different therapies [6].

Propolis (PRP) has already been studied in wound healing when incorporated in many vehicles, such as ointments, emulsions, hydrogels, films, or as hydroalcoholic or glycolic extracts. PRP exhibits important pharmacological activity, already proven in several studies, in addition to being a biologically safe compound [17-21]. This natural drug is also widely used as antimicrobial agent, immune system strengthener, and anticancer drug in the form of its ethanolic or glycolic extracts. It is a strongly adhesive gum resin, which is collected, processed, and used by honey bees (*Apis mellifera* L.) [17,22,23].

PRP extracts have been reported to enhance some antibiotic effects, attributing the antibacterial activity of propolis mainly to flavonoids or synergisms among some components [24]. The ethanol extract of PRP has several pharmacological activities, such as antiviral, antibacterial, antifungal, anti-inflammatory, anesthetic, cytostatic, hypotensive, and immunostimulatory properties [25]. Glycolic extracts can be an alternative in situations where the use of alcoholic extracts is inappropriate. Propylene glycol can be used as solvent, extractant, and preservative in a variety of pharmaceutical, cosmetic, and food formulations. It is compatible with several cosmetic and pharmaceutical bases, in addition to having an antiseptic capacity similar to that of ethanol and lower toxicity [26,27].

In our previous studies, polymeric systems composed of polyvinyl alcohol (PVA), polyvinylpyrrolidone (PVP), and poloxamer 407 (P407) were obtained and characterized. P407 could improve structuring and rapid dispersion of polymeric matrices, which showed promising physicochemical characteristics for potential application as nanostructured platforms for controlled drug delivery [28-30]. To our knowledge, MNs containing PRP have not been proposed before. Therefore, the aim of this study was to design microneedles composed of PVA, PVP, and P407 for the delivery of ethanolic or glycolic extracts of Brazilian green PRP. A 3^2 full-factorial design was utilized to determine the influence of P407 and PRP extract on the morphology and mechanical characteristics of MNs. They were characterized macroscopically, microscopically, and regarding size and texture, yielding an improved MN formulation for each type of PRP extract.

Results and Discussion

PRP quality assessment

The PRP sample was obtained from an apiary in the northwest region of Paraná. It had a characteristic aromatic odor, resin gum appearance, and a greenish-yellow color, very characteristic of the north and northeast regions of the states of Paraná, São Paulo, and Minas Gerais [31-33]. The PRP used had all suitable characteristics to be used in the following experiments.

Preparation of mold

When using polydimethylsiloxane (PDMS), the combination of base and catalyst resulted in a translucent mixture, which was easy to handle. However, there was intense formation of air bubbles. In order to reduce the bubbles in the final mold, the flask containing the mixture was placed in an ultrasonic bath and, subsequently, in a vacuum desiccator, until all bubbles were removed. With the mixture being completely clear, it was possible to insert the master structure for mold development (Supporting Information File 1, Figure S1). After 24 h, after the careful removal of the cartridge, a flexible mold was obtained, with intact and visible micropores, both on its surface and on its extension.

Fabrication of microneedles

After obtaining the 18 formulations, all were analyzed regarding structure integrity, formation of the 36 microneedles per patch, presence of air bubbles, and also the facility of removing from the mold. The MNs containing ethanolic extract of propolis (EE) showed more integrity and were easier to be removed from the mold. MNs containing glycolic extract (GE) were more difficult to remove from the mold, as there was an increase in the concentration of extract. The formulations containing 8% (w/w) GE did not result in MNs with good integrity, due to the high amount of propylene glycol, which yielded more malleable structures. Previous studies have shown that films containing PVA and propylene glycol are more malleable due to the breaking of hydrogen bonds by the effect of propylene glycol [34].

The factorial design chosen allowed us to evaluate the characteristics of the formulations containing different concentrations of EE and EG in addition to the concentration of P407. This made it possible to choose the best concentrations for each type of extract.

In previous studies carried out by Bruschi and colleagues, the concentrations of PRP extract that would have biological activity were studied. The ranges and concentrations used in this study were chosen so that the formulation obtained has a sufficient amount of PRP extract for biological activity [31,35,36].

Morphological analysis

The formulations could successfully replicate the master mold shape (Supporting Information File 1, Figure S2), and the obtained structures were macroscopically analyzed. Patches composed of 36 MNs with a spherical base and sharp tips were obtained for the majority of the formulations, mainly for those containing EE. All formulations were evaluated by optical and scanning electron microscopy for a better visualization of their structure. The micrographs obtained by optical microscopy for the all formulations are displayed in Figure 1 and Figure 2.

The micrographs show differences between MNs containing EE and those containing GE. The presence of EE resulted in MNs being more structured and firmer; however, from the images it can be seen that inside of each needle there are air bubbles or less deposits of extract. The MNs containing GE showed to be more malleable; they were more homogeneous in the dispersion of the extract; however, they also displayed air bubbles along the structure.

The morphological characteristics of the preparations were evaluated by SEM (Figure 3 and Figure 4), which confirmed the uniform and regular morphology of the needles. Micrographs of the formulations revealed polymeric fragments with well-defined, homogeneous structures, showing that the preparation used to obtain the structures was effective.

Micrographs obtained by scanning electron microscopy (Figure 3 and Figure 4) corroborate the results obtained from optical microscopy (Figure 1 and Figure 2), MNs containing EE demonstrated better structuring and MNs with GE demonstrated to be more malleable, with some being not formed at all (e.g., compare MNs E5 and G5, where the MNs in E5 are straight and without deformations, while the MNs in GE 5 have a malleable structure).

All formulations were analyzed regarding size. Base and height of MNs were determined to confirm the complete formation of each needle considering the total entry into the mold and characterized the size of the obtaining MNs. The measurements were taken from one of the 36 needles present in the patch (as shown below in Figure 7). The results of measurements for all MNs are shown in Table 1.

MNs containing EE were 1.78 ± 0.11 mm in height and 0.33 ± 0.01 mm in width of the base. The MNs containing GE were 1.56 ± 0.15 mm in height and 0.30 ± 0.02 mm in width of the base with smaller proportions due to the solvent affecting the formation of structures. There is a decrease of 10% and 22% in MN height, when EE and GE, respectively, are compared with the depth of the master mold. This is related to solvent evapora-

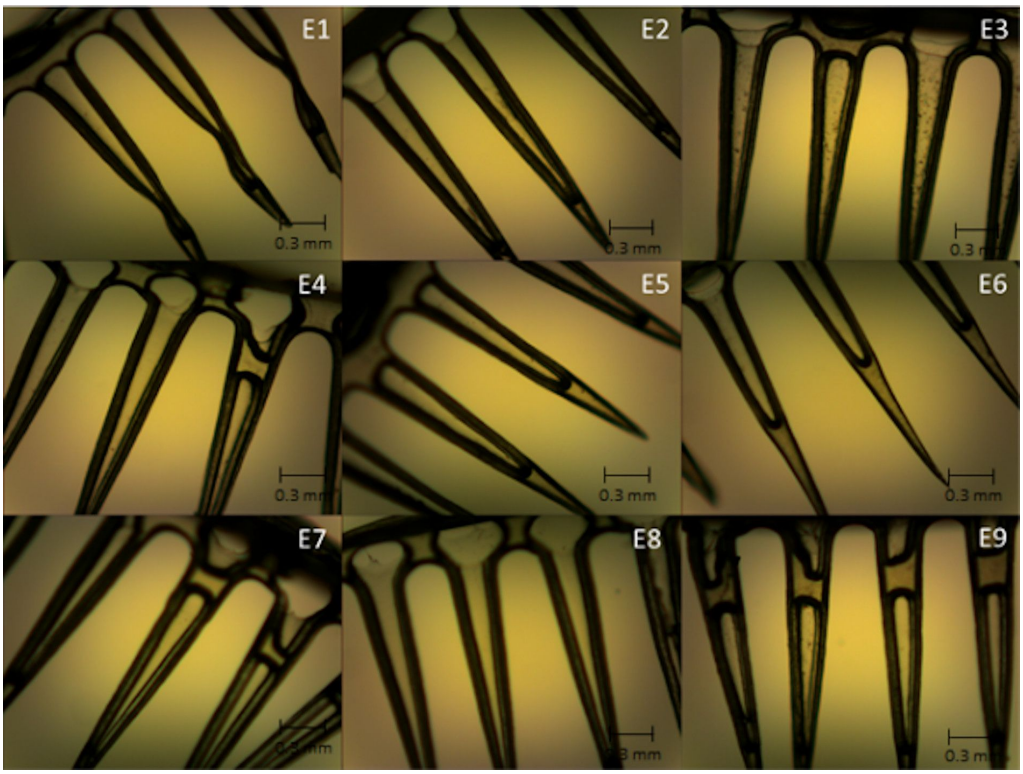


Figure 1: Micrographs obtained by optical microscopy showing the structure of the microneedles containing ethanolic extract of propolis (E1 to E9); magnification 40×.

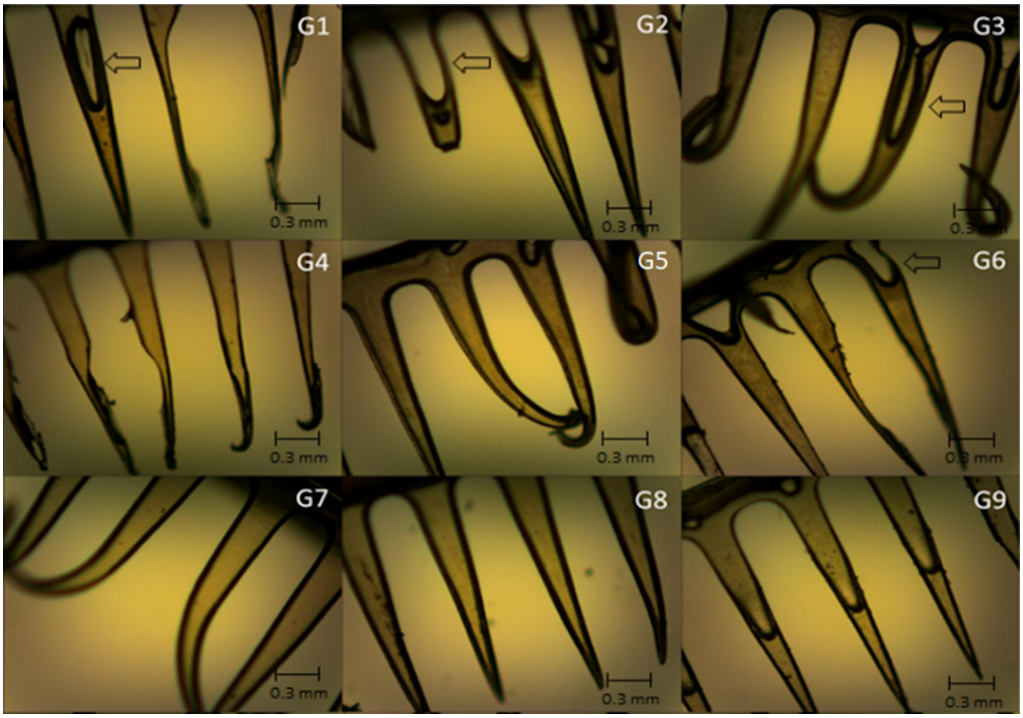


Figure 2: Micrographs obtained by optical microscopy showing the structure of microneedles containing glycolic extract of propolis (G1 to G9); magnification 40×. Arrows represent locations where bubbles are present.

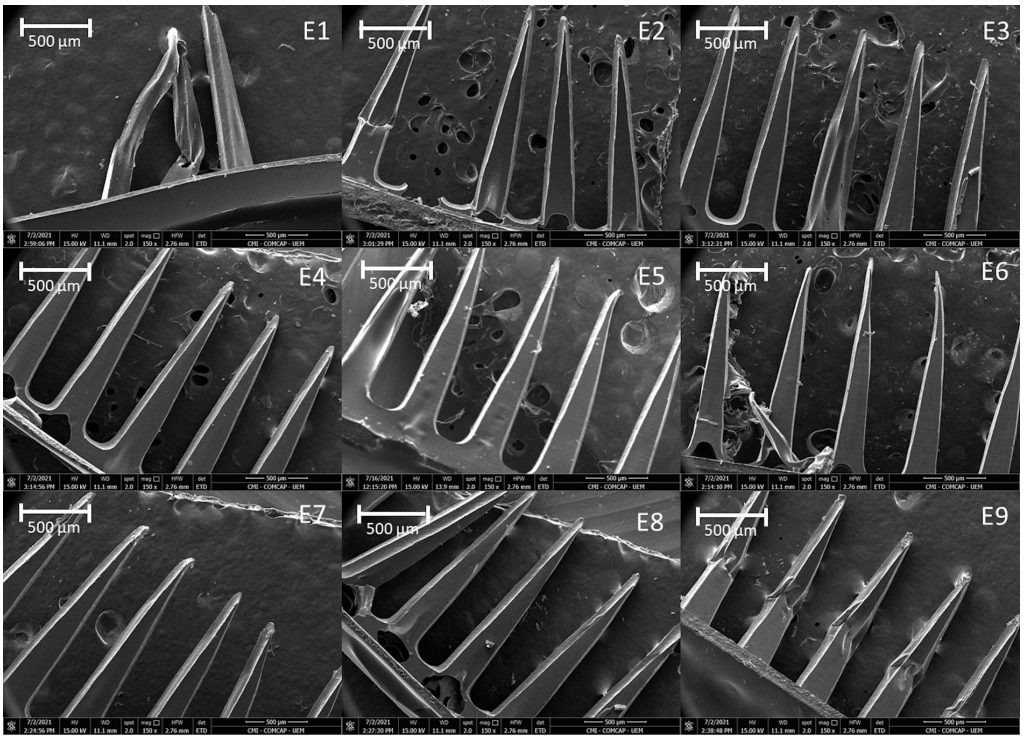


Figure 3: Micrographs obtained by scanning electron microscopy (SEM) showing the surface morphology microneedles containing ethanolic extract of propolis (E1 to E9); magnification 150×.

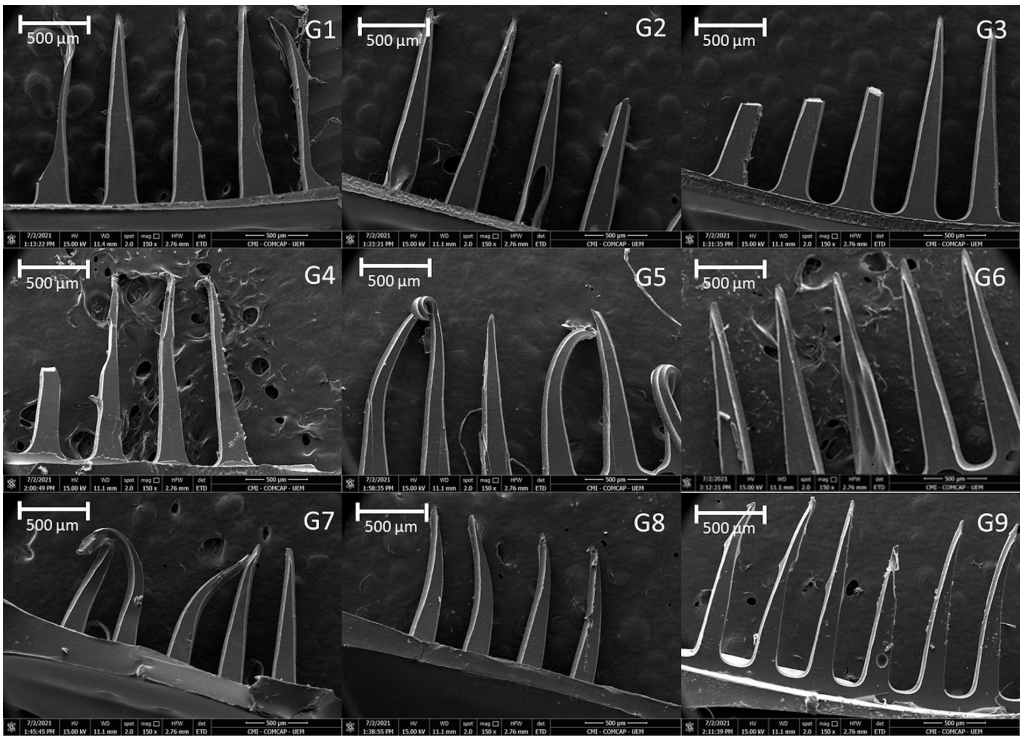


Figure 4: Micrograph obtained by scanning electron microscopy (SEM) showing the surface morphology of microneedles containing glycolic extract of propolis (G1 to G9); magnification 150×.

Table 1: Size analysis of microneedles containing ethanolic (EE) or glycolic extract (GE) of propolis.

EE			GE		
Formulation	Height (mm)	Base (mm)	Formulation	Height (mm)	Base (mm)
E1	1.6896 ± 0.0835	0.3471 ± 0.0029	G1	1.8310 ± 0.0305	0.3046 ± 0.0036
E2	1.8220 ± 0.0398	0.3109 ± 0.0080	G2	1.4469 ± 0.4359	0.3290 ± 0.0088
E3	1.6402 ± 0.0074	0.3262 ± 0.0018	G3	1.3802 ± 0.2444	0.2978 ± 0.0094
E4	1.6483 ± 0.0167	0.3216 ± 0.0151	G4	1.5806 ± 0.0173	0.2786 ± 0.0049
E5	1.7946 ± 0.0193	0.3125 ± 0.0079	G5	1.4446 ± 0.2019	0.3097 ± 0.0191
E6	1.9248 ± 0.0269	0.3174 ± 0.0119	G6	1.4007 ± 0.3192	0.2671 ± 0.0150
E7	1.9182 ± 0.0362	0.3419 ± 0.0134	G7	1.6577 ± 0.2206	0.3357 ± 0.0193
E8	1.8138 ± 0.0110	0.3279 ± 0.0117	G8	1.6384 ± 0.0454	0.3304 ± 0.0096
E9	1.7891 ± 0.0249	0.3418 ± 0.0022	G9	1.6279 ± 0.1809	0.2910 ± 0.0115

tion as described in the literature for other biopolymeric MNs prepared by solvent casting [37,38]. The above sizes allow the MNs to rupture the stratum corneum but not reach the blood vessels, creating ducts that facilitate the flow of large molecules, nanoparticles, and proteins through the skin [39,40].

Considering the height, the MNs containing EE and P407 exhibited a significant positive interference ($p > 0.05$) (Supporting Information File 1, Table S2 and Figure S5), being greater for the amount of extract, which corroborates the results that MNs containing more EE were better formed macroscopically. As for GE, none of the variables significantly interfered in the height measurement ($p > 0.05$), which was confirmed by the difficult formation of MNs containing GE. It can also be confirmed by the response surface graphs; however, greater height values were observed for smaller amounts of P407.

Regarding the measurement of the base width, the amounts of both extracts presented significant negative interference in the final value ($p < 0.05$) (Supporting Information File 1, Table S2 and Figure S5). For GE, positive interference was observed, and for P407 and EE, negative interference was observed. Positive interferences mean that an increase of the studied condition generates an increase in the response, negative interferences mean a decrease of the response with an increase of the studied condition [41], in this case the concentration of PRP and P407 extract. Even with relatively low r values, it was possible to observe the behavior of the formulations with different amounts of PRP and P407 extract regarding height and base width measurements. The base width values of all formulations were quite similar, mainly due to the standardized use of molds.

The response surface is an advanced experiment design technique that helps to understand and optimize the best response. This tool is used to develop a functional relationship between a response of interest, and also to refine models after determining the important factors by selecting the performed experiments [41]. The response surfaces for analysis of height and base width measurements are shown in Figure 5.

The equations obtained for the height and base measurement responses, as well as the values for the correlation coefficient (r), from the statistical analysis of the results obtained for the measurements of microneedles are given in Table 2.

As the base width/height ratio decreased, the failure force decreased as well. This can be observed by the MNs E5, which have the lowest compression force of the MNs containing EE

Table 2: Equations obtained for the height and base responses with the correlation coefficient r.

	EE		GE	
	Equation	r	Equation	r
Height	$Y = 1.7823 + 0.1231X_1 - 0.0985X_1 \cdot X_2 + 0.0417X_{22}^2$	0.9167	$Y = 1.5565$	0.3583
Base	$Y = 0.3275 - 0.0155X_{11}^2 - 0.0156X_{22}^2$	0.7218	$Y = 0.3049 - 0.0210X_2 - 0.0189X_1 \cdot X_2 - 0.0296X_{11}^2 + 0.0272X_{22}^2$	0.8316

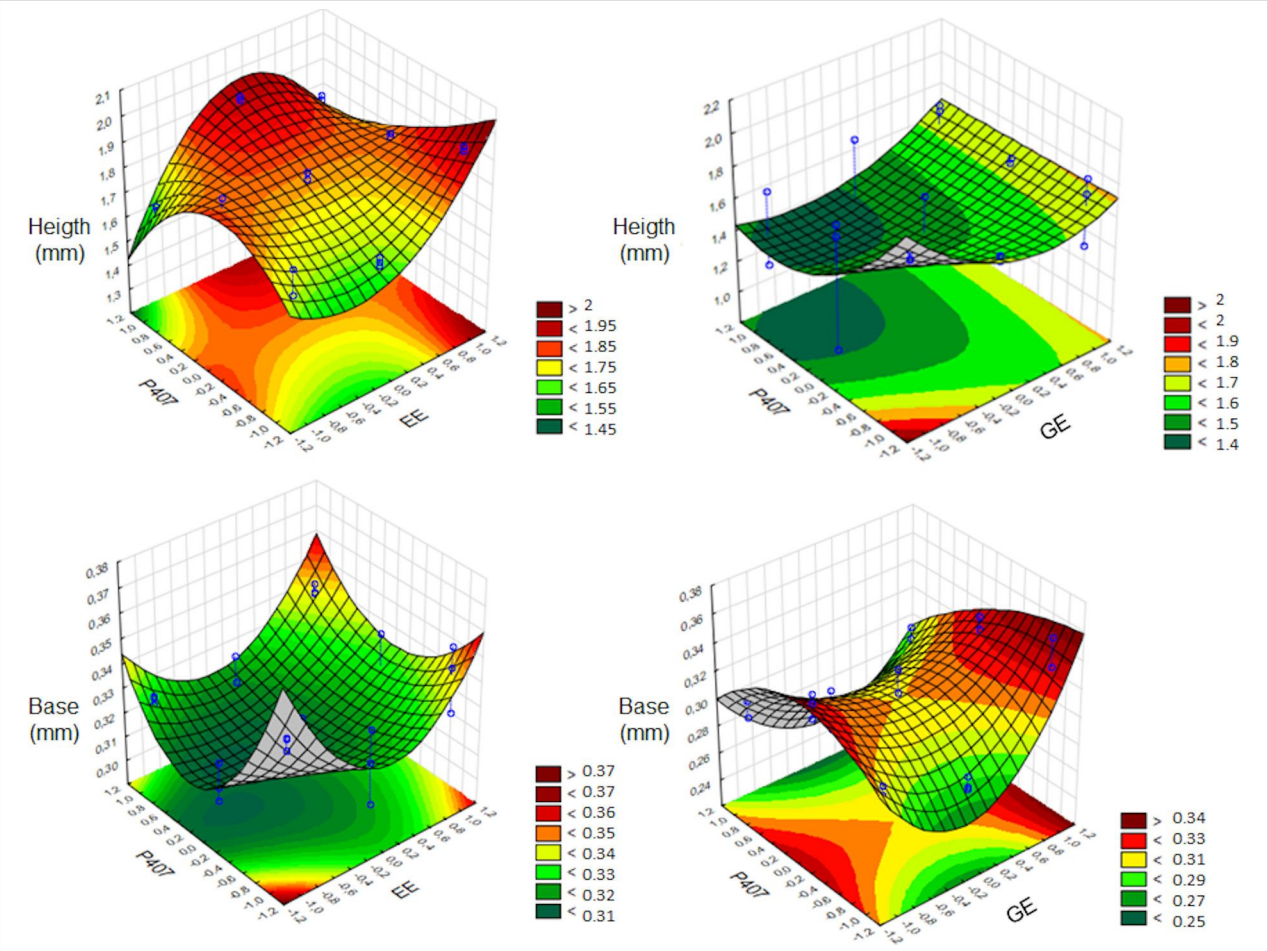


Figure 5: Response surface plots for height and base measurements of MNs containing EE or GE. The color scale is indicated in each figure and shows the isoparametric values.

and an aspect ratio of 1:7 (base width/height) while the MNs E9 have the highest compression value and an aspect ratio of 1:6 (base width/height). Römgens and colleagues also observed that with an increase in the diameter of the MN tips, the force for insertion increases [42]. When different MN tip diameters were studied for insertion into the biological substrate, it was observed that MNs with a diameter of 5 µm presented greater penetration power than MNs with larger diameters [42]. The MNs containing EE and GE displayed similar tip shapes and sizes as the MNs of this previous study, thus favoring penetration.

Analysis of hardness

The 18 formulations were analyzed for compression force and compression area on a hard glass surface (Petri dish). The results are displayed in Table 3.

Regarding the compression force, for MNs containing EE, only the extract showed positive significant interference, where higher values of compression force were observed for MNs containing a greater amount of extract, with the highest value obtained for the E9 formulation, which contains 3% P407.

Considering MNs containing GE, both independent variables had significant interference, being negative for GE and positive for P407. The formulations that presented greater compression force were the formulations G5 and G6, containing 4% of GE and 2% and 3% of P407 respectively. The respective equations obtained were $Y = 0.7928 + 0.5232X_1 - 0.3523X_{11}^2$ and $Y = 0.3230 - 0.1297X_1 + 0.0871X_2 + 0.2187X_{11}^2$ for MNs containing EE or GE, respectively. The response surface plots for analysis of force and compression area are displayed in Figure 6.

For the compression area of MNs containing EE, the highest values were observed for the formulations with 12% of EE, whereas for the formulations with GE the highest values were observed for the formulations containing 4% of GE. The respective equations obtained were $Y = 11.1227 + 7.3499X_1 - 9.4281X_{11}^2 + 4.0988X_{22}^2$ and $Y = 3.5036 - 2.6528X_1 + 2.3812X_2 - 2.8720X_1 \cdot X_2 + 1.8557X_{11}^2$. The results of strength

Table 3: Compression force and compression area of MNs containing EE or GE on a hard glass surface. Each analysis was performed, at least, in triplicate.

Formulation	Compression force (N)	Compression area (N·mm)	Formulation	Compression force (N)	Compression area (N·mm)
E1	0.6133 ± 0.0984	7.9167 ± 1.2208	G1	0.3075 ± 0.0170	2.5867 ± 0.2097
E2	0.6034 ± 0.0489	10.9777 ± 4.0329	G2	0.2220 ± 0.0233	2.4287 ± 0.5104
E3	0.6475 ± 0.0493	7.6293 ± 1.5393	G3	0.4153 ± 0.1330	4.9460 ± 1.9119
E4	0.3436 ± 0.0383	2.4487 ± 0.5678	G4	0.3090 ± 0.0001	2.2160 ± 0.0001
E5	0.3392 ± 0.2011	2.4637 ± 1.5757	G5	0.6140 ± 0.1005	7.1507 ± 1.7283
E6	0.5229 ± 0.0346	4.6517 ± 1.1466	G6	0.4833 ± 0.0298	4.5703 ± 0.6339
E7	1.1130 ± 0.2569	19.0077 ± 4.9568	G7	0.2260 ± 0.0001	2.0580 ± 0.0001
E8	1.1981 ± 0.0231	18.5693 ± 3.2540	G8	0.1245 ± 0.0001	1.1800 ± 0.0001
E9	1.2345 ± 0.0138	15.9167 ± 0.4926	G9	0.2053 ± 0.0124	1.4380 ± 0.1895

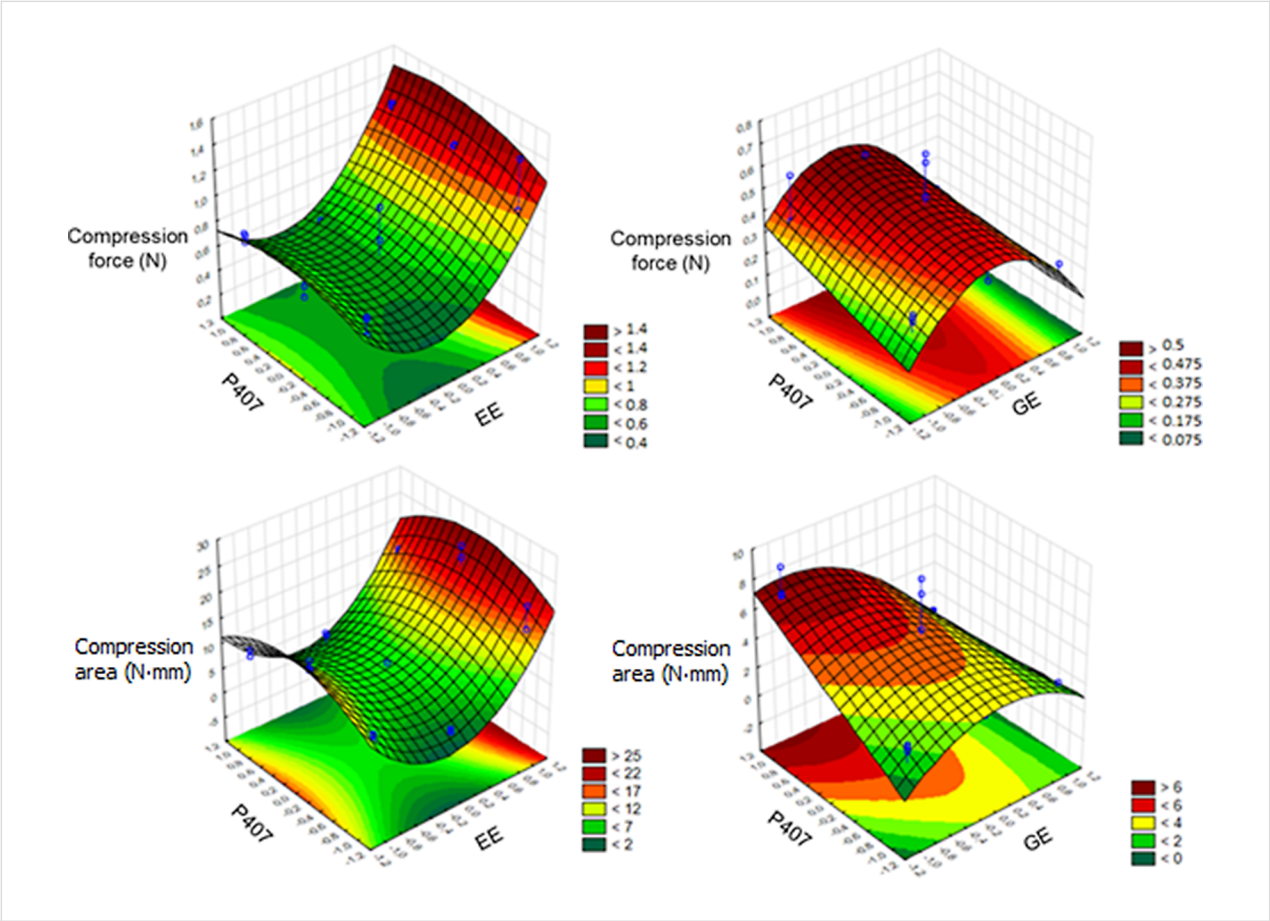


Figure 6: Response surface plots for force and compression area of MNs containing EE or GE. The color scale is indicated in each figure and shows the isoparametric values.

and compression area were essential for choosing the best formulations, in addition to showing the best structures for the amounts of extract and P407 used.

In previous studies of Donnelly and colleagues [4], MNs composed of PVA, alginic acid, Carbopol 971P, and Gantrez were synthesized and also mechanically analyzed. It was observed that, for values greater than 0.03 N per needle, it would already be possible to perforate the stratum corneum to release the active substance. In comparison with the results obtained, formulations E7, E8, and E9 would have presented compression forces in a petri dish sufficient to perforate the initial layer

of the skin. In Supporting Information File 1, Figure S6 it is possible to observe the structure of the MNs before and after the compression test.

Afterwards, the best formulations were chosen to proceed with further characterizations. The selected formulations were E3, E6, E9, and G6. They are composed of 3% P407 and 4%, 8%, and 12% EE, or 4% GE, respectively. These formulations were chosen because they exhibited macroscopic integrity and the formulations containing EE with 3% of P407 presented the highest values in the mechanical analysis. Although the MNs containing GE were malleable, the formulation GE6 was chosen because it showed good integrity, with values similar to those of E3. It was utilized for comparison with the formulations containing EE.

Compression test on different surfaces

The best formulations (E3, E6, E9, and G6) were mechanically evaluated in compression tests on PVC film, Parafilm M, gelatin, and porcine skin. The results for the compression force of the best formulations are displayed in Table 4. The MNs did not yield total penetration of PVC film, Parafilm M, and porcine skin; however, it was verified that the applied force was sufficient to mark the substrates. All evaluated formulations displayed penetration of the gelatin substrate, including the MNs without PRP extract and the stainless-steel MNs (standard) used to obtain the mold. Previous studies have shown that MNs composed of Gantrez S-97 and PEG 10,000 had differences when inserted into porcine skin and layered Parafilm M [43].

For all analyses, as the amount of extract in the formulations increases, the compression force also increases regardless of the surface utilized in the test. The formulation G6 displayed the lowest results, probably due to the presence of propylene glycol in the formulation. Considering that the selected formulations contained 3% P407, the amount of PRP extract was the only factor that influenced the increase in the compression force. Thus, it can be inferred that the hardness of MNs increases with the increase in the concentration of PRP extract in the formulation. MNs with GE were malleable due to the plasticizing effect of propylene glycol, which resulted in lower mechanical strength [34]. In contrast, the presence of EE resulted in better structured MNs that were harder and had greater penetration capacity.

In other studies using MNs composed of PVA, Carbopol 971P, and alginic acid, it was observed that with a force of 0.03 N or greater, most MNs could penetrate the stratum corneum [4]. Thus, the force values displayed for the selected formulations also indicate the ability to penetrate porcine skin.

All selected MN formulations were statistically compared with MNs without PRP extract and stainless-steel MNs (standard) using Students' *t*-test evaluation of possible significant differences among the compression forces for each substrate/surface utilized. The results for the *p* values are displayed in Supporting Information File 1, Table S1. There were no statistically significant differences for PVC film when the formulations E3 and G6 were compared with the formulations without extract and the standard. For Parafilm M, no significant differences were observed when comparing E3 and MNs without PRP, G6 and MNs without PRP, and MNs without PRP and the standard. For the analysis using gelatin as surface, only the difference between formulations E6 and E9 was not statistically significant. When the surface was porcine skin, the differences between E6 and E9, E3 and G6, and MNs without PRP and standard were not statistically significant (Figure S3, Supporting Information File 1).

Supporting Information File 1, Figure S4 displays images of the different surfaces (PVC film, Parafilm M, gelatin, and porcine skin) after the compression test with MN formulations. It was not possible to observe any punctures or, consequently, to stain the porcine skin, possibly due to the thickness of the skin.

Table 4: Compression force (N) of the selected MN formulations applied on different surfaces (PVC film, Parafilm M, gelatin and porcine skin). Each analysis was performed, at least, in triplicate.

Formulations	Force (N)			
	PVC film	Parafilm M	Gelatin	Porcine skin
E3	0.4247 ± 0.0123	0.3863 ± 0.0090	0.1479 ± 0.0129	0.0979 ± 0.0017
E6	0.5085 ± 0.0116	0.6319 ± 0.0253	0.2726 ± 0.0094	0.1431 ± 0.0093
E9	0.5492 ± 0.0161	0.7476± 0.0394	0.2737 ± 0.0120	0.1438 ± 0.0055
G6	0.3989 ± 0.0031	0.3422 ± 0.0164	0.2231 ± 0.0103	0.0866 ± 0.0064
MNs without propolis extract	0.1369 ± 0.0099	0.3429 ± 0.0857	0.1030 ± 0.0041	0.1893 ± 0.0158
Stainless still MNs (standard model)	0.1543 ± 0.0109	0.7943 ± 0.0525	0.3589 ± 0.0108	0.2406 ± 0.0231

Conclusion

The present study demonstrated, for the first time, the design of MNs composed of PVA, PVP, and P407 as a polymeric platform for the delivery of alcoholic and glycolic green propolis extracts. MN formulations were characterized regarding their morphology, dimensions, and mechanical properties. Selected MN formulations (E3, E6, E9, and G6) exhibited suitable mechanical strength to penetrate different substrates that mimic the human skin, making them potentially useful systems for topical propolis administration. As MNs are minimally invasive platforms, the selected systems can be easy to apply and monitor. Further studies should be conducted regarding in vitro and in vivo evaluation of the biological activity and cytotoxicity of the MNs, the vitro PRP release profile, the cutaneous permeation using porcine and human skin, and photoacoustic spectroscopy.

Experimental

Materials

Poloxamer 407 (P407), gelatin, and propylene glycol were purchased from Sigma (St. Louis, MO, USA). Polyvinyl alcohol (PVA) was obtained from Neon (Sao Paulo, SP, Brazil), polyvinylpyrrolidone (PVP), and ethanol 96° GL was purchased from Labsynth (Sao Paulo, SP, Brazil). Sylgard^{TM} 184 silicone elastomers kit (polydimethylsiloxane; PDMS) was purchased from Dow (Midland, MI, USA). Purified water was obtained from a water purification system (Evoqua Water Technologies, Pittsburgh, PA, USA). Absolute ethanol was purchased from Anidrol (Sao Paulo, SP, Brazil).

Preparation and characterization of PRP extracts

Brazilian green propolis (PRP) was obtained from an apiary of *Apis mellifera* L. bees, located inside a eucalyptus reserve, surrounded by native forest with predominance of *Baccharis dracunculifolia* (Asteraceae), in the northwest of Parana state. This research was registered in Brazil with SISGEN N° AC7A2F5. The different PRP extracts were prepared by turbo extraction. The ethanolic extract (EE) was obtained using ethanol 96° GL and the comminuted drug with a drug/solvent (w/w) ratio of 3:7. The glycolic extract (GE) was prepared using the comminuted drug and an aqueous solution of propylene glycol 50% (w/w) and the same drug/solvent (w/w) ratio of 3:7. The final dispersions were filtered through grade-3 filter paper [44,45].

The pH determination was performed using a pHmeter calibrated with buffer solutions. The relative density of the extract was determined using a pycnometer calibrated at 20 °C in a controlled temperature environment (20 °C). To determine the dry residue, exactly 1 g of extract was weighed, the excess solvents were evaporated on a hot plate for approximately 10 min. Subsequently, the containers containing the extracts were taken to an oven (110 °C) for 40 min until constant weight. An aliquot of 12.5 mL of the extractive solution was placed in a round-bottomed flask, added to 50.0 mL of purified water and subjected to simple distillation. The distillate was collected in a 50.0 mL volumetric flask and made up to volume with purified water. The distillate density was determined, and from the density the alcohol content was determined.

The determination of the total polyphenol content was performed in 25.0 mL volumetric flasks, 10 mL of purified water were added and 10.0 μL of extract were added. Then, 1.0 mL of phosphomolybdotungstic reagent R (Folin–Ciocalteau) was added and the volume was made up with 14.06% (m/V) aqueous sodium carbonate solution. The extracts were analyzed using a high-performance liquid chromatograph coupled to a UV–vis spectrophotometric detector. For the detection of polyphenols, chrysin and p-coumaric acid (analytical standard) at a wavelength (λ) of 310 nm were used as markers. At least three determinations were performed for each assay [36,46-48].

Preparation of silicone molds

The master structure utilized to fabricate the molds was a stainless-steel microneedle system (cartridge) from DermaPen (Belrose, Australia) containing 36 microneedles of 2 mm in length. The molds developed were inverse replicas of this master structure.

For the preparation of the PDMS mold, suitable amounts of the catalyst agent and the silicone base were mixed, in a proportion of 1:6, using a beaker and taken to ultrasound for 5 min. Afterwards, the mixture was poured into 12-well plates and taken to ultrasound for another 5 min. The microneedle cartridge was inserted into the mixture and placed under ultrasound for 5 min to remove all air bubbles. The plate containing the silicone and the microneedle cartridge was placed in a vacuum desiccator for silicone curing. After 24 h, the cartridge was carefully removed and the mold obtained was cleaned and evaluated for integrity for later use.

Fabrication of microneedles

Polymeric MNs were prepared using the mold casting technique. The polymeric matrix, composed of PVA, PVP, P407, and the different types of PRP extract, was prepared to compose the microneedle system. For the development of MNs, three different concentrations of P407 and PRP extract were used in a fixed matrix of PVA/PVP using a ratio of 1:1. P407 was used at 1%, 2%, and 3% (w/w) and PRP extract at 4%, 8%, and 12% (w/w) for the ethanolic extract and 2%, 4%, and 8% (w/w) for the glycolic extract, resulting in a factorial design of 3^2, totaling

nine formulations for each type of extract, rendering a total of 18 formulations (Table 5).

Table 5: Experimental 3^2 design utilized for the development of microneedles (MNs) composed of polyvinyl alcohol (PVA) and polyvinylpyrrolidone (PVP) in a fixed 1:1 ratio, poloxamer 407 (P407), and ethanolic propolis extract (EE) or glycolic propolis extract (GE).

	Levels		
Independent variables	Low (−1)	Central (0)	High (+1)
X_1 = P407 (%, w/w)	1	2	3
X_2 = EE (%, w/w)[a]	4	8	12
X_2 = GE (%, w/w)[b]	2	4	8
Standard run (formulations)	X_1	X_2	
E1	−1	−1	
E2	0	−1	
E3	+1	0	
E4	−1	0	
E5	0	+1	
E6	+1	+1	
E7	−1	−1	
E8	0	−1	
E9	+1	0	
G1	−1	0	
G2	0	+1	
G3	+1	+1	
G4	−1	−1	
G5	0	−1	
G6	+1	0	
G7	−1	0	
G8	0	+1	
G9	+1	+1	

[a]formulations containing EE (block a); [b]formulations containing E (block b).

Firstly, each polymer was dispersed separately. To PVA, 8 mL of purified water were added, and the mixture was heated and stirred until completely dispersed. The suitable amount of PVP was dissolved in 3 mL of absolute ethyl alcohol, and P407 was dissolved in 2 mL of the same solvent. After obtaining the individual dispersions, the P407 was poured onto the PVP, magnetically stirred for 10 min, and this mixture was poured onto the PVA under magnetic stirring for another 10 min, after which the PRP extract was placed and the mixture was stirred for 20 min.

Afterwards, the final formulations were centrifuged at 3200 rpm for 10 min to remove air bubbles. Each formulation was carefully poured onto the molds to form a complete microneedle patch. Then, they were placed in a desiccator for 48 h for complete casting. Subsequently, the MNs were carefully recovered from the molds with the help of tweezers and stored in desiccators until future use.

Experimental design

The 3^2 full factorial design (two blocks) was utilized to determine the influence of P407 (X_1) and PRP extract (X_2) concentrations on height and base measurements, strength, and printing area in a hard surface (glass Petri dish) [49]. The independent factors were evaluated at three levels, low (−1), central (0) and high (+1) (Table 5). The surface response plots of the MN system behavior were utilized to show the interaction effects of the independent variables (P407 and EE or GE) on height and base measurements, strength, and printing area in the hard surface. To predict the optimal conditions, a polynomial equation was fitted correlating the relationship between the independent variables and the response:

$$Y = b_0 + b_1X_1 + b_2X_2 + b_{12}X_1X_2 + b_{11}{X_{11}}^2 + b_{22}{X_{22}}^2 \quad (1)$$

where Y is the response (the dependent variable) as function of X_1 and X_2, b_0 is a constant term (the arithmetic mean response of nine batches), b_1 and b_2 are the estimated coefficients of linear terms, and b_{12} is the coefficient of the interaction effect. The polynomial terms ${X_{11}}^2$ and ${X_{22}}^2$ consider the non-linearity, and the interaction term X_1X_2 shows the response changes when two factors are simultaneously changed.

The experiments were randomized to minimize the influence of unexplained variability in the responses. Residual analysis was also conducted to validate the assumptions utilized in the analysis of variance and to identify outliers. The proportion of variance explained by models obtained was given by the multiple and adjusted coefficients (r^2 and ${r^2}_{adj}$), whereas the adequacy of the model was determined by a lack-of-fit test.

Macroscopic evaluation

The MNs obtained were evaluated macroscopically for flexibility, integrity, homogeneity, color, and presence of air bubbles. The height and base measurements of the MNs obtained were analyzed (Figure 7).

Optical microscopy analysis

The evaluations of the morphological characteristics and dimensions of the molds and MNs were carried out by optical microscopy using an optical microscope KozoOptics (Nanjing, China), at 40× magnification. For analysis, a row of MNs was cut from the structure obtained for better visualization of the isolated microneedles.

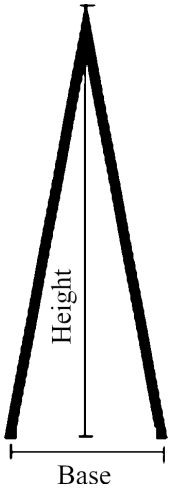


Figure 7: Schematic representation for the analysis of the height and base measurements of the microneedles.

Scanning electron microscopy

The elucidation of more specific morphological details of the fabricated MNs was performed by scanning electron microscopy. Each sample was placed over a circular metallic holder (with the help of double-sided tape) and fixed with colloidal gold in a hermetically closed chamber in argon atmosphere. The samples were observed using a Quanta 250 electron microscope (FEI, Hillsboro, OR, USA).

Mechanical analysis

Hardness

The effects of the amount of P407 and of amount and type of PRP extract on the MN hardness and mechanical resistance were quantitatively evaluated by a microneedle textural study. A compressive load was applied (i.e., force applied parallel to the vertical axis) to the polymeric MNs using a TA-XTplus texturometer (TA Instruments, Surrey, UK). The MN patches were connected to the mobile cylindrical probe (P/1 – 1″ diameter aluminium cylinder) with double-sided tape. The probe was pressed against the defined surface (hard glass surface of Petri dish) at a rate of 0.05 mm/s. The pre-test and post-test speeds were 1 mm/s, and the applied force was 0.049 N. The length at which the MNs descended in the test was 1.5 mm. From the relationship between force and time, the compression force (the maximum force during compression) and compression area (the work required to deform the sample during compression) were calculated using the software Texture Exponent 6.1.12.0 (Stable Micro Systems, Surrey, UK).

Puncture

The effect of formulation composition on the puncture force and distance was evaluated by MN insertion study. The best formulations selected from previous analysis were mechanically evaluated using different surfaces. The same texturometer and probe previously described were utilized. In compression mode, the MNs patch attached to the probe was pressed against the defined surface with a force of 0.049 N at a 0.05 mm/s using 5% gelatin or porcine skin or at rate of 0.1 mm/s using PVC film or Parafilm M [4]. The pre-test and post-test speeds were 1 mm/s. The length at which the MNs descended in the test was 1.5 mm. The force required to pucture the substrate during the compression of the probe/MNs patch was calculated using the software Texture Exponent 6.1.12.0 (Stable Micro Systems, Surrey, UK). The substrate composed of an aqueous dispersion of gelatin 5% (w/w) was prepared by dispersing the weighed gelatin in warm water. After complete dispersion, the dispersion was poured into petri dishes and allowed to dry at room temperature to be used in further tests. The porcine skin samples were obtained by dissection of skins from the ears of pigs (albinos and youngsters), which were recently slaughtered. The skin patches were washed, the hairs cut and, later, the patches were dissected in order to extract the epidermis and dermis. They were cut into standardized sizes, wrapped in plastic film and aluminum foil, and kept in a freezer. At the time of use, they were thawed at room temperature, and each skin fragment was then placed in a base for the test.

Statistical analysis

The effects of the amount of P407 and of amount and type of PRP extract on the height and base measurements, strength, and printing area in the petri dish were statistically evaluated using three-way analysis of variance (ANOVA). Tukey's post-hoc test was used to analyze significant differences. A significance level of $p < 0.05$ was considered and the Statistica 12.0 software (StatSoft Company, Tulsa, OK, USA) was used for all analyses.

Supporting Information

Supporting Information features pictures of molds and macroscopic appearance of the MNs, statistical analysis of the compression force of MNs applied on different substrates (PVC film, Parafilm M, Gelatin, and porcine skin), images of substrates after puncture test, statistical analysis of MN height and base measurements, and images of the MNs before and after the compression test.

Supporting Information File 1

Additional figures and tables.
[https://www.beilstein-journals.org/bjnano/content/supplementary/2190-4286-13-42-S1.pdf]

Funding

The authors are thankful to the Brazilian funding agencies CAPES (*Coordenação de Aperfeiçoamento de Pessoal de Nível Superior*/Coordination for the Improvement of Higher Education Personnel; Finance Code 001), CNPq (*Conselho Nacional de Pesquisa*/National Research Council; Process nº 307695/2020-4), and FINEP (*Financiadora de Estudos e Projetos*/Financier of Studies and Projects) for their support.

ORCID® iDs

Camila Felix Vecchi - https://orcid.org/0000-0003-3788-0497
Rafaela Said dos Santos - https://orcid.org/0000-0002-6473-4869
Jéssica Bassi da Silva - https://orcid.org/0000-0003-0586-7802
Marcos Luciano Bruschi - https://orcid.org/0000-0002-4838-5742

References

1. Radhika, C.; Gnanavel, B. K. *Mater. Today: Proc.* **2021,** *39,* 1538–1542. doi:10.1016/j.matpr.2020.05.549
2. Zainal Abidin, H. E.; Ooi, P. C.; Tiong, T. Y.; Marsi, N.; Ismardi, A.; Mohd Noor, M.; Nik Zaini Fathi, N. A. F.; Abd Aziz, N.; Sahari, S. K.; Sugandi, G.; Yunas, J.; Dee, C. F.; Yeop Majlis, B.; Hamzah, A. A. *J. Pharm. Sci.* **2020,** *109,* 2485–2492. doi:10.1016/j.xphs.2020.04.019
3. Sharma, S.; Hatware, K.; Bhadane, P.; Sindhikar, S.; Mishra, D. K. *Mater. Sci. Eng., C* **2019,** *103,* 109717. doi:10.1016/j.msec.2019.05.002
4. Donnelly, R. F.; Majithiya, R.; Singh, T. R. R.; Morrow, D. I. J.; Garland, M. J.; Demir, Y. K.; Migalska, K.; Ryan, E.; Gillen, D.; Scott, C. J.; Woolfson, A. D. *Pharm. Res.* **2011,** *28,* 41–57. doi:10.1007/s11095-010-0169-8
5. Kim, Y.-C.; Park, J.-H.; Prausnitz, M. R. *Adv. Drug Delivery Rev.* **2012,** *64,* 1547–1568. doi:10.1016/j.addr.2012.04.005
6. Reis, T. A.; Lira de Sá-Barreto, L. C.; Soares da Cunha-Filho, M. S.; Gratieri, T.; Gelfuso, G. M. *Rev. Bras. Med.* **2014,** *51,* 159–169.
7. Soares, M.; Vitorino, C.; Sousa, J.; Pais, A. *Rev. Cienc. Farm. Basica Apl.* **2015,** *36,* 337–348.
8. Moreira, A. F.; Rodrigues, C. F.; Jacinto, T. A.; Miguel, S. P.; Costa, E. C.; Correia, I. J. *Pharmacol. Res.* **2019,** *148,* 104438. doi:10.1016/j.phrs.2019.104438
9. Arora, A.; Prausnitz, M. R.; Mitragotri, S. *Int. J. Pharm.* **2008,** *364,* 227–236. doi:10.1016/j.ijpharm.2008.08.032
10. Singh, A.; Yadav, S. *Indian Dermatol. Online J.* **2016,** *7,* 244. doi:10.4103/2229-5178.185468
11. Salwa; Chevala, N. T.; Jitta, S. R.; Marques, S. M.; Vaz, V. M.; Kumar, L. *J. Drug Delivery Sci. Technol.* **2021,** *65,* 102711. doi:10.1016/j.jddst.2021.102711
12. van der Maaden, K.; Jiskoot, W.; Bouwstra, J. *J. Controlled Release* **2012,** *161,* 645–655. doi:10.1016/j.jconrel.2012.01.042
13. Tuan-Mahmood, T.-M.; McCrudden, M. T. C.; Torrisi, B. M.; McAlister, E.; Garland, M. J.; Singh, T. R. R.; Donnelly, R. F. *Eur. J. Pharm. Sci.* **2013,** *50,* 623–637. doi:10.1016/j.ejps.2013.05.005
14. Hong, X.; Wei, L.; Wu, F.; Wu, Z.; Chen, L.; Liu, Z.; Yuan, W. *Drug Des., Dev. Ther.* **2013,** *7,* 945–952. doi:10.2147/dddt.s44401
15. Haridass, I. N.; Wei, J. C. J.; Mohammed, Y. H.; Crichton, M. L.; Anderson, C. D.; Henricson, J.; Sanchez, W. Y.; Meliga, S. C.; Grice, J. E.; Benson, H. A. E.; Kendall, M. A. F.; Roberts, M. S. *J. Controlled Release* **2019,** *306,* 59–68. doi:10.1016/j.jconrel.2019.05.024
16. Rzhevskiy, A. S.; Telaprolu, K.; Mohammed, Y. H.; Grice, J. E.; Roberts, M. S.; Anissimov, Y. G. *Eur. J. Pharm. Biopharm.* **2018,** *127,* 12–18. doi:10.1016/j.ejpb.2018.01.019
17. Burdock, G. A. *Food Chem. Toxicol.* **1998,** *36,* 347–363. doi:10.1016/s0278-6915(97)00145-2
18. Marquele, F. D.; Di Mambro, V. M.; Georgetti, S. R.; Casagrande, R.; Valim, Y. M. L.; Fonseca, M. J. V. *J. Pharm. Biomed. Anal.* **2005,** *39,* 455–462. doi:10.1016/j.jpba.2005.04.004
19. de Albuquerque-Júnior, R. L. C.; Barreto, A. L. S.; Pires, J. A.; Reis, F. P.; Lima, S. O.; Ribeiro, M. A. G.; Cardoso, J. C. *Int. J. Morphol.* **2009,** *27,* 1105–1110. doi:10.4067/s0717-95022009000400025
20. Barbosa, M. H.; Zuffi, F. B.; Maruxo, H. B.; Jorge, L. L. R. *Acta Paulista de Enfermagem* **2009,** *22,* 318–322. doi:10.1590/s0103-21002009000300013
21. Sehn, E.; Hernandes, L.; Franco, S. L.; Gonçalves, C. C. M.; Baesso, M. L. *Anal. Chim. Acta* **2009,** *635,* 115–120. doi:10.1016/j.aca.2009.01.019
22. Ghisalberti, E. L. *Bee World* **1979,** *60,* 59–84. doi:10.1080/0005772x.1979.11097738
23. de Funari, C. S.; de Oliveira Ferro, V.; Mathor, M. B. *J. Ethnopharmacol.* **2007,** *111,* 206–212. doi:10.1016/j.jep.2006.11.032
24. Sforcin, J. M.; Fernandes, A., Jr.; Lopes, C. A. M.; Bankova, V.; Funari, S. R. C. *J. Ethnopharmacol.* **2000,** *73,* 243–249. doi:10.1016/s0378-8741(00)00320-2
25. Park, Y. K.; Koo, M. H.; Abreu, J. A. S.; Ikegaki, M.; Cury, J. A.; Rosalen, P. L. *Curr. Microbiol.* **1998,** *36,* 24–28. doi:10.1007/s002849900274
26. Aulton, M. E. *Pharmaceutics;* Churchill Livingstone: Edinburgh, 2002; Vol. 2.
27. Owen, S. C.; Weller, P. J. *Propylene Glycol*, 5th ed.; Association, A. P., Ed.; Washington, DC:, 2006.
28. Vecchi, C. F.; Said dos Santos, R.; Bassi da Silva, J.; Rosseto, H. C.; Sakita, K. M.; Svidzinski, T. I. E.; Bonfim-Mendonça, P. d. S.; Bruschi, M. L. *Photodiagn. Photodyn. Ther.* **2020,** *32,* 101957. doi:10.1016/j.pdpdt.2020.101957
29. Vecchi, C. F.; dos Santos, R. S.; Bruschi, M. L. *Ther. Delivery* **2020,** *11,* 431–446. doi:10.4155/tde-2020-0031
30. Vecchi, C. F.; Cesar, G. B.; de Souza, P. R.; Caetano, W.; Bruschi, M. L. *Pharm. Dev. Technol.* **2021,** *26,* 138–149. doi:10.1080/10837450.2020.1849283
31. Bruschi, M. L.; Panzeri, H.; de Freitas, O.; Helena, E.; Lara, G.; Palmira, M.; Gremião, D. *Rev. Bras. Cienc. Farm.* **2006,** *42,* 29–47. doi:10.1590/s1516-93322006000100004
32. Pereira, R. R. A. Development and characterization of thermo-sensitive mucoadhesive system containing propolis microparticles for the potential treatment of vulvovaginal candidiasis. Ph.D. Thesis, State University of Maringa, Brazil, 2011.
33. Pamplona, B. *Rev. Racine* **1997,** *7,* 49–53.
34. Cho, Y. H.; Kim, B. C.; Dan, K. S. *Macromol. Res.* **2009,** *17,* 591–596. doi:10.1007/bf03218914
35. Bruschi, M. L.; Cardoso, M. L. C.; Lucchesi, M. B.; Gremião, M. P. D. *Int. J. Pharm.* **2003,** *264,* 45–55. doi:10.1016/s0378-5173(03)00386-7
36. Bruschi, M. L. Development and characterisation of into the periodontal pocket propolis delivery systems. Ph.D. Thesis, University of Sao Paulo, Brazil, 2006.
37. Zhang, Y.; Jiang, G.; Yu, W.; Liu, D.; Xu, B. *Mater. Sci. Eng., C* **2018,** *85,* 18–26. doi:10.1016/j.msec.2017.12.006

38. Yu, W.; Jiang, G.; Zhang, Y.; Liu, D.; Xu, B.; Zhou, J. *Mater. Sci. Eng., C* **2017,** *80,* 187–196. doi:10.1016/j.msec.2017.05.143
39. Fonseca, D. F. S.; Costa, P. C.; Almeida, I. F.; Dias-Pereira, P.; Correia-Sá, I.; Bastos, V.; Oliveira, H.; Vilela, C.; Silvestre, A. J. D.; Freire, C. S. R. *Macromol. Biosci.* **2020,** *20,* 2000195. doi:10.1002/mabi.202000195
40. Rzhevskiy, A. S.; Singh, T. R. R.; Donnelly, R. F.; Anissimov, Y. G. *J. Controlled Release* **2018,** *270,* 184–202. doi:10.1016/j.jconrel.2017.11.048
41. Khuri, A. I.; Mukhopadhyay, S. *Wiley Interdiscip. Rev.: Comput. Stat.* **2010,** *2,* 128–149. doi:10.1002/wics.73
42. Römgens, A. M.; Bader, D. L.; Bouwstra, J. A.; Baaijens, F. P. T.; Oomens, C. W. J. *J. Mech. Behav. Biomed. Mater.* **2014,** *40,* 397–405. doi:10.1016/j.jmbbm.2014.09.015
43. Larrañeta, E.; Moore, J.; Vicente-Pérez, E. M.; González-Vázquez, P.; Lutton, R.; Woolfson, A. D.; Donnelly, R. F. *Int. J. Pharm.* **2014,** *472,* 65–73. doi:10.1016/j.ijpharm.2014.05.042
44. Bruschi, M. L.; Klein, T.; Lopes, R. S.; Franco, S. L.; Gremião, M. P. D. *Rev. Cienc. Farm. (Sao Paulo, Braz.)* **2002,** *23,* 289–306.
45. Rosseto, H. C.; Toledo, L. d. A. S. d.; Francisco, L. M. B. d.; Esposito, E.; Lim, Y.; Valacchi, G.; Cortesi, R.; Bruschi, M. L. *Colloids Surf., B* **2017,** *158,* 441–452. doi:10.1016/j.colsurfb.2017.07.029
46. Brazilian National Health Surveillance Agency (ANVISA). Brazilian Pharmacopeia. 6th Ed.; Vol. 1, 2019.
47. de Francisco, L.; Pinto, D.; Rosseto, H.; Toledo, L.; Santos, R.; Tobaldini-Valério, F.; Svidzinski, T.; Bruschi, M.; Sarmento, B.; Oliveira, M. B. P. P.; Rodrigues, F. *Food Res. Int.* **2018,** *105,* 537–547. doi:10.1016/j.foodres.2017.11.046
48. Bruschi, M. L.; Franco, S. L.; Gremião, M. P. D. *J. Liq. Chromatogr. Relat. Technol.* **2003,** *26,* 2399–2409. doi:10.1081/jlc-120023254
49. Villa Nova, M.; Ratti, B. A.; Herculano, L. S.; Bittencourt, P. R. S.; Novello, C. R.; Bazotte, R. B.; de Oliveira Silva Lautenschlager, S.; Bruschi, M. L. *Pharm. Dev. Technol.* **2019,** *24,* 12–23. doi:10.1080/10837450.2017.1410556

License and Terms

This is an open access article licensed under the terms of the Beilstein-Institut Open Access License Agreement (https://www.beilstein-journals.org/bjnano/terms), which is identical to the Creative Commons Attribution 4.0 International License (https://creativecommons.org/licenses/by/4.0). The reuse of material under this license requires that the author(s), source and license are credited. Third-party material in this article could be subject to other licenses (typically indicated in the credit line), and in this case, users are required to obtain permission from the license holder to reuse the material.

The definitive version of this article is the electronic one which can be found at:
https://doi.org/10.3762/bjnano.13.42

BEILSTEIN JOURNAL OF NANOTECHNOLOGY

Ciprofloxacin-loaded dissolving polymeric microneedles as a potential therapeutic for the treatment of *S. aureus* skin infections

Sharif Abdelghany[*1,§], Walhan Alshaer[2], Yazan Al Thaher[3], Maram Al Fawares[2], Amal G. Al-Bakri[1], Saja Zuriekat[1] and Randa SH. Mansour[3]

Full Research Paper

Open Access

Address:
[1]School of Pharmacy, University of Jordan, Amman, 11942, Jordan, [2]Cell Therapy Center, University of Jordan, Amman, 11942, Jordan and [3]Faculty of Pharmacy, Philadelphia University, Amman, 19392, Jordan

Email:
Sharif Abdelghany[*] - s.abdelghany@ju.edu.jo

* Corresponding author
§ Tel +962 6 535 5000

Keywords:
dissolving microneedles; microneedles; polyvinyl alcohol (PVA); polyvinylpyrrolidone (PVP); skin infection

Beilstein J. Nanotechnol. **2022,** *13,* 517–527.
https://doi.org/10.3762/bjnano.13.43

Received: 16 February 2022
Accepted: 01 June 2022
Published: 15 June 2022

This article is part of the thematic issue "Microneedles for vaccination and drug delivery".

Guest Editor: P. D. Prewett

© 2022 Abdelghany et al.; licensee Beilstein-Institut.
License and terms: see end of document.

Abstract

Microneedles have been widely studied for many topical and transdermal therapeutics due to their ability to painlessly puncture the skin, thereby bypassing the stratum corneum, the main skin barrier. In this study, ciprofloxacin (CIP) was loaded into dissolving polymeric microneedles prepared by a two-layer centrifugation method as a potential treatment of skin infections such as cellulitis. The polymers used were polyvinyl alcohol (PVA) and polyvinylpyrrolidone (PVP). Two formulations were investigated, namely CIP_MN1, composed of 10 mg ciprofloxacin incorporated into a polymer matrix of PVA and PVP with a weight ratio of (9:1), and CIP_MN2, composed of 10 mg ciprofloxacin incorporated into PVA polymer. CIP_MN1 and CIP_MN2 showed a mean microneedle height of 188 and 179 µm, respectively. Since Parafilm has been proven as a model to examine the perforation of microneedles in skin, it was used to evaluate the ability of microneedles to perforate the skin. CIP_MN1 showed almost complete perforation of Parafilm, 190 pores, compared to CIP_MN2 which created only 85 pores in Parafilm, and therefore CIP_MN1 was used for subsequent studies. Examining CIP_MN1 on agarose gel as an in vitro model of human skin showed that the formula was able to fully perforate the agarose gel. Moreover, this formula showed significantly greater antimicrobial activity ($p < 0.0001$) compared to a free gel of ciprofloxacin against *Staphylococcus aureus* in an agarose gel-based model. This was evidenced by a zone of inhibition of 29 mm for the microneedle formulation of ciprofloxacin (CIP_MN1) compared to 2 mm for the free gel of ciprofloxacin. Furthermore, the CIP_MN1 showed complete dissolution in human skin after 60 min from application. Finally, the skin deposition of CIP_MN1 was investigated in ex vivo excised human skin. CIP_MN1 showed significantly more deposition of ciprofloxacin in deeper skin layers compared to the free gel of ciprofloxacin, and the released ciprofloxacin from the microneedles

tends to migrate to deeper layers with time. Collectively, these results suggest that CIP_MN1 can be a potential delivery system for the treatment of *S. aureus* skin infections.

Introduction

Topical and transdermal drug delivery is a major route for the administration of antimicrobials to the infected parts of the skin and to the systemic circulation. The main limitation to dermal drug delivery is skin barriers. This is mainly due the uppermost dead keratinized skin layer known as the stratum corneum [1]. Microneedles of different shapes and sizes have been utilized to overcome this limitation since they can painlessly penetrate the upper skin layers [2]. Patients can self-administer microneedles and, thus, overcome the pain associated with conventional parenteral injections. Moreover, this drug delivery system can potentially overcome the low bioavailability of orally administered drugs due to poor absorption and enzymatic degradation in the gastrointestinal tract [3,4].

Among the different types of microneedles, dissolving microneedles have attracted research due to their advantages, which include low cost and simple preparation techniques. These microneedles are manufactured of polymers incorporated with medicaments and are intended to dissolve completely in the skin, permitting the medicament to be distributed in deeper skin layers to treat local and systemic infections [5].

Previous studies have shown the advantages of dissolving microneedles in reducing the microbial burden in bacterial and fungal skin infections [6,7]. Herein, we are aiming at providing a potential microneedle delivery system for the treatment of staphylococcal skin and soft tissue infections such as cellulitis. Cellulitis, as an example of common bacterial skin infection, is a potentially serious disease that involves the dermis and subcutaneous tissues [8]. Gram-positive cocci such as *Staphylococcus aureus* are among the predominant causes of cellulitis [9-11]. Ciprofloxacin is a broad spectrum quinolone antibiotic [12], reported to effectively manage soft tissue and skin infections (STSI) caused by *S. aureus* [13-16]. However, the therapeutic dose of ciprofloxacin upon using conventional delivery systems is relatively high and associated with adverse effects, which partially contributed to its current limited use in the management of *S. aureus* STSI [17].

Therefore, a proper delivery system that can evade the barrier properties of the skin is essential to be effective in the treatment of cellulitis and other skin infections. In this work, the potential of dissolving polymeric microneedles loaded with ciprofloxacin for the treatment of *S. aureus* skin infections was investigated. Recent studies showed that dissolving polymeric microneedles are a promising approach in topical and transdermal drug delivery because of the rapid dissolution and/or degradation of the polymer, which, in turn, releases the incorporated drug [18]. These dissolving microneedles are based on polymers such as PVA, PVP, chitosan, and poly(lactide-*co*-glycolide) [19].

In our study, polymer-based microneedles were optimized to achieve a formulation that can efficiently penetrate the skin. In this context, microneedles were studied regarding drug content and penetration of Parafilm and an agarose-based skin model. Parafilm has been utilized to test the insertion properties of polymeric microneedles [20]. Parafilm-M is mainly composed of paraffin waxes and polyalkene (polyolefin) [21] and, thus, presumably similar in hydrophobicity to the stratum corneum, the main barrier of human skin. Also, the dissolution of these microneedles in excised human skin and the concentration of ciprofloxacin in each layer of the excised human skin was studied. We designed an in vitro model of skin infection to compare the microneedles with free gel and, consequently, the antimicrobial activity of ciprofloxacin-loaded polymeric microneedles against *S. aureus*. Agarose gel, a transparent gelatinous substance composed of a carbohydrate polymer extracted from certain red seaweed, was proposed in recent studies as an in vitro model for the mechanical properties of the human skin [22,23]. Gelatinous substances can interact with water, which allows one to control various physical, mechanical, and chemical properties of the artificial skin, such as hardness, and surface properties [24]. Therefore, agarose gel was utilized as artificial skin and was subsequently treated with inoculum of *Staphylococcus aureus* to study the antibacterial activity of ciprofloxacin-loaded polymeric microneedles.

To assess the distribution of CIP in dermal layers after microneedle application, the cryostatic microtome technique was utilized. This technique is based on freezing excised skin samples and slicing them using a microtome for microscopic examination and analysis. The optimal critical temperature (O.C.T) compound is used to stabilize the skin during sectioning below −10 °C [25-27]. The sliced layers were analyzed for CIP content in a similar manner to that described in [25].

Experimental

Materials

Ciprofloxacin hydrochloride, PVA, PVP, acetonitrile, phosphoric acid, triethylamine, and phosphate buffer tablets were purchased from Merck, Germany. *Staphylococcus aureus* (ATCC-29213) was purchased from ATCC, USA. Poly(dimethyl-

siloxane) (PDMS) molds, including 196 laser-engineered pyramidal holes measuring 200 µm in depth and 50 µm base diameter were procured from Micropoint company, Singapore. Parafilm-M (thickness 0.13 mm) was purchased from Merck, Germany. HPLC-grade double-distilled water was used. O.C.T compound clear was obtained from Agar Scientific, UK.

Analysis of ciprofloxacin content in needles and skin

The analysis of ciprofloxacin was adopted from the United States Pharmacopoeia (USP) and was performed using HPLC (Shimadzu HPLC, model LC-2030C PLUS 3D). The system included an integrated solvent and degasser, an analytical pump, a thermostatic autosampler, a UV detector, and a thermostatic column compartment. Data acquisition was performed via the LabSolutions LCGC software. The eluent was detected at 278 nm. Separation was carried out using a reversed-phase Interclone C18 column (250 mm × 4.6 mm, 5 µm particle ODS 100 Å size) (Phenomenex, California, USA) at 30 °C. The mobile phase had an isocratic composition of 0.025 M phosphoric acid (pH 3.0 ± 0.1) previously adjusted with triethylamine/acetonitrile (80:20 v/v), eluted at a flow rate of 1.5 mL/min. The injection volume was 20 µL. The drug concentration was then determined according to a calibration curve. The calibration curve was plotted by correlating the peak area measured with known concentrations of ciprofloxacin samples. All measurements were conducted in triplicate to calculate mean values and standard deviations.

Preparation of ciprofloxacin-loaded polymeric microneedles

20% PVA (w/w) and 60% (w/w) PVP aqueous solutions were prepared by heating at 70 °C while stirring the solution with a magnetic stirrer (IKA-Werke GmbH & Co. KG, Staufen, Germany). Microneedles were prepared via a two-layer centrifugation method, as shown in Figure 1. Briefly, 10 mg CIP and 9 g of aqueous 20% w/w PVA/60% w/w PVP (9:1 weight ratio) or 9 g of 20% w/w PVA alone were stirred using a magnetic stirrer at 70 °C. Next, the mixture of CIP and PVA or PVA/PVP was centrifuged at 145*g* for 5 min (Eppendorf Centrifuge 5804, Merck KGaA, Darmstadt, Germany) to remove the air bubbles. The resulting mixture was then poured into 14 × 14, poly(dimethylsiloxane) (PDMS) molds (Micropoint company, Singapore). Each hole in the mold was 200 µm in depth and 50 µm diameter. The molds were then centrifuged at 1370*g* for 20 min to allow the polymer solution to fill the mold holes. Excess mixture was removed by scraping with a spatula and the molds was left for 5 h to dry. The aqueous baseplate solution of 20% w/w PVA (with no drug) was poured on the molds and centrifuged for 20 min at 699*g*. Next day, the dried microneedles were peeled from the mold gently. Blank microneedles were prepared in a similar manner without the ad-

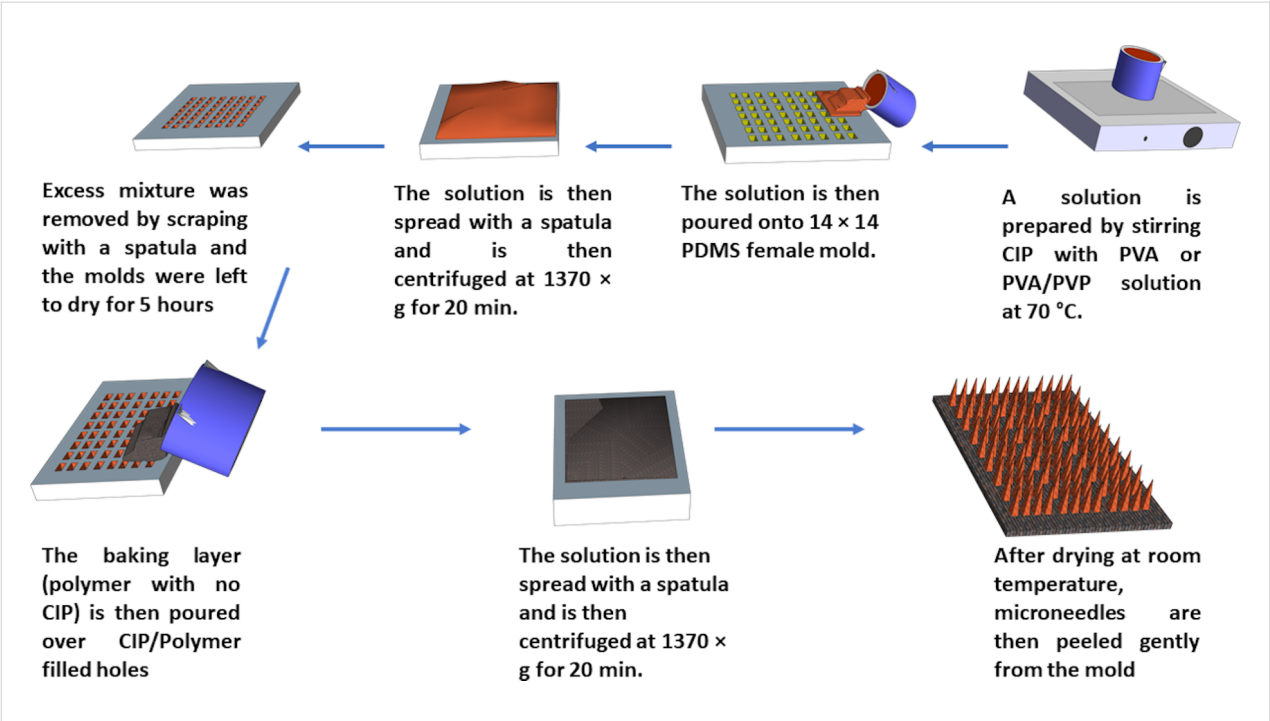


Figure 1: Microneedle fabrication using the two-layer centrifugation method. PVA/PVP or PVA gel with ciprofloxacin is stirred at 70 °C and poured on 14 × 14 PDMS mold and spread with a spatula. The mold is then centrifuged to fill the mold holes. The baking layer, which is free of the drug, is then spread over the mold, centrifuged, and allowed to dry forming polymeric microneedles.

dition of CIP to the PVA or PVA/PVP solution in the initial step.

Microneedle characterization

The shape and dimensions of CIP_MN1 and CIP_MN2 arrays were examined using a digital light microscope (Swift SW380B, China). Studying the mechanical strength of the microneedles, heights before compression were first measured. After pressing the microneedle arrays by thumb for 30 s, the microneedle heights were measured again.

Preparation of artificial agarose skin

Previously, agarose gel was utilized as an artificial skin model [28]. Briefly, 2.5 g of agarose was suspended in 100 mL water. The dispersion was then placed in the microwave to melt for 2 min. The solution is then loaded into a 6-well plate with a thickness of 2 mm and incubated at room temperature for 1 h to solidify. The gel was then removed from the wells and used to study the insertion properties and for in vitro infection assay.

Preparation of excised human skin samples

The excised human skin specimen was obtained from Shmeisani hospital under ethical approval No. UPR. 101/6-45. The consent of the skin donor, a 38 year-old female, was verbally granted when undergoing abdominal plastic surgery. She had the option to dump the specimen or donate it for scientific research. Her consent was granted before and after surgery and was witnessed by the surgeon. The skin was obtained from Al-Shmeisani hospital immediately after the surgery and treated as previously obtained specimens [29]. Specimens were defatted using a scalpel, cleaned by tapping with dry wipes and placed on paperboard wrapped with aluminum foil with the skin surface facing upward. Then, the skin was covered with aluminum foil, kept in zipper plastic bags, and subsequently stored at −70 °C for a maximum period of 6 months.

Microneedle dissolution in the skin

Prior to use, skin specimens were equilibrated in 1× phosphate-buffered saline (PBS), pH 7.4, for 15 min. A section of full-thickness human skin was placed, with the stratum corneum facing upward, onto a piece of tissue paper soaked with PBS in a weighing boat. CIP_MN1 were adhered to a piece of plastic tape and manually applied to the skin. To prevent the skin from drying out, another inverted weighing boat was placed on the top of the weighing boat containing the skin specimen and sealed with plastic tape. At predefined time points, CIP_MN1 were withdrawn from the skin and their heights were measured using the digital microscope.

Skin deposition studies

This study was conducted in a manner analogous to the procedure in [25]. Briefly, CIP_MN1 were inserted into the full-thickness human skin using finger press applied to the microneedle baseplate for 30 s. As shown in Figure 2, a cylin-

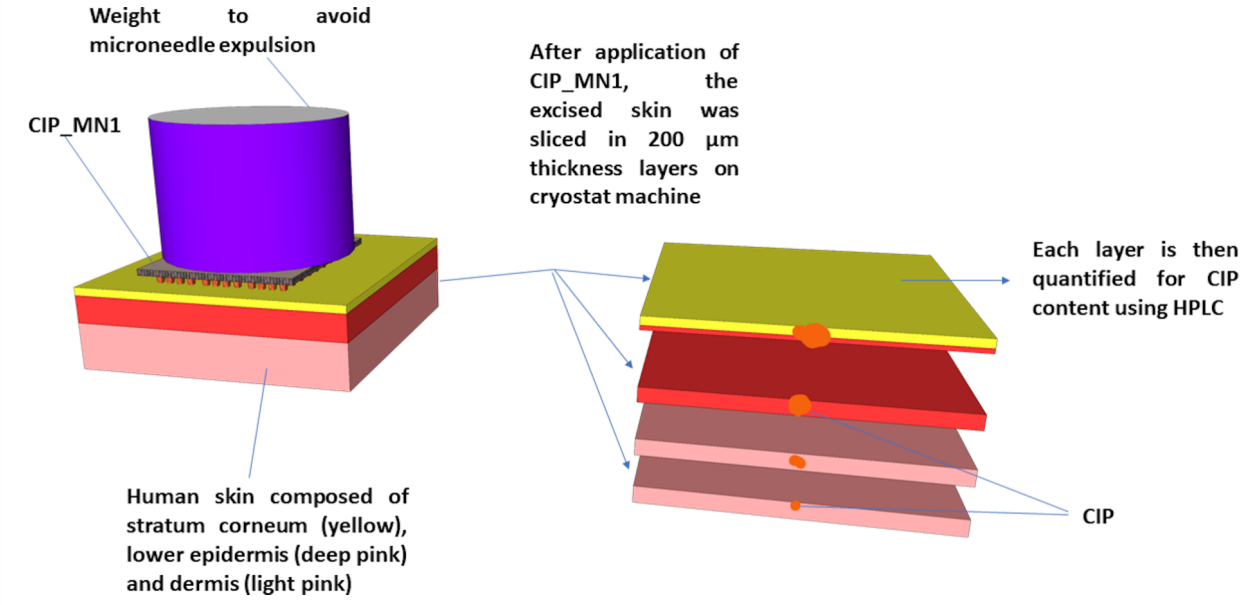


Figure 2: Schematic presentation of the skin deposition study of CIP_MN1. The full-thickness human skin was excised and treated. CIP_MN1 was then inserted into the skin using finger pressure applied to the microneedle baseplate for 30 s. A cylindrical 10 g stainless steel weight was placed on top of CIP_MN1 array to prevent expulsion of the microneedles, and the tissue paper was frequently wetted with PBS to prevent the skin from drying out. At each predefined time point, CIP_MN1 was removed, and the skin was sliced using a cryostatic microtome.

drical 10 g stainless steel weight was placed on top of the CIP_MN1 and the tissue paper was frequently soaked with PBS to prevent the skin from drying out. At each predefined time point, CIP_MN1 were removed, the skin was placed on dental wax and 1 cm^2 of skin was excised using a cork borer. The skin was then fully immersed in O.C.T media and frozen in liquid nitrogen. The frozen skin was then sliced horizontally into layers of 200 µm using a cryostatic microtome (Leica CM1900-1-1 cryostatic microtome, Leica Microsystems, Nussloch, Germany). Ciprofloxacin was then extracted from skin specimens with 1 mL acetonitrile via sonication for 4 h and centrifugation for 20 min at 10,000*g* (Eppendorf 5425, UK). All samples were analyzed using the developed reverse-phase HPLC method. The drug distribution resulting from the control was studied in the same manner except that, instead of inserting a ciprofloxacin microneedle array, free gel containing an equivalent amount of ciprofloxacin was placed on top of the skin, followed by the stainless steel weight for consistency.

Antimicrobial activity: in vitro infection study

S. aureus (ATCC-29213) inoculum equivalent to 0.5 MacFarland (ca. 1 × 10^8 CFU/mL) turbidity was prepared from an overnight culture. A sterile swab was dipped in the preadjusted inoculum and the excess fluid was expressed. This swab was used to streak the entire surface of nutrient agar plate (Oxoid, UK) (CLSI, 2013). An artificial agarose-based skin (9.5 cm^2) was put on top of the inoculated agar. Then CIP_MN1, free ciprofloxacin gel, or blank microneedles were put on the surface of the artificial skin. After incubation for 24 h at 37 °C, microneedles loaded with ciprofloxacin (CIP_MN), free gel (with equivalent drug concentration to the microneedles), and blank microneedles (free from drug) were removed, the artificial skin was removed, and the zone of inhibition was measured in millimeters using a ruler (Figure 3).

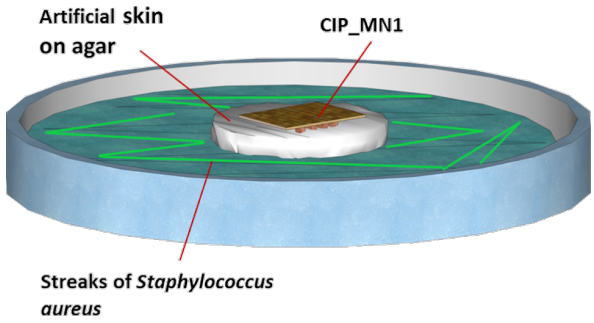


Figure 3: In vitro model for the antimicrobial activity of CIP_MN1. Preincubated inoculum of *S. aureus* is streaked over an agar plate. An artificial agarose-based skin is then put on the top of the agar. A microneedle array of ciprofloxacin, free ciprofloxacin gel, or blank microneedles were put on the surface of the agar. After incubation for 24 h, CIP_MN1, free CIP gel, or blank microneedles were removed, and the zone of inhibition was measured in millimeters using a ruler.

Statistical analysis

The results are presented as means ± standard deviation. Statistical comparison between microneedles and free CIP gel, in terms of ciprofloxacin permeation, was made using GraphPad Prism software (ver. 9; GraphPad, Inc. San Diego, CA, USA). A two-tailed Student's *t*-test was used to compare different pairs of data. One-way and two-way analysis of variance (ANOVA) was used in the skin disposition study to compare the effects of different formulations and/or times of incubation. Rejection of the null hypothesis was considered when $p < 0.05$.

Results and Discussion

Microneedles characterization

The polymeric microneedles were prepared using a mixture of PVA and PVP, or PVA alone. Size and shape were examined using a light microscope. The microneedles showed a pyramidal appearance with an average microneedle height of 188 ± 11 µm and an average square base diameter 49.5 ± 3.4 µm for the formulation of PVA/PVP (9:1) (CIP_MN1). CIP_MN2 showed a microneedle height of 179 ± 16 µm and a square base diameter of 44.2 ± 7.1 µm. As shown in Figure 4, the tips of the microneedles were sharp with less than 5 µm tip diameter. In a previous study, sharp tips with 5 µm tip diameter were required for smooth skin penetration, in contrast to needles with a larger tip diameter (15 µm or more), which showed sudden increase in depth after initial superficial penetration [30]. Moreover, in another study, the square base of the microneedles was shown to cause deeper penetration compared to hexagonal bases [31]. The shape of the microneedles in our study was faceted pyramidal due to the use of the pyramidal PDMS mold in the microneedle preparation. The faceted appearance of the CIP_MN1 and CIP_MN2 microneedles was attributed to the shrinkage of the polymer gel upon drying as suggested by previous studies [32,33]. A similarly faceted shape of microneedles was observed with polymeric microneedles made of chitosan and alginate [34]. Also, a similar microneedle shape was obtained using hydroxypropyl methyl cellulose and PVA as the matrix blend of the microneedles [35]. The CIP content in our study was 170 µg per array for CIP_MN1 and 182 µg per array for CIP_MN2.

Microneedle penetration capabilities

To assess the skin penetration capabilities of CIP_MN1 and CIP_MN2, we utilized Parafilm as a model to simulate human skin. Parafilm has been proposed as a model that simulates the mechanical properties of porcine skin [36], which is similar in barrier properties to human skin [37]. In a study to assess the insertion depth of microneedles in Parafilm, no significant difference was shown in the insertion depth between porcine skin and Parafilm for insertion forces of 10 and 40 N [36]. In a recent study, Parafilm was also studied as a model that simu-

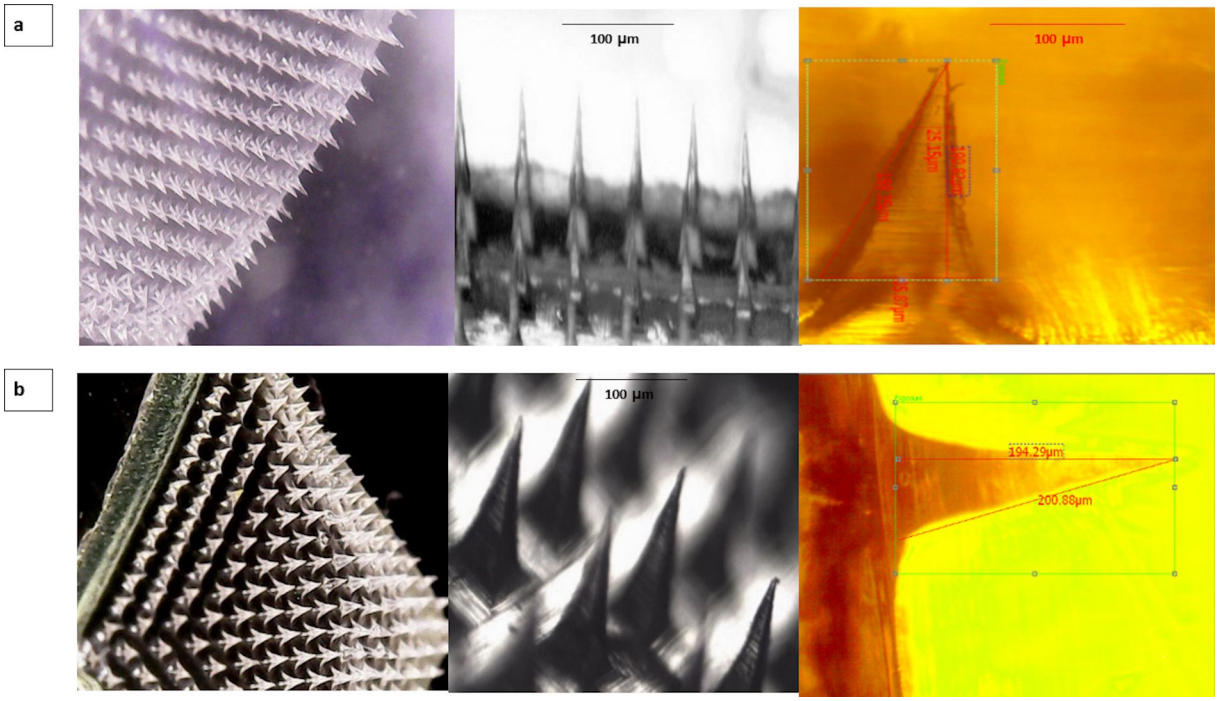


Figure 4: Microneedle visualization for two formulations; (a) CIP_MN1 images under digital light microscope, and (b) CIP_MN2 images under digital light microscope.

lates the mechanical and dissolution properties of mammalian skin [38]. Therefore, the ability of the microneedles to penetrate the Parafilm is an indication that microneedles are capable of penetrating human skin. The thickness of the Parafilm is 130 µm. Therefore, the ability of CIP_MN1 to fully puncture Parafilm is an indication that these microneedles can potentially fully penetrate the skin when applied.

CIP_MN1 gave a complete array of perforations for the first layer of Parafilm, which means that the microneedles can reach 130 µm, as shown in Figure 5 and Table 1. However, CIP_MN2 showed significantly fewer perforations compared to the CIP_MN1; the first layer of Parafilm was perforated only by 85 needles. Although PVA hydrogel has shown satisfactory mechani-

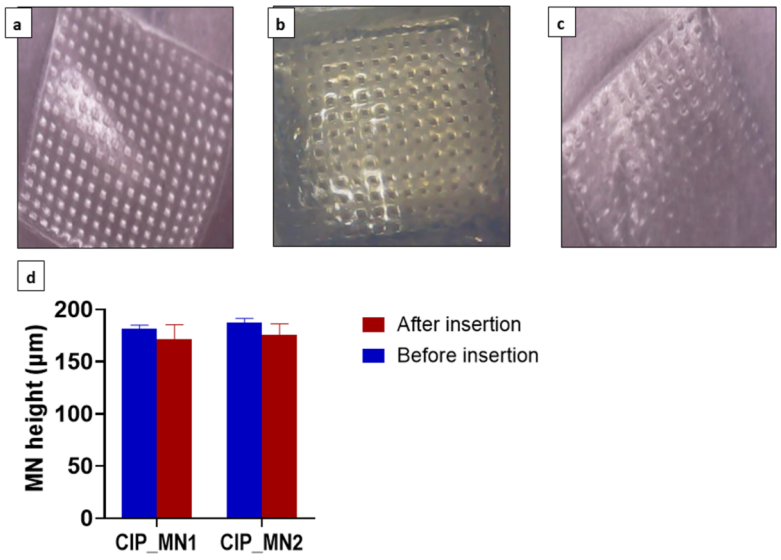


Figure 5: (a) Parafilm penetration with CIP_MN1 microneedles; (b) artificial skin (agarose-based) penetration with CIP_MN1; (c) Parafilm penetration with CIP_MN2 microneedles; (d) heights of CIP_MN1 and CIP_MN2 before and after compression with a thumb press for 30 s, n = 3.

Table 1: Physical characteristics of CIP_MN1 and CIP_MN2, that is, height, diameter, CIP content, and number of pores in Parafilm after insertion, n = 3.

	Microneedle height (µm)	Microneedles diameter (µm)	CIP content (µg/array)	Number of pores in Parafilm after insertion
CIP_MN1	188 ± 11	49.5 ± 3.4	170 ± 39	190 ± 3
CIP_MN2	179 ± 16	44.2 ± 7.1	182 ± 45	85 ± 12

cal properties of PVA/PVP hydrogels [39-41]. In one study, the tensile strength of PVA hydrogel was increased by 133% after blending with less than 2% w/w PVP [42]. This is due to the formation of relatively strong hydrogen bonds between the hydroxy groups of PVA and the carbonyl groups of PVP in an intertwined network [43]. Therefore, we assumed that CIP_MN1 composed of PVA/PVP hydrogel had greater mechanical strength than CIP_MN2 composed of PVA and penetrated the Parafilm more efficiently. Overall, the results we obtained signify the superiority of the CIP_MN1 formulation, which was chosen to be investigated further.

Next the penetration capabilities of CIP_MN1 were studied using the in vitro skin model composed of 2.5% agarose gel. Agarose gel is widely used in wound healing for skin regeneration due to its mechanical properties that resemble those of human skin [44,45]. Additionally, using an agarose-based in vitro skin model can help to reduce the skin structure variability to obtain more consistent and reproducible lab results [46]. The 2.5% agarose gel as an artificial skin model revealed penetration of the CIP_MN1 microneedle array, as shown in Figure 5.

The ability of microneedles to withstand the insertion force is crucial in topical and transdermal delivery systems [47]. Compressing the microneedles with a thumb press revealed no significant difference in the height of CIP_MN1 or CIP_MN2 before and after thumb press for 30 s on excised human skin. This indicates that both microneedle formulations withstand the insertion force required for microneedle application on skin. We used thumb press to study the tensile strength of the microneedles since, previously, dissolving polymeric microneedles composed of PVA have been shown to withstand insertion forces equivalent to thumb press [25]. Also, several research studies have used gentle thumb press for in vitro and ex vivo topical/transdermal delivery studies [48-50]. Dissolving microneedles, particularly made of PVP and PVA, have been shown to withstand the required insertion force in skin [51,52].

Microneedle dissolution in human skin

The dissolution of CIP_MN1 in human skin showed a gradual decrease in the microneedle length with time. The microneedles required one hour for complete dissolution in the skin as shown in Figure 6. The dissolution of CIP_MN1 was consistent with previous studies. In a recent study on the dissolution of microneedles, PVA-based microneedles have shown to dissolve in porcine skin over a period of 40 min [53]. In another study, PVP/PVA-based microneedles showed to dissolve in the skin of rats within one hour from application [54].

Skin deposition study

One-way ANOVA analysis showed a significant difference in the permeation of ciprofloxacin between the free CIP gel and CIP_MN1, after one hour and after 12 h (P value = 0.015). Moreover, the results also showed that the deposition of the incorporated drug into deeper layers could be enhanced by the microneedle delivery system. As shown in Figure 7, ciprofloxacin in CIP_MN1 appeared to migrate to a deeper layer compared to ciprofloxacin in free gel. Ciprofloxacin released from CIP_MN1 permeated to a depth of more than 500 µm compared to less than 200 µm from free gel. The results also showed that ciprofloxacin released from CIP_MN1 appeared to decrease with time in the upper layers and to increase in deeper layers, as shown by comparing the deposition of ciprofloxacin after 1 h and after 12 h. This was evidenced by p = 0.044 in a two-way ANOVA analysis for the interaction between skin depth and ciprofloxacin content.

In our skin deposition study, ciprofloxacin was able to migrate deeper than 500 µm after application (CIP_MN1 on excised human skin sample), which means that ciprofloxacin already passed the epidermis and reached the dermis, since the epidermis thickness is generally less than 10–80 µm. Microneedles that can reach deeper than 80 µm can potentially deliver the incorporated drug for the treatment of local and systemic infections [55].

The dermis is a viable layer that is rich in water, blood capillaries, and connective tissues including collagen and elastin [56]. These properties can facilitate the diffusion into the dermis and underlying layers for local and transdermal effects. In a recent study, PVP-based dissolving microneedles were able to deliver sinomenine hydrochloride to a skin depth of 200 µm in

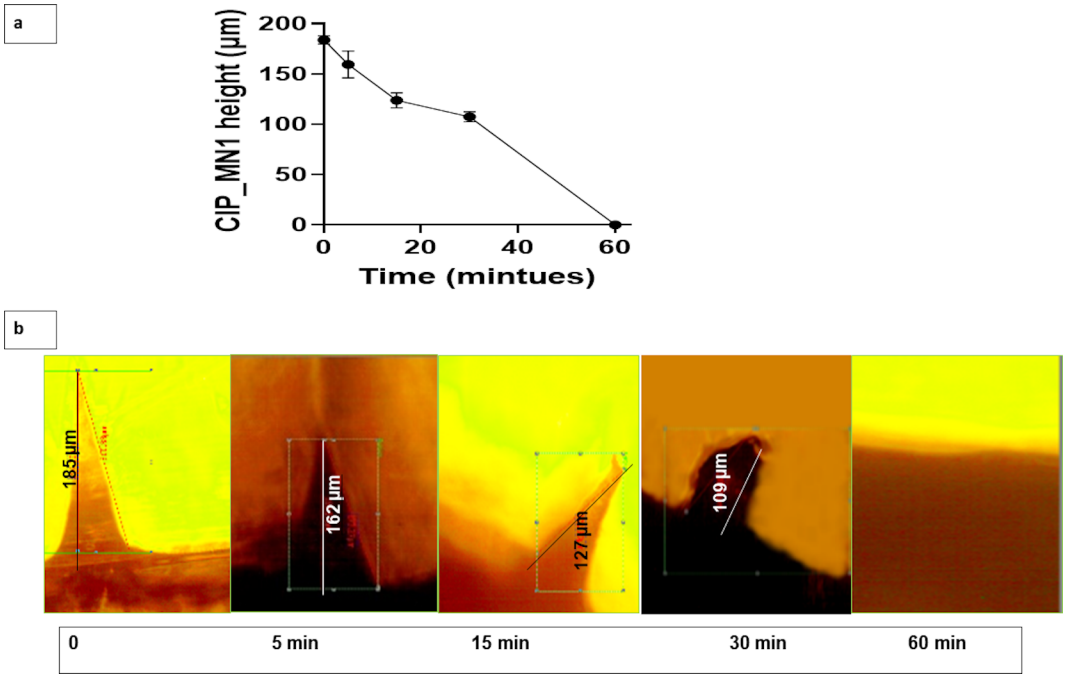


Figure 6: (a) CIP_MN1 dissolution in excised human skin over time (represented by CIP_MN1 height decease with time), $n = 3$; (b) microscopic image of CIP_MN1 at 0, 5, 15, 30, and 60 min after insertion in excised human skin.

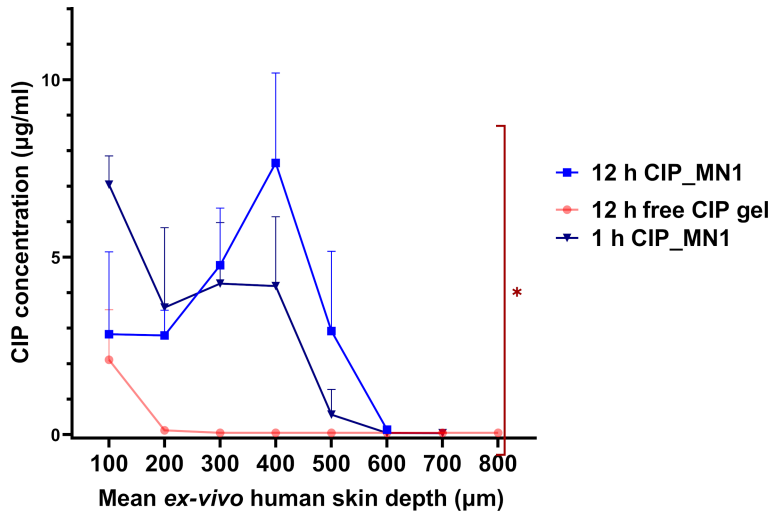


Figure 7: Ciprofloxacin skin deposition from CIP_MN1 after 1 h and 12 h from insertion, and from free gel after 12 h from application, into different depth distances. *$P < 0.05$ for one-way ANOVA between 12 h CIP_MN1, 1 h CIP_MN1, and free CIP gel; $n = 4$.

rats [57], which is significantly less than the depth that we achieved. In another study showing the efficiency of dissolving microneedles in transdermal delivery, the contraceptive hormone levonorgestrel was released and migrated through the entire skin structure, maintaining a quantifiable plasma concentration for up to 60 days [58].

Antibacterial activity of CIP_MN1

Skin models are generally less expensive, provide a solution to the limited availability of fresh human skin samples, and increase safety of handling [59]. Also, utilizing an in vitro skin model with definite bacterial inoculum can reduce the inter- and intra-individual variability in mechanical properties of human

skin [60]. After incubation of the artificial skin with the *S. aureus*, a bacterial lawn was obviously formed beneath the untreated skin. As shown in Figure 8, when samples were applied over the artificial skin, a zone of inhibition of 29 mm was observed for CIP_MN1, and one of 2 mm was observed for free ciprofloxacin gel, indicating that ciprofloxacin was able to permeate the artificial skin layer significantly better than the free CIP gel ($p < 0.0001$). No zone of inhibition was observed for the untreated group and the blank microneedles.

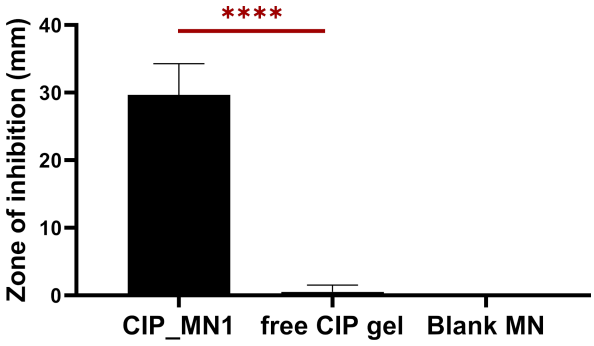


Figure 8: Antibacterial activity of CIP_MN1 applied on an in vitro skin model mounted on *S. aureus*-inoculated agar. ****$p < 0.0001$; $n = 3$.

CIP-loaded microneedles were studied on three substrates, namely Parafilm, 2.5% agarose, and excised human skin. A summary of the experiments and the principal results is given in Table 2.

Conclusion

This study investigated the potential of ciprofloxacin-loaded dissolving microneedles based on PVA and PVP as copolymers for the treatment of *S. aureus* skin infections. The PVA/PVP-based dissolving microneedles were studied regarding drug content, mechanical strength, perforation of Parafilm and an agarose-based skin model, dissolution in excised human skin, and antibacterial activity in the agarose-based skin model infected with *S. aureus*. The results suggest that PVA/PVP microneedles were able to withstand the insertion force and to fully penetrate Parafilm and agarose gel. Moreover, the superiority of this delivery system over conventional administration of free gel in excised human skin and in an in vitro skin infection model was demonstrated. This can be of great benefit for the painless topical/transdermal delivery of antibiotics, overcoming the barrier properties of the skin.

Acknowledgements

We thank Dr. Mahmoud Bataineh from Shmeisani hospital for facilitating the obtaining of the excised human skin.

Funding

This study is funded by the Deanship of Scientific Research, University of Jordan (Project NO. 2146).

Table 2: CIP_MN1 and CIP_MN2 penetration capabilities with the rationale of the experiment and the principal outcomes.

Experiment	Substrate	Rationale	Principle results of our study
microneedle penetration capabilities	Parafilm	The penetration depth in Parafilm is similar to the penetration depth in porcine skin and human skin [36,37].	CIP_MN1 showed 190 perforations compared to 85 perforations of CIP_MN2
	2.5% agarose gel in vitro skin model	Agarose gel has shown mechanical properties similar to those of human skin [22,23].	CIP_MN1 (which was used in subsequent skin dissolution and deposition studies) showed complete perforation on 2.5% agarose gel.
antibacterial activity of CIP_MN1 vs free CIP gel	2.5% agarose gel in vitro skin model infected with *Staphylococcus aureus*	Agarose in vitro skin model reduces the inter- and intra-individual variability and is also less expensive and widely available [46].	CIP_MN1 showed a significantly larger zone of inhibition (29 mm) than free gel (2 mm).
dissolution of CIP_MN1 in human skin	excised human skin	Using excised human skin is feasible and requires less strict ethical issue compared to a clinical study. Moreover, excised human skin study provides minimal differences to in vivo conditions [61].	CIP_MN1 showed complete dissolution in the skin one hour after application.
deposition of CIP in the dermal layers			Ciprofloxacin released from CIP_MN1 permeated to a depth of more than 500 µm compared to ciprofloxacin from free gel, which permeated less than 200 µm in depth.

ORCID® iDs

Sharif Abdelghany - https://orcid.org/0000-0002-7446-4436
Walhan Alshaer - https://orcid.org/0000-0003-2946-7328
Yazan Al Thaher - https://orcid.org/0000-0002-1643-6605

References

1. Alkilani, A. Z.; McCrudden, M. T. C.; Donnelly, R. F. *Pharmaceutics* **2015,** *7,* 438–470. doi:10.3390/pharmaceutics7040438
2. Waghule, T.; Singhvi, G.; Dubey, S. K.; Pandey, M. M.; Gupta, G.; Singh, M.; Dua, K. *Biomed. Pharmacother.* **2019,** *109,* 1249–1258. doi:10.1016/j.biopha.2018.10.078
3. Homayun, B.; Lin, X.; Choi, H.-J. *Pharmaceutics* **2019,** *11,* 129. doi:10.3390/pharmaceutics11030129
4. Bachmann-Mennengaa, B.; Ohlmer, A.; Heesen, M. *Arzneim. Forsch.* **2003,** *53,* 621–626. doi:10.1055/s-0031-1297158
5. Ita, K. *Biomed. Pharmacother.* **2017,** *93,* 1116–1127. doi:10.1016/j.biopha.2017.07.019
6. Permana, A. D.; Paredes, A. J.; Volpe-Zanutto, F.; Anjani, Q. K.; Utomo, E.; Donnelly, R. F. *Eur. J. Pharm. Biopharm.* **2020,** *154,* 50–61. doi:10.1016/j.ejpb.2020.06.025
7. Permana, A. D.; Mir, M.; Utomo, E.; Donnelly, R. F. *Int. J. Pharm.: X* **2020,** *2,* 100047. doi:10.1016/j.ijpx.2020.100047
8. Sullivan, T.; de Barra, E. *Clin. Med. J.* **2018,** *18,* 160–163. doi:10.7861/clinmedicine.18-2-160
9. Raff, A. B.; Kroshinsky, D. *JAMA, J. Am. Med. Assoc.* **2016,** *316,* 325–337. doi:10.1001/jama.2016.8825
10. Chira, S.; Miller, L. G. *Epidemiol. Infect.* **2010,** *138,* 313–317. doi:10.1017/s0950268809990483
11. Borschitz, T.; Schlicht, S.; Siegel, E.; Hanke, E.; von Stebut, E. *PLoS One* **2015,** *10,* e0132775. doi:10.1371/journal.pone.0132775
12. Fass, R. J. *Postgrad. Med.* **1990,** *87,* 117–131. doi:10.1080/00325481.1990.11704677
13. LeBel, M. *Pharmacotherapy* **1988,** *8,* 3–30. doi:10.1002/j.1875-9114.1988.tb04058.x
14. Davis, R.; Markham, A.; Balfour, J. A. *Drugs* **1996,** *51,* 1019–1074. doi:10.2165/00003495-199651060-00010
15. Esposito, S.; Bassetti, M.; Borre, S.; Bouza, E.; Dryden, M.; Fantoni, M.; Gould, I. M.; Leoncini, F.; Leone, S.; Milkovich, G.; Nathwani, D.; Segreti, J.; Sganga, G.; Unal, S.; Venditti, M. *J. Chemother. (Abingdon, U. K.)* **2011,** *23,* 251–262. doi:10.1179/joc.2011.23.5.251
16. Fass, R. J. *J. Antimicrob. Chemother.* **1986,** *18* (Suppl. D), 153–157. doi:10.1093/jac/18.supplement_d.153
17. Ball, P. *J. Antimicrob. Chemother.* **1986,** *18* (Suppl. D), 187–193. doi:10.1093/jac/18.sd.187
18. Ahmed Saeed AL-Japairai, K.; Mahmood, S.; Hamed Almurisi, S.; Reddy Venugopal, J.; Rebhi Hilles, A.; Azmana, M.; Raman, S. *Int. J. Pharm.* **2020,** *587,* 119673. doi:10.1016/j.ijpharm.2020.119673
19. Dalvi, M.; Kharat, P.; Thakor, P.; Bhavana, V.; Singh, S. B.; Mehra, N. K. *Life Sci.* **2021,** *284,* 119877. doi:10.1016/j.lfs.2021.119877
20. Ziesmer, J.; Tajpara, P.; Hempel, N.-J.; Ehrström, M.; Melican, K.; Eidsmo, L.; Sotiriou, G. A. *Adv. Mater. Technol. (Weinheim, Ger.)* **2021,** *6,* 2001307. doi:10.1002/admt.202001307
21. Kim, Y. S.; Yang, Y.; Henry, C. S. *Sens. Actuators, B* **2018,** *255,* 3654–3661. doi:10.1016/j.snb.2017.10.005
22. Dąbrowska, A. K.; Rotaru, G.-M.; Derler, S.; Spano, F.; Camenzind, M.; Annaheim, S.; Stämpfli, R.; Schmid, M.; Rossi, R. M. *Skin Res. Technol.* **2016,** *22,* 3–14. doi:10.1111/srt.12235
23. Fonseca, D. F. S.; Costa, P. C.; Almeida, I. F.; Dias-Pereira, P.; Correia-Sá, I.; Bastos, V.; Oliveira, H.; Vilela, C.; Silvestre, A. J. D.; Freire, C. S. R. *Macromol. Biosci.* **2020,** *20,* 2000195. doi:10.1002/mabi.202000195
24. Kozlov, P. V.; Burdygina, G. I. *Polymer* **1983,** *24,* 651–666. doi:10.1016/0032-3861(83)90001-0
25. Abdelghany, S.; Tekko, I. A.; Vora, L.; Larrañeta, E.; Permana, A. D.; Donnelly, R. F. *Pharmaceutics* **2019,** *11,* 308. doi:10.3390/pharmaceutics11070308
26. Hanke, C. W.; Lee, M. W. *Dermatol. Surg.* **1989,** *15,* 29–32. doi:10.1111/j.1524-4725.1989.tb03109.x
27. Ishii, T.; Kasama, K.; Kondo, M.; Takahashi, T. *Tohoku J. Exp. Med.* **1993,** *171,* 101–105. doi:10.1620/tjem.171.101
28. Zhang, D.; Das, D. B.; Rielly, C. D. *J. Pharm. Sci.* **2014,** *103,* 613–627. doi:10.1002/jps.23835
29. Mansour, R. S. H.; Hamdan, I. I.; Salem, M. S. H.; Khalil, E. A.; Sallam, A. A. *PLoS One* **2021,** *16,* e0247879. doi:10.1371/journal.pone.0247879
30. Römgens, A. M.; Bader, D. L.; Bouwstra, J. A.; Baaijens, F. P. T.; Oomens, C. W. J. *J. Mech. Behav. Biomed. Mater.* **2014,** *40,* 397–405. doi:10.1016/j.jmbbm.2014.09.015
31. Loizidou, E. Z.; Inoue, N. T.; Ashton-Barnett, J.; Barrow, D. A.; Allender, C. J. *Eur. J. Pharm. Biopharm.* **2016,** *107,* 1–6. doi:10.1016/j.ejpb.2016.06.023
32. Kudo, K.; Ishida, J.; Syuu, G.; Sekine, Y.; Ikeda-Fukazawa, T. *J. Chem. Phys.* **2014,** *140,* 044909. doi:10.1063/1.4862996
33. Jang, H.; Choi, H.; Jeong, H.; Baek, S.; Han, S.; Chung, D. J.; Lee, H. S. *Macromol. Res.* **2018,** *26,* 151–156. doi:10.1007/s13233-018-6031-2
34. Arshad, M. S.; Hassan, S.; Hussain, A.; Abbas, N.; Kucuk, I.; Nazari, K.; Ali, R.; Ramzan, S.; Alqahtani, A.; Andriotis, E. G.; Fatouros, D. G.; Chang, M.-W.; Ahmad, Z. *Daru, J. Pharm. Sci.* **2019,** *27,* 673–681. doi:10.1007/s40199-019-00301-3
35. He, M.; Yang, G.; Zhang, S.; Zhao, X.; Gao, Y. *J. Pharm. Sci.* **2018,** *107,* 1037–1045. doi:10.1016/j.xphs.2017.11.013
36. Larrañeta, E.; Moore, J.; Vicente-Pérez, E. M.; González-Vázquez, P.; Lutton, R.; Woolfson, A. D.; Donnelly, R. F. *Int. J. Pharm.* **2014,** *472,* 65–73. doi:10.1016/j.ijpharm.2014.05.042
37. Ranamukhaarachchi, S. A.; Lehnert, S.; Ranamukhaarachchi, S. L.; Sprenger, L.; Schneider, T.; Mansoor, I.; Rai, K.; Häfeli, U. O.; Stoeber, B. *Sci. Rep.* **2016,** *6,* 32074. doi:10.1038/srep32074
38. Berzosa, M.; Nemeskalova, A.; Zúñiga-Ripa, A.; Salvador-Bescós, M.; Larrañeta, E.; Donnelly, R. F.; Gamazo, C.; Irache, J. M. *Pharmaceutics* **2022,** *14,* 239. doi:10.3390/pharmaceutics14020239
39. Rajesh, K.; Crasta, V.; Rithin Kumar, N. B.; Shetty, G.; Rekha, P. D. *J. Polym. Res.* **2019,** *26,* 99. doi:10.1007/s10965-019-1762-0
40. Teodorescu, M.; Morariu, S.; Bercea, M.; Săcărescu, L. *RSC Adv.* **2016,** *6,* 39718–39727. doi:10.1039/c6ra04319d
41. Zheng, Y.; Huang, X.; Wang, Y.; Xu, H.; Chen, X. *J. Appl. Polym. Sci.* **2009,** *113,* 736–741. doi:10.1002/app.29326
42. Huang, Y.; Zheng, Y.; Song, W.; Ma, Y.; Wu, J.; Fan, L. *Composites, Part A* **2011,** *42,* 1398–1405. doi:10.1016/j.compositesa.2011.06.003
43. Morariu, S.; Bercea, M.; Teodorescu, M.; Avadanei, M. *Eur. Polym. J.* **2016,** *84,* 313–325. doi:10.1016/j.eurpolymj.2016.09.033
44. Ying, R.; Huang, W.-C.; Mao, X. *ACS Biomater. Sci. Eng.* **2022,** *8,* 293–302. doi:10.1021/acsbiomaterials.1c01215
45. Su, T.; Zhang, M.; Zeng, Q.; Pan, W.; Huang, Y.; Qian, Y.; Dong, W.; Qi, X.; Shen, J. *Bioact. Mater.* **2021,** *6,* 579–588. doi:10.1016/j.bioactmat.2020.09.004

46. Roger, M.; Fullard, N.; Costello, L.; Bradbury, S.; Markiewicz, E.; O'Reilly, S.; Darling, N.; Ritchie, P.; Määttä, A.; Karakesisoglou, I.; Nelson, G.; von Zglinicki, T.; Dicolandrea, T.; Isfort, R.; Bascom, C.; Przyborski, S. *J. Anat.* **2019,** *234,* 438–455. doi:10.1111/joa.12942
47. Ita, K. *Pharmaceutics* **2015,** *7,* 90–105. doi:10.3390/pharmaceutics7030090
48. Johnson, A. R.; Caudill, C. L.; Tumbleston, J. R.; Bloomquist, C. J.; Moga, K. A.; Ermoshkin, A.; Shirvanyants, D.; Mecham, S. J.; Luft, J. C.; DeSimone, J. M. *PLoS One* **2016,** *11,* e0162518. doi:10.1371/journal.pone.0162518
49. Ye, R.; Yang, J.; Li, Y.; Zheng, Y.; Yang, J.; Li, Y.; Liu, B.; Jiang, L. *ACS Biomater. Sci. Eng.* **2020,** *6,* 2487–2494. doi:10.1021/acsbiomaterials.0c00120
50. Chinnadayyala, S. R.; Park, K. D.; Cho, S. *ECS J. Solid State Sci. Technol.* **2018,** *7,* Q3159–Q3171. doi:10.1149/2.0241807jss
51. Wang, Q. L.; Ren, J. W.; Chen, B. Z.; Jin, X.; Zhang, C. Y.; Guo, X. D. *J. Ind. Eng. Chem. (Amsterdam, Neth.)* **2018,** *59,* 251–258. doi:10.1016/j.jiec.2017.10.030
52. Zhang, N.; Zhou, X.; Liu, L.; Zhao, L.; Xie, H.; Yang, Z. *Front. Pharmacol.* **2021,** *12,* 719905. doi:10.3389/fphar.2021.719905
53. Nasiri, M. I.; Vora, L. K.; Ershaid, J. A.; Peng, K.; Tekko, I. A.; Donnelly, R. F. *Drug Delivery Transl. Res.* **2022,** *12,* 881–896. doi:10.1007/s13346-021-01107-0
54. Rabiei, M.; Kashanian, S.; Bahrami, G.; Derakhshankhah, H.; Barzegari, E.; Samavati, S. S.; McInnes, S. J. P. *Eur. J. Pharm. Sci.* **2021,** *167,* 106040. doi:10.1016/j.ejps.2021.106040
55. Andrews, S. N.; Jeong, E.; Prausnitz, M. R. *Pharm. Res.* **2013,** *30,* 1099–1109. doi:10.1007/s11095-012-0946-7
56. Dréno, B. *Ann. Dermatol. Venereol.* **2009,** *136,* S247–S251. doi:10.1016/s0151-9638(09)72527-x
57. Shu, Z.; Cao, Y.; Tao, Y.; Liang, X.; Wang, F.; Li, Z.; Li, Z.; Gui, S. *Drug Delivery* **2020,** *27,* 642–651. doi:10.1080/10717544.2020.1754524
58. Donnelly, R. F.; Larraňeta, E. *Nat. Biomed. Eng.* **2019,** *3,* 169–170. doi:10.1038/s41551-019-0369-4
59. Flaten, G. E.; Palac, Z.; Engesland, A.; Filipović-Grčić, J.; Vanić, Ž.; Škalko-Basnet, N. *Eur. J. Pharm. Sci.* **2015,** *75,* 10–24. doi:10.1016/j.ejps.2015.02.018
60. Jacquet, E.; Chambert, J.; Pauchot, J.; Sandoz, P. *Skin Res. Technol.* **2017,** *23,* 491–499. doi:10.1111/srt.12361
61. Gowing, G.; Svendsen, S.; Svendsen, C. N. *Prog. Brain Res.* **2017,** *230,* 99–132. doi:10.1016/bs.pbr.2016.11.003

License and Terms

This is an open access article licensed under the terms of the Beilstein-Institut Open Access License Agreement (https://www.beilstein-journals.org/bjnano/terms), which is identical to the Creative Commons Attribution 4.0 International License (https://creativecommons.org/licenses/by/4.0). The reuse of material under this license requires that the author(s), source and license are credited. Third-party material in this article could be subject to other licenses (typically indicated in the credit line), and in this case, users are required to obtain permission from the license holder to reuse the material.

The definitive version of this article is the electronic one which can be found at:
https://doi.org/10.3762/bjnano.13.43

BEILSTEIN JOURNAL OF NANOTECHNOLOGY

Fabrication and testing of polymer microneedles for transdermal drug delivery

Vahid Ebrahiminejad[1], Zahra Faraji Rad[*1], Philip D. Prewett[2,3] and Graham J. Davies[4,5]

Full Research Paper

Open Access

Address:
[1]School of Engineering, University of Southern Queensland, Springfield Central, QLD 4300, Australia, [2]Department of Mechanical Engineering, University of Birmingham, Birmingham B15 2TT, United Kingdom, [3]Oxacus Ltd., Dorchester-on-Thames, OX10 7HN, United Kingdom, [4]Faculty of Engineering, University of New South Wales, Sydney, NSW 2052, Australia and [5]College of Engineering & Physical Sciences, School of Engineering, University of Birmingham, Birmingham, B15 2TT, United Kingdom

Email:
Zahra Faraji Rad[*] - zahra.farajirad@usq.edu.au

* Corresponding author

Keywords:
hot embossing; microneedles; penetration efficiency; thermoplastic polymers; two-photon polymerization

Beilstein J. Nanotechnol. **2022,** *13,* 629–640.
https://doi.org/10.3762/bjnano.13.55

Received: 16 March 2022
Accepted: 30 June 2022
Published: 08 July 2022

This article is part of the thematic issue "Microneedles for vaccination and drug delivery".

Associate Editor: S. Giordani

© 2022 Ebrahiminejad et al.; licensee Beilstein-Institut.
License and terms: see end of document.

Abstract

Microneedle (MN) patches have considerable potential for medical applications such as transdermal drug delivery, point-of-care diagnostics, and vaccination. These miniature microdevices should successfully pierce the skin tissues while having enough stiffness to withstand the forces imposed by penetration. Developing low-cost and simple manufacturing processes for MNs is of considerable interest. This study reports a simple fabrication process for thermoplastic MNs from cycloolefin polymers (COP) using hot embossing on polydimethylsiloxane (PDMS) soft molds. COP has gained interest due to its high molding performance and low cost. The resin master MN arrays (9 × 9) were fabricated using two-photon polymerization (TPP). A previous gap in the detailed characterization of the embossing process was investigated, showing an average of 4.99 ± 0.35% longitudinal shrinkage and 2.15 ± 0.96% lateral enlargement in the molded MN replicas. The effects of bending, buckling, and tip blunting were then examined using compression tests and also theoretically. MN array insertion performance was studied in vitro on porcine back skin using both a prototype custom-made applicator and a commercial device. An adjustable skin stretcher mechanism was designed and manufactured to address current limitations for mimicking skin in vivo conditions. Finite element analysis (FEA) was developed to simulate single MN insertion into a multilayered skin model and validated experimentally using a commercial Pen Needle as a model for the thermoplastic MNs. Margins of safety for the current MN design demonstrated its potential for transdermal drug delivery and fluid sampling. Experimental results indicated significant penetration improvements using the prototype applicator, which produced array penetration efficiencies as high as >92%, depending on the impact velocity setting.

Introduction

During the past two decades, MN devices have become a promising tool for transdermal drug delivery, vaccination, and point-of-care diagnostics [1,2]. MNs are a painless and non-invasive method of drug delivery or sampling which can bypass the skin's outermost layer, the stratum corneum (SC), without stimulating nerves, causing irritation, or initiating infections [2,3]. These miniature devices enable disease diagnosis and control testing beyond viruses to bacterial infections and medical emergencies, with point-of-care patch diagnostics replacing ponderous and expensive laboratory testing. Therefore, there is a growing interest in small patches incorporating mass manufacturable polymer MNs [4,5], with the point-of-care rapid diagnosis market alone predicted to grow to $50.6 billion by 2025 [6].

To enable mass manufacturing of MNs, factors such as reproducibility, fabrication precision, lower production cost, and time should be addressed. For instance, manufacturing techniques such as reactive ion etching and deep reactive ion etching incorporate multistage fabrication processes with high production costs [7]. Similarly, laser ablation and lithography techniques are costly, requiring extended production time [8]. To overcome the current manufacturing limitations, MNs might be fabricated cost-effectively, with high precision and accuracy, using 3D printing and TPP techniques [9-11]. Although additive manufacturing (AM) techniques are usually viewed as time-consuming processes, modifications and optimizations of printing parameters within the codes and algorithms of AMs can lead to significant reductions in production time [11].

MN arrays are classified into solid, hollow, coated, hydrogel-forming, and dissolvable types, which depending on the specific medical applications [12,13], are fabricated using silicon, metal, ceramic, silica glass, carbohydrate, and polymers [7,14]. In recent years, polymeric MNs have gained a lot of interest due to their biocompatibility, biodegradability, and potential for mass production [12]. Polymers such as polylactic acid (PLA), poly(methyl methacrylate) (PMMA), poly(carbonate), cyclic olefin copolymer (COC) and cycloolefin polymers (COP), polystyrene, and SU-8 photoresists, have all been used for fabrication of MNs. The low manufacturing cost and desirable mechanical properties of medical-grade thermoplastics such as COPs make them a particularly attractive choice of materials [15,16]. MN thermoplastic replicas are readily fabricated using injection molding or hot embossing [17]. However, process characteristics such as operating temperature, axial force range, and embossing time depend on material properties, geometrical size, and complexity, requiring multiple optimization studies.

MN arrays must be capable of being handled without risk of damage and must penetrate the skin with low force to the required depth [18]. There should be no MN-induced skin contamination, for example, due to breakage of the tips, and zero toxicity demands medical-grade materials. Evaluation of MN mechanical strength requires an investigation of MN insertion characteristics and possible failure scenarios. During the normal insertion of MNs, the applied force is linearly increased to the moment of rupture, which breaks the skin's SC layer, followed by a sudden drop in the force-displacement graph [19,20]. However, the MN can be subjected to sudden excessive axial or lateral loads, which may induce early failure of the MN before skin rupture. Several methods are used to estimate these critical loads and their associated stresses, including theoretical analysis, experimental investigations, and FEA simulations [21]. For example, due to the skin's SC barrier, the normal (vertical) insertion of MN patches on the skin may result in MN failure due to buckling. The skin's irregular topology and inherent elasticity can also impose undesired lateral loads, resulting in transverse bending failure [14]. Prevention of possible failure scenarios can avoid MN breakage and reduce the risk of leaving residues in the skin, hence improving overall insertion safety. For the MN insertion to be mechanically safe, the safety margin (SM), which is the ratio of failure force to insertion force, should be maximized and greater than unity (SM > 1) [22].

MNs must penetrate deep enough into the skin layers to enable an effective therapeutic drug or vaccine delivery and extraction of capillary blood or interstitial fluid while avoiding stimulation of the underlying nerve system, which can cause pain to the patient [21,23]. To facilitate the penetration of the MNs, the axial force applied to the MN must be greater than the resistive force of the skin. Successful insertion is achieved upon reaching sufficient penetration depth and creating microchannels within the skin. However, the skin's inherent elasticity and its irregular surface, with the tendency to fold around MN projections, result in unpredictable array penetration efficiency (APE), defined as the fraction of the MNs in the array passing through the stratum corneum layer without damage [24,25]. Further quantification of MN penetration is the fractional penetration length (FPL), defined as the proportion of a MN's length penetrating the skin relative to its overall length. Meanwhile, several commercial insertion devices are patented and marketed to provide a platform for quick and pain-free insertion of MN patches, mainly for drug delivery; however, they may only be suitable for specific MN designs [26].

During MN insertion tests, the experimental setups for the measurement of FPL and APE affect the fidelity and repeatability of results [21]. To mimic the in vivo conditions of the skin, some

researchers pre-stretch the sample [27,28]. But the uncontrolled initial skin strain may yield different results for otherwise similar experiments. Shu et al. recently indicated the significance of controlled skin strains on both force of insertion and MN penetration [29].

This paper investigates the reliability and fidelity of dense thermoplastic MN arrays (9 × 9) fabricated using TPP and hot embossing techniques. It considers the mechanical integrity and insertion characteristics of the arrays using theoretical, experimental, and simulation approaches. The arrays are coated with fluorescein to simulate transdermal low molecular weight drug delivery. To study MN penetration, the replicated polymer MN arrays were applied on the skin with various application methods, including dynamic impact insertion using a commercial applicator and insertion using an in-house designed and manufactured spring-loaded prototype applicator. A custom skin stretching mechanism was built to mimic skin in vivo conditions in a controlled manner. MN arrays were applied on the full-thickness porcine back skin. Pig skin possesses similarities to human skin [30]; excised dorsal (back) skin has greater stiffness compared to other skin locations [31]. The experimental results include the MN mechanical strength, mechanisms of MN damage, skin insertion force, and margin of safety prediction, along with an estimation of FPL and APE applied using different methods. The study shows the importance of custom-made impact applicators tailored for specific MN arrays to improve the APE and FPL and maintain a higher margin of safety during insertions.

Materials and Methods

Design and fabrication of master MN array

The MN array fabrication process uses the commercial Nanoscribe Photonic Professional GT 3D printer (Nanoscribe GmbH, Karlsruhe, Germany), providing a TPP process to make a master MN array by additive manufacturing. The 9 × 9 MN array with an overall height of 1100 µm, 250 µm base diameter, 500 µm interspacing, and 75 µm base fillet were initially designed in SolidWorks (Dassault Systems SolidWorks Corporation, Concord, NH, USA), then exported to stereolithography (STL) code.

The generated STL code is then imported into the DeScribe (Nanoscribe GmbH, Karlsruhe, Germany) software to adjust settings such as slicing, shell and scaffolding, laser power, and scanning speeds before converting to General Writing Language (GWL) codes. Parameters such as slicing distance of 2 µm, multiple base slide counts of 4 layers, shell and scaffolding filling method, null shear angle (0°), and laser power of 100 mW were selected after process optimization to reduce MN fabrication time and delamination from the substrate. GWL files are then imported to NanoWrite software (Nanoscribe GmbH, Karlsruhe, Germany), which is synced with NanoScribe to initiate the polymerization. The IP-S negative-tone photoresist was drop cast onto an indium tin oxide (ITO) glass substrate prior to starting the printing process. A dip-in laser lithography (DiLL) objective (25× magnification, NA = 0.8) was used for printing, after which the MN array was washed in propylene glycol methyl ether acetate (PGMEA) for 10 minutes, then rinsed in isopropanol (IPA) solution for 3 minutes. The final master MN array was carefully rinsed with deionized water and air-dried (Figure 1a).

Manufacturing PDMS molds and MN replication

The master MNs were subsequently used to make soft polydimethylsiloxane (PDMS) molds for hot embossing the MN arrays in Zeonor 1060R COP. The PDMS solution was made by degassing the mixture of 1:10 curing agent/base ratio, which was then poured onto the master MN array and heated at 80 °C for 1 hour (Figure 1b). Samples were kept overnight to cure the PDMS mixture (Figure 1c).

To perform the hot embossing process, a rheometer (TA Instruments, New Castle, USA) was used to melt the Zeonor 1060R COP crystals, and placed in the cavities of the PDMS mold, while press forcing the sample against the mold. During this process, Zeonor 1060R crystals are placed on the PDMS mold cavities (Figure 1d), with the chamber temperature raised to 160 °C, which is 60 °C above the Zeonor 1060R's glass transition temperature (100 °C). The rheometer is equipped with an enclosable chamber to maintain a constant temperature during the process. To perform the embossing process, the upper plate displacement and the lowering speed were set to decrease overtime to overcome the effects of viscosity that can impose abrupt pressure on the mold cavities (Figure 1e). The upper disk was lowered by ≈1.5 mm (Figure 1g) at a speed which was non-linearly reduced from ≈50 to 5 µm/min ensuring that the maximum axial force did not exceed 30 ± 2 N (Figure 1h). After embossing, the chamber temperature was set to 10 °C for 15 minutes to cool down the PDMS and thermoplastic sample and solidify the replicated microstructure. The polymeric replica of the MN array was then carefully peeled off from the PDMS mold (Figure 1f). The entire replication process for each MN array took 45 minutes.

MN mechanical compression test

To study the failure modes of the MN arrays, a quasi-static compression test was conducted using the rheometer. A single MN with similar geometry to the 9 × 9 MN array was separately manufactured using the same process. It was assumed that the single MN projection linearly represents the 9 × 9 MN

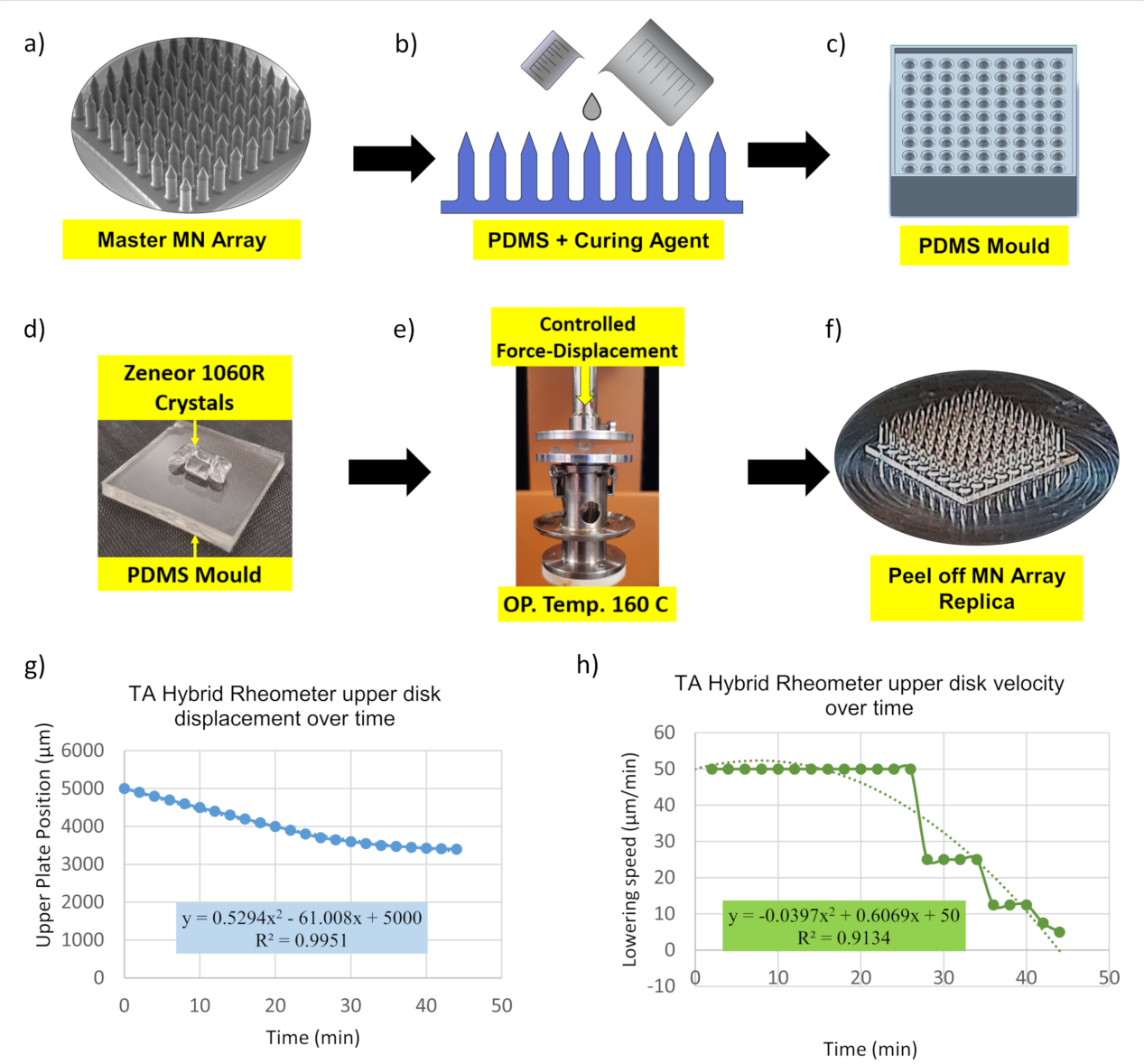


Figure 1: Laboratory scale process for hot embossing of COP MN array replicas using a rheometer. a) Master MN arrays fabricated using TPP technique, b) PDMS mixture solution is poured on the master mold then cured at 80 °C inside the oven, c) PDMS mold is made once master MN arrays are peeled off, d) Zeonor 1060R pellets are placed on the PDMS mold, e) hot embossing is conducted by lowering the upper disk in a controlled manner at a chamber temperature of 160 °C, f) COP thermoplastic MN array is peeled from the PDMS mold, g) the rheometer's upper disk displacement versus time, and h) the rheometer's upper disk speed overtime during the molding process.

array by the factor of the number of MN projections. The single MN was attached to the lower disk of the rheometer using a double-sided tape. The upper disk was lowered with a constant velocity of 1 µm/s and traveled for 400 µm, measured from the MN tip. During the compression test, the force-displacement data were collected and plotted with MATLAB (Natick, Massachusetts, USA).

Skin preparation and MN array insertion tests

Porcine back skin was used to test the penetration efficiency and insertion depth of the 9 × 9 MN arrays, using experimental procedures approved by the University of Southern Queensland (USQ) and the University of Queensland (UQ) animal ethics and biosafety committees. The skins were shaved to remove the excess hairs and kept frozen at −20 °C on a flat aluminum surface, then sectioned using a surgical knife to remove the fat layer to the thickness of 3 ± 0.1 mm [31], and thawed before insertion testing on a 3D printed stretching mechanism to mimic skin in vivo conditions (Figure 2a). The MN arrays were initially oxygen plasma cleaned for 1 minute before dip coating with a concentrated aqueous solution of fluorescein (Sigma-Aldrich Corp., St. Louis, MO, USA). Subsequently, the MN

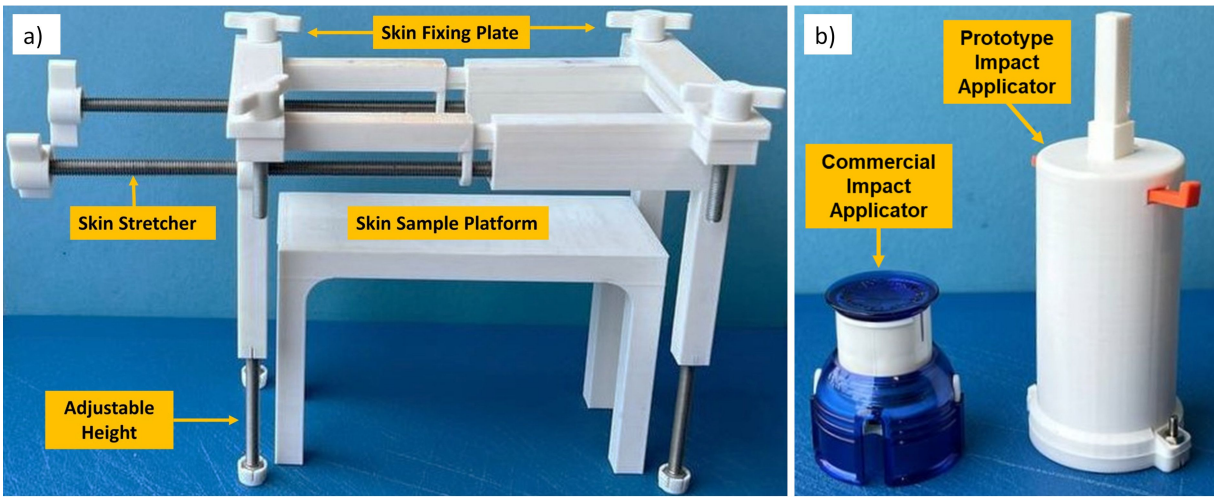


Figure 2: a) Skin stretching mechanism used to mimic skin condition in vivo. The skin sample is placed on the skin sample platform. Then, the stretching mechanism's height is adjusted. Skin is then secured at both ends by fixing plates before stretching by the stretcher screws. b) A commercial applicator with a single impact speed and a prototype custom-made impact applicator capable of insertion with different impact speeds was used to apply MN arrays dynamically onto the porcine skin subjects.

arrays were fixed onto a commercial spring-loaded applicator (Medtronic MiniMed Quick-Serter), providing an insertion velocity of 0.5 m/s. The tests were repeated using a custom-made prototype applicator, providing an insertion velocity of 1.5–4.5 m/s (Figure 2b). MN arrays were attached to the applicators' plungers with double-sided tape and applied to the skin. The skin samples were then tape-stripped to remove the SC layer of skin before imaging.

Stereomicroscopy was then performed using a Nikon SMZ-18 microscope to determine the APE on skin subjects. The skin samples were fixed in optimal cutting temperature (OCT) compound, then sectioned to 50 µm thick slices using Leica CM3050 cryostat (Wetzlar, Germany) and placed on Superfrost glass slides. The sectioned samples were then imaged by a Zeiss LSM 710 Meta NLO confocal laser scanning microscope (Carl Zeiss, Jena, Germany) to visualize the penetration depth and estimate the FPL for individual MN projections. The images were further analyzed using ImageJ software (U. S. National Institutes of Health, Bethesda, Maryland, USA).

Measuring the force of insertion

Skin insertion tests were designed to measure the insertion force during the experiments. To facilitate the force recordings during MN insertions on porcine skin, BD Ultra-Fine™ 4 mm Pen Needles were used (Franklin Lakes, New Jersey, USA), having similar geometry to the fabricated MN array projections described above. The main reason for using PEN needles was their greater length (4 mm) which prevents early attachment of skin to the base plate, which is a common phenomenon when testing the MNs. The force of insertion is directly proportional to the square of the MN base diameter (Equation 1). Compared to other MN geometrical parameters, the dependence on the interfacial area was previously reported by Park et al. for an insertion test of polymeric MNs on human cadaver skin [22]. The representative PEN needle had a diameter of 230 µm and tip size of 2.5 µm (Figure 3a). This is similar to polymeric MNs made from Zeonor 1060R with a base diameter of 245 µm and tip size of 1.6 µm (Figure 3b). The Ultra-Fine PENs were attached to the upper disk of the rheometer using double-sided tape. The porcine back skin is fixed on the custom-made 3D printed skin stretching mechanism described above (Figure 2a) and subsequently pre-stretched to mimic the skin in vivo conditions [27]. The upper plate was lowered at 0.1 mm/s speed towards the skin while recording the force versus displacement data.

FEA of MN insertion into the skin

To determine the MN and skin interactions during the penetration, a 2D axisymmetric simulation model was performed using ANSYS (2020 R1, ANSYS, Canonsburg, Pennsylvania, USA) Explicit Dynamics. The skin was assumed to be comprised of three layers (1) stratum corneum, (2) dermis, and (3) hypodermis with 26 µm, 2 mm, and 1.1 mm thicknesses, respectively. An Ogden (first-order) model [32] was introduced for the dermis layer, while SC and hypodermis layers were considered to possess a linear elastic mechanical response. Quadrilateral meshing with a bias factor of 5 was used to increase the number of elements in the vicinity of the skin piercing zone. Moreover, the sphere of influence meshing algorithm was used to create fine elements at the tip of the MNs.

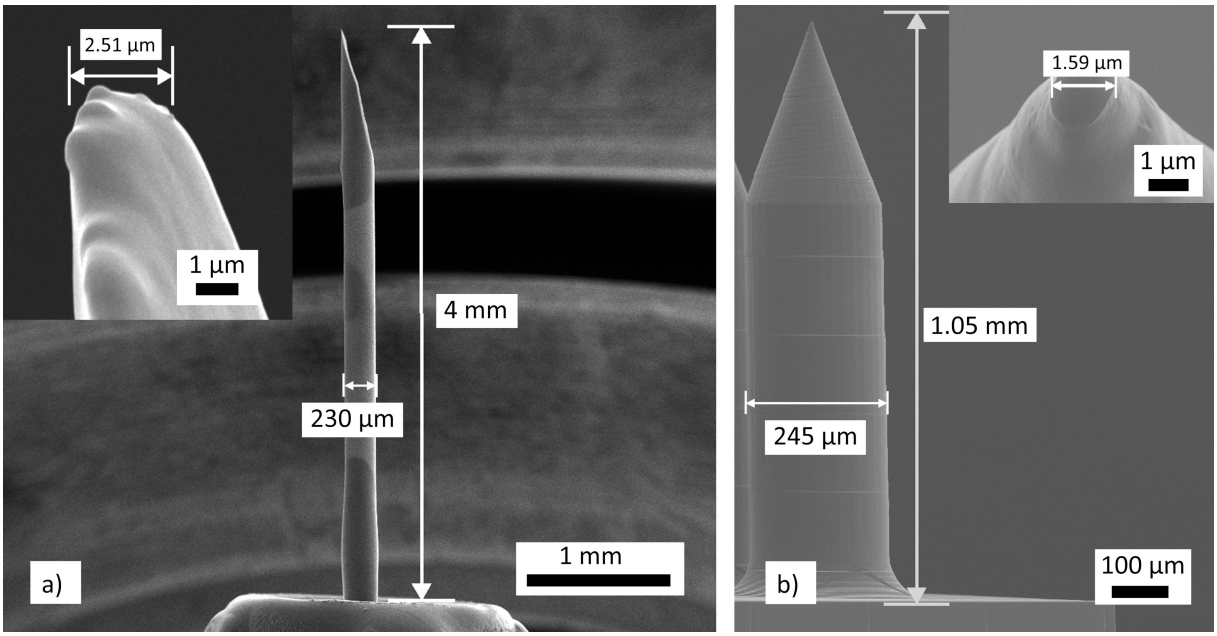


Figure 3: SEM images of length, tip size, and diameter of the a) BD Ultra-Fine™ 4 mm Pen Needle and b) thermoplastic Zeonor 1060R replicas.

The coefficient of friction between the contact surfaces was set to 0.42 [29]. Upon MN penetration, with a constant impact speed of 4.5 m/s, the force-displacement data were recorded to estimate the insertion force. To enable the skin piercing model, an erosion algorithm was used to eliminate the elements that reached their failure stress. To optimize the run time, the automatic mass scaling method was activated with a minimum Courant–Friedrichs–Lewy (CFL) time step of 1 picosecond [33]. The mass scale algorithm artificially increases the elemental density, which in turn reduces the overall time step by increasing the time required for a sound wave to traverse the smallest elements. Table 1 summarizes the material properties used for the individual components in the insertion simulation.

Results and Discussions

Design and fabrication of MN array master and replica

The 9 × 9 MN arrays were successfully fabricated by TPP, and Zeonor 1060R replicas were made (>20 cycles) using hot embossing on PDMS mold. During the cycles, no damage was observed to the PMDS mold or its microcavities. Three 9 × 9 MN patch replicas were selected from different replication cycles of equal intervals (cycles: 1, 15, and 30). Nine projections per MN patch (n = 27) were selected and measured against MN master length and base diameter. The overall average length and base diameter were 1045.04 ± 3.83 µm and

Table 1: Mechanical properties of different skin layers used in ANSYS Explicit Dynamics simulation.

Parameter	Microneedle	SC	Dermis	Hypodermis
mathematical model	linear elastic	linear elastic	hyperelastic: Ogden 1st order with uniaxial test data	linear elastic
thickness (mm)	n.a.	0.026	2	1.1
Young Modulus (MPa)	2100	67	n.a.	0.1
Poisson ratio	0.48	0.49	0.49	0.48
density (kg/m^3)	1.01 E−6	1.3 E−6	1.2 E−6	9.71 E−7
hyperelastic coefficients MU1, A1 (MPa)	n.a.	n.a.	0.0568, 13.3	n.a.
incompressibility factor (1/MPa)	n.a.	n.a.	0.0745	n.a.
failure criteria (MPa)	n.a.	20	7	n.a.
Ref.	[9]	[29,30,34]	[29,35]	[29,34]

255.37 ± 2.39 µm (mean ± standard deviation), respectively. The results recorded for the cycles 1, 15, and 30 indicated the respective average projection's axial shrinkages of 4.72 ± 0.15%, 5.37 ± 0.27%, 4.9 ± 0.21% (mean ± standard deviation) (ANOVA, $p < 0.001$). Measurement for base diameters indicated enlargements of 3.22 ± 0.21%, 2.02 ± 0.33%, 1.07 ± 0.2% (mean ± standard deviation) (ANOVA, $p < 0.001$), respectively. The base diameter enlargements indicated excessive lateral forces on the cavity walls compared to longitudinal force along the axis. Figure 4a shows the SEM images of the MN array resin master, and Figure 4b,c shows the Zeonor 1060R replicas after the hot embossing, indicating slight shrinkages in both height and diameter after replication; the occurrence of small shrinkage has been reported for these thermoplastic COP materials before [9]. Thus, the effect of shrinkage needs to be considered within the initial design to ensure the dimensional accuracy of final MN replicas.

Analytical and experimental characteristics of MN failures by mechanical compression test

Bending, buckling, and fracture are the main possible failure risks of polymer MN arrays upon insertion into the skin. Thus, investigations on the MN failure scenarios are essential and can be performed using experimental and analytical approaches. For a MN array of N projections to puncture the skin with the application of a vertical force F, the tip radius of the MNs must be small enough to exceed the puncture stress σ_p. Assuming an approximately hemispherical tip, the condition on the tip radius for an array of N MNs applied with a force F is:

$$r_t \leq \sqrt{\frac{F}{2\pi\sigma_p N}} . \quad (1)$$

For a particular application force (F), the maximum tip radius r_t can be approximated based on the skin's ultimate stress before puncture (σ_p).

During actual insertions, MNs are not always inserted in an exactly vertical fashion which results in lateral shear loads. This horizontal shear force component (f_h) that is perpendicular to the axis of each MN may cause fracture at an approximate distance x from the base where the yield stress σ_y of the material is exceeded. Therefore, for MNs having a cylindrical shaft of radius a, with yield stress σ_y the fracture location from the base can be estimated as [36]:

$$x = \frac{\pi a^3 \sigma_y}{4 f_h} . \quad (2)$$

If bending is avoided and true vertical insertion is achieved, failure may be due to buckling when the vertical force on each MN reaches the critical value (f_B) [37]:

$$f_B = \frac{\pi^3 a^4 E}{16 L^2} , \quad (3)$$

where L is the MN length, a is the MN radius, and E is the elastic modulus. Buckling failure load f_B is the most important figure of merit used to determine the margin of safety of MNs.

Figure 5a shows the results of mechanical quasi-static compression tests for the single replicated MN. The results revealed both near-tip yield stress failure, presumed due to the horizontal shear stress forces, and buckling failure, which occurred

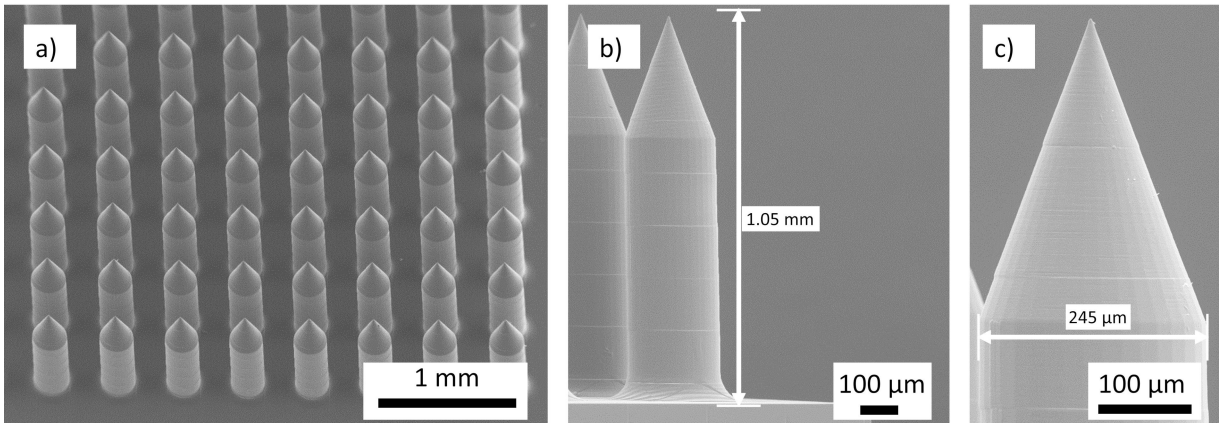


Figure 4: SEM of the 9 × 9 MN array, a) master MN array fabricated by TPP, b) replicated thermoplastic MN array with 1.05 mm height, and c) replicated thermoplastic MN array with a diameter of 245 µm.

at the axial applied force of 1.29 N. Figure 5b illustrates the experimental force-displacement diagram for the theoretical prediction of the moment of critical buckling load. The peak on the graph indicated the MN failure. However, due to the viscoelastic nature of Zeonor 1060R, the initial near-tip failure was indistinct on the force-displacement diagram. These mechanical responses have been previously observed during compression tests on polymeric MN materials, including carboxymethyl cellulose (CMC) and polylactic acid (PLA) [1,38]. This unique viscoelastic behavior prevents the MN tip fracture, which can leave residuals in the skin. As indicated in Figure 5a, the bending location (x) and magnitude of buckling load are in alignment with Equation 2 and Equation 3. The exact location is dependent on the base diameter (125 µm), Zeonor 1060R yield stress (53 MPa), and lateral shear force component estimated during insertion. According to SEM images from samples (n = 3), the location of bending from the base (x) is at 244.4 ± 2.03 µm corresponding to a lateral shear load of 0.33 to 0.34 N. Buckling modeling was based on elastic modulus (2100 MPa) and effective penetrative length (1.025 mm) using Equation 3 and compared with experimental data. This critical buckling load was predicted to occur at 0.95 N, based on theory, whereas the experimental value was 1.29 N during compression tests. The higher value found in experimental results compared to buckling theory (Equation 3) is due to the reinforcing effects of the fillets at the MN base that improved MN stability toward sudden bending [9]. The thermoplastic Zeonor 1060R MNs had a higher failure force when compared to failure forces (0.1–0.22 N) of polylactic-*co*-glycolic acid (PLGA) MNs with a similar base diameter (200 µm) and lengths (700–1500 µm) [22].

Simulation and experimental investigation on MN insertion force

To investigate the insertion force and failure modes of MN arrays into the skin, the insertion of a single MN was simulated using FEA software. Figure 6a illustrates the axisymmetric model incorporating a three-layer skin model with the relevant boundary conditions. For mesh generation, the inclusion of quadrilateral elements for skin layers with a bias factor of 5 and the sphere of influence technique for MN tip yielded more accurate results due to finer meshing at the regions of MN–skin interactions. The results from the simulation showed that maximum von-Mises stress in the skin layers reached 18.9 MPa on the SC layer near the MN insertion, which is in line with the predefined failure criteria for SC and dermis layers (Figure 6b). Force displacement data were recorded and plotted during the MN insertion. The graph represented a linear increase that peaked at 0.18 N before a sudden drop due to skin fracture at the SC layer (Figure 6c).

The results were coupled with a representative in vitro experimental model using BD Ultra-Fine™ 4 mm Pen Needles. In this test, the force was linearly increased to a peak value of 0.26 N before penetrating the skin, followed by an abrupt drop in the recorded force. The ratio of buckling failure force to the insertion force was calculated using the simulation method, showing a SM of 7.16. For in vitro insertion by BD Ultra-Fine™ 4 mm Pen Needles, the SM was calculated as 4.95 (Figure 6d). The SM for both methods was above 1, indicating a sufficient safety level for skin insertions. However, SM directly depends on the MN material, its base diameter and the fillet, overall length, and the mechanics of skin subjects.

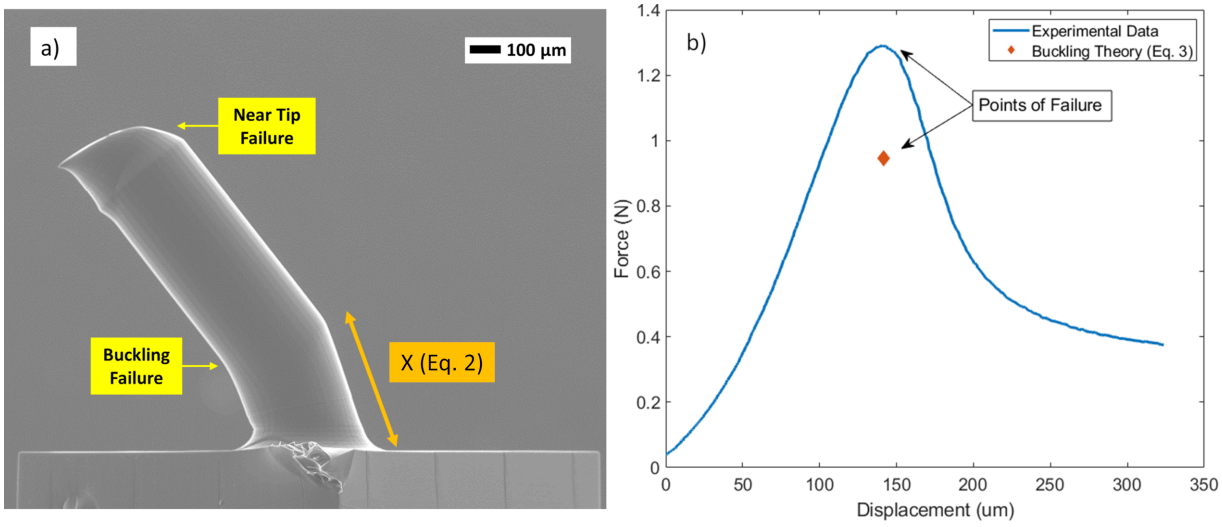


Figure 5: a) SEM of a MN after compression test, showing effects due to buckling and near tip failure indicating non-vertical shearing forces, b) force-displacement data for a single MN indicating a failure point of 1.26 N validated by buckling theory.

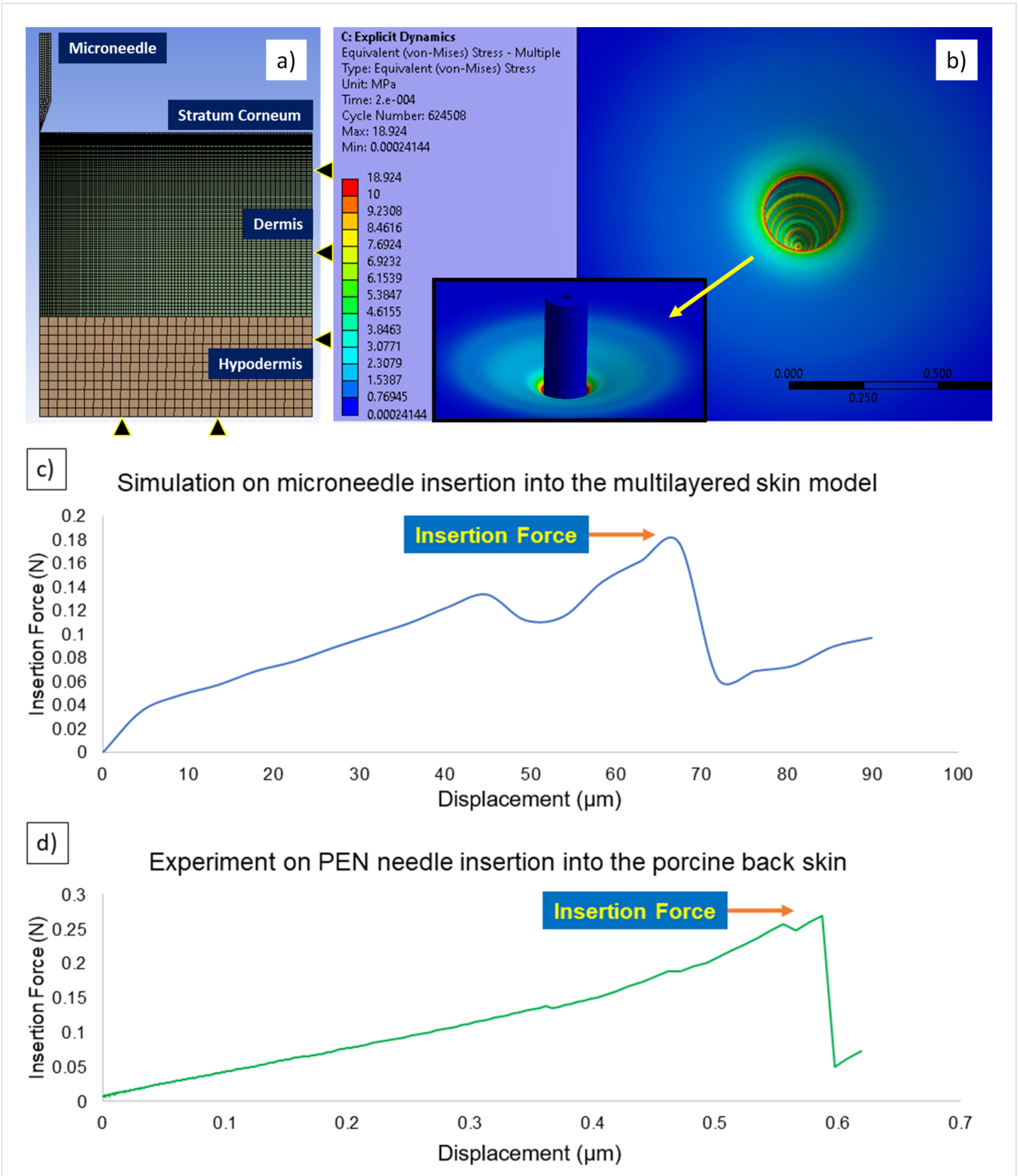


Figure 6: a) 2D axisymmetric meshing for three-layer skin model and single MN model, b) von-Mises stress result of the penetration region and the associated skin deflection surrounding the MN insertion. Force-displacement graph recorded during insertion based on c) FEA Explicit Dynamics simulation, and d) in vitro experiment using a BD Ultra-Fine™ 4 mm Pen Needle on porcine skin.

Penetration and delivery of fluorescein into skin

For MN array insertion tests on porcine skin, confocal and stereo microscopes were used to estimate the FPL and APE penetration metrics. Figure 7a–d shows confocal microscopy results of skin insertion tests for various insertion methods: (a) control, (b) using a commercial applicator, (c) using the prototype applicator at impact velocity of 3 m/s, and d) again at

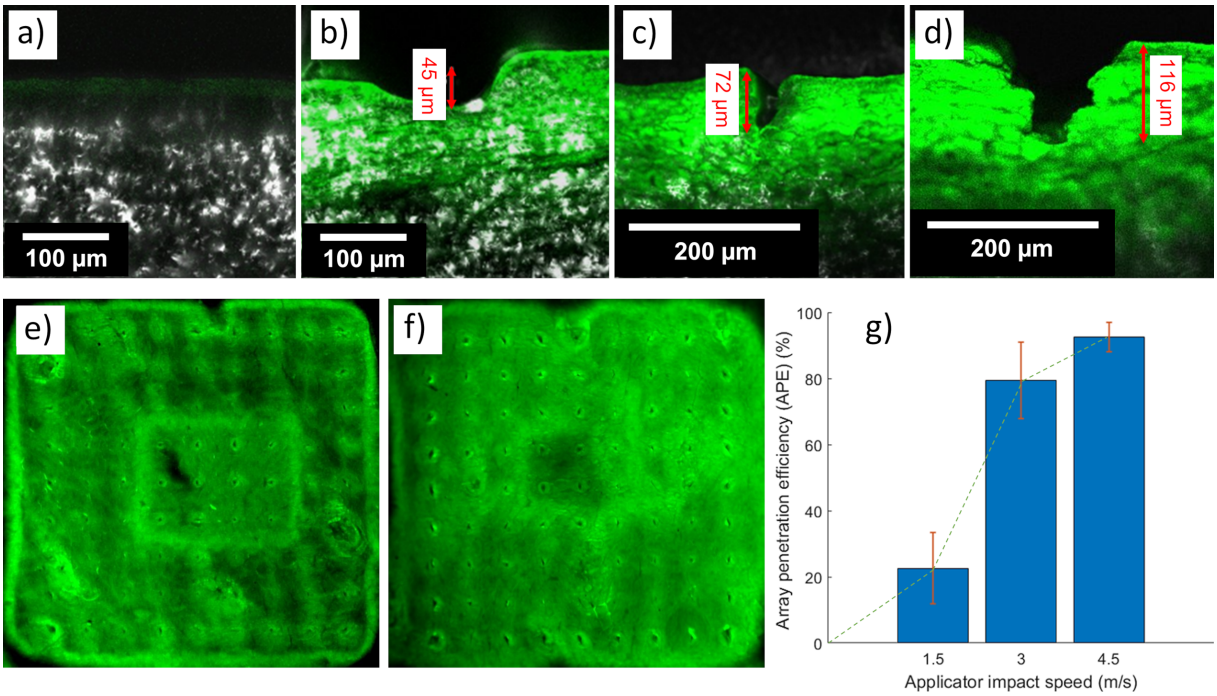


Figure 7: Confocal images of cryo-sectioned porcine back skin showing MN array penetration: a) control test without MNs or fluorescein solution, b) MN array patch on the skin showing no penetration using the commercial applicator, c) MN penetration and fluorescein diffusion into the skin, using the custom-made impact applicator at 3 m/s impact velocity, d) as c) for 4.5 m/s impact velocity. Stereomicroscopy images for the estimation of APE using the custom-made applicator with e) impact velocity of 3 m/s, and f) impact velocity of 4.5 m/s. g) Graph representation of the effects of the prototype applicator on APE (n = 3) for different impact speeds.

4.5 m/s impact velocity. Figure 7a shows the control results where no MN array was inserted into the skin. Figure 7b indicates a skin deflection of 45 µm using the commercial applicator with 0.5 m/s impact speed revealing no penetration through the SC. In contrast, the custom applicator produced penetration of 72 µm and 116 µm (FPL of 7% and 11%) for impact velocities of 3 m/s and 4.5 m/s (Figure 6c,d). For comparison, the insertion tests of Meliga et al. on mouse ear skin produced penetration of ≈20 µm to 60 µm when their application speed increased from ≈0.25 m/s to 2 m/s [33]. In our experiments, for both applicators, insertion performance depends not only on impact velocity, but also on the number of MNs, MN interspacing, MN base diameter, and skin type, though, in this work, only impact velocity was varied. Our previous results showed that the same commercial applicator with an insertion velocity of 0.5 m/s successfully inserted a 4 × 4 thermoplastic MN patch (height: 700 µm, base diameter: 150 µm) into rabbit ear skin without deformation of the MN patch [9].

After initial penetration, APE was measured from stereomicroscopy of the diffused fluorescein patterns. There was a total failure to deliver fluorescein into the skin using the commercial applicator. In contrast, fluorescein delivery to the skin using the prototype applicator revealed APE from 22.63 ± 10.78% through 79.42 ± 11.47% to 92.52 ± 4.45% (mean ± standard deviation, n = 3 for each test) when the impact velocity was increased from 1.5, through 3, to 4.5 m/s (Figure 7e,f). Figure 7g shows the APE effects in bar chart form. The results show an increase of 56.79% in APE on increasing impact velocity from 1.5 to 3 m/s and an increase of 13.17% for an impact velocity increase from 3 to 4.5 m/s.

It is worth noting that Crichton et al. [39] studied the effect of varying skin strain rates on MN insertion into a rabbit's ear. At low strain rates (≈0, 0.56, and 1.22 m/s), the APE for their Nanopatch^{TM} was as low as 25%; however, by increasing the strain rate to 5,300 s^{-1}, at an insertion velocity of 1.96 m/s, an APE value of ≈95% was achieved.

The work summarized here demonstrates the potential of high-fidelity and low-cost thermoplastic MN arrays for coated drug delivery. In addition, thermoplastic MN arrays have the potential for collecting interstitial fluid more safely than using glass [40] or silicon MNs.

Conclusion

MN arrays have considerable potential for cost-effective, rapid, and non-invasive therapeutic drug delivery, vaccination, and

point-of-care diagnostics, with potential for self-administration. While large-scale manufacturing of MN arrays with high accuracy remains a challenge, the emerging technique of TPP coupled with hot embossing provides a promising, cost-effective, and highly precise method to produce batches of polymer MNs with the potential for mass production. This study fabricated Zeonor 1060R polymer MN arrays from PDMS secondary molds using a controlled hot embossing process with only minor shrinkage of the thermoplastic protrusions. The hot embossing process, tailored for current MN geometrical complexity and size, was described, including embossing time and compression speed. Key parameters were optimized to minimize the polymerization time and enhance the structural integrity during the TPP process.

A series of experiments was performed to characterize the mechanical failure and insertion characteristics of MNs: (1) axial compression test, (2) controlled insertion of BD Ultra-Fine™ 4 mm Pen Needle on porcine back skin, along with (3) Explicit Dynamics simulation of single MN insertion on a three-layered skin model. The comparisons between the results found for insertion force and quasi-static buckling test showed sufficient margins of safety (SM ≫ 1), indicating the potential of Zeonor 1060R MNs for applications in drug delivery and vaccination, with minimal associated risks. The insertion test setups for current research introduced a mechanism to enable controlled skin stretching to mimic in vivo conditions. Experiments also showed that the commercial applicator was less effective than our customized impact insertion applicator, demonstrating the need to design and manufacture customized applicators tailored for specific MN array designs.

Acknowledgements

This work was performed in part at the Queensland node of the Australian National Fabrication Facility, a company established under the National Collaborative Research Infrastructure Strategy to provide nano and microfabrication facilities for Australia's researchers. This research was undertaken with the assistance of resources provided at the University of Southern Queensland.

ORCID® iDs

Zahra Faraji Rad - https://orcid.org/0000-0001-6528-5965

References

1. Lee, J. W.; Park, J.-H.; Prausnitz, M. R. *Biomaterials* **2008,** *29,* 2113–2124. doi:10.1016/j.biomaterials.2007.12.048
2. Uddin, M. J.; Scoutaris, N.; Economidou, S. N.; Giraud, C.; Chowdhry, B. Z.; Donnelly, R. F.; Douroumis, D. *Mater. Sci. Eng., C* **2020,** *107,* 110248. doi:10.1016/j.msec.2019.110248
3. Bariya, S. H.; Gohel, M. C.; Mehta, T. A.; Sharma, O. P. *J. Pharm. Pharmacol. (Chichester, U. K.)* **2011,** *64,* 11–29. doi:10.1111/j.2042-7158.2011.01369.x
4. Faraji Rad, Z. Microneedles Fabrication for Subcutaneous Fluid Sampling and Drug Delivery. Ph.D. Thesis, University of Birmingham, Birmingham, UK, 2016. http://etheses.bham.ac.uk/id/eprint/6734/
5. Ventrelli, L.; Marsilio Strambini, L.; Barillaro, G. *Adv. Healthcare Mater.* **2015,** *4,* 2606–2640. doi:10.1002/adhm.201500450
6. Vashist, S. K. *Biosensors* **2017,** *7,* 62. doi:10.3390/bios7040062
7. Jung, J. H.; Jin, S. G. *J. Pharm. Invest.* **2021,** *51,* 503–517. doi:10.1007/s40005-021-00512-4
8. Aldawood, F. K.; Andar, A.; Desai, S. *Polymers (Basel, Switz.)* **2021,** *13,* 2815. doi:10.3390/polym13162815
9. Faraji Rad, Z.; Nordon, R. E.; Anthony, C. J.; Bilston, L.; Prewett, P. D.; Arns, J.-Y.; Arns, C. H.; Zhang, L.; Davies, G. J. *Microsyst. Nanoeng.* **2017,** *3,* 17034. doi:10.1038/micronano.2017.34
10. Faraji Rad, Z.; Prewett, P. D.; Davies, G. J. *Microsyst. Nanoeng.* **2021,** *7,* 71. doi:10.1038/s41378-021-00298-3
11. Johnson, A. R.; Procopio, A. T. *3D Print. Med.* **2019,** *5,* 2. doi:10.1186/s41205-019-0039-x
12. Faraji Rad, Z.; Prewett, P. D.; Davies, G. J. *Beilstein J. Nanotechnol.* **2021,** *12,* 1034–1046. doi:10.3762/bjnano.12.77
13. Waghule, T.; Singhvi, G.; Dubey, S. K.; Pandey, M. M.; Gupta, G.; Singh, M.; Dua, K. *Biomed. Pharmacother.* **2019,** *109,* 1249–1258. doi:10.1016/j.biopha.2018.10.078
14. Larrañeta, E.; Lutton, R. E. M.; Woolfson, A. D.; Donnelly, R. F. *Mater. Sci. Eng., R* **2016,** *104,* 1–32. doi:10.1016/j.mser.2016.03.001
15. Faraji Rad, Z.; Nordon, R. E.; Davies, G. J.; Anthony, C. J.; Prewett, P. D. Microfluidic devices and fabrication. U.S. Patent US10850082B2, Dec 1, 2020.
16. Faraji Rad, Z.; Prewett, P. D.; Davies, G. J. *Manuf. Lett.* **2021,** *30,* 39–43. doi:10.1016/j.mfglet.2021.10.007
17. Juster, H.; van der Aar, B.; de Brouwer, H. *Polym. Eng. Sci.* **2019,** *59,* 877–890. doi:10.1002/pen.25078
18. Davis, S. P.; Landis, B. J.; Adams, Z. H.; Allen, M. G.; Prausnitz, M. R. *J. Biomech.* **2004,** *37,* 1155–1163. doi:10.1016/j.jbiomech.2003.12.010
19. Khanna, P.; Luongo, K.; Strom, J. A.; Bhansali, S. *J. Micromech. Microeng.* **2010,** *20,* 045011. doi:10.1088/0960-1317/20/4/045011
20. Ranamukhaarachchi, S. A.; Stoeber, B. *Biomed. Microdevices* **2019,** *21,* 100. doi:10.1007/s10544-019-0449-y
21. Ebrahiminejad, V.; Prewett, P. D.; Davies, G. J.; Faraji Rad, Z. *Adv. Mater. Interfaces* **2022,** *9,* 2101856. doi:10.1002/admi.202101856
22. Park, J.-H.; Allen, M. G.; Prausnitz, M. R. *J. Controlled Release* **2005,** *104,* 51–66. doi:10.1016/j.jconrel.2005.02.002
23. Ma, G.; Wu, C. *J. Controlled Release* **2017,** *251,* 11–23. doi:10.1016/j.jconrel.2017.02.011
24. Badran, M. M.; Kuntsche, J.; Fahr, A. *Eur. J. Pharm. Sci.* **2009,** *36,* 511–523. doi:10.1016/j.ejps.2008.12.008
25. Donnelly, R. F.; Garland, M. J.; Morrow, D. I. J.; Migalska, K.; Singh, T. R. R.; Majithiya, R.; Woolfson, A. D. *J. Controlled Release* **2010,** *147,* 333–341. doi:10.1016/j.jconrel.2010.08.008
26. Singh, T. R. R.; Dunne, N. J.; Cunningham, E.; Donnelly, R. F. *Recent Pat. Drug Delivery Formulation* **2011,** *5,* 11–23. doi:10.2174/187221111794109484
27. Olatunji, O.; Das, D. B.; Garland, M. J.; Belaid, L.; Donnelly, R. F. *J. Pharm. Sci.* **2013,** *102,* 1209–1221. doi:10.1002/jps.23439

28. Xenikakis, I.; Tzimtzimis, M.; Tsongas, K.; Andreadis, D.; Demiri, E.; Tzetzis, D.; Fatouros, D. G. *Eur. J. Pharm. Sci.* **2019,** *137,* 104976. doi:10.1016/j.ejps.2019.104976
29. Shu, W.; Heimark, H.; Bertollo, N.; Tobin, D. J.; O'Cearbhaill, E. D.; Annaidh, A. N. *Acta Biomater.* **2021,** *135,* 403–413. doi:10.1016/j.actbio.2021.08.045
30. Ranamukhaarachchi, S. A.; Lehnert, S.; Ranamukhaarachchi, S. L.; Sprenger, L.; Schneider, T.; Mansoor, I.; Rai, K.; Häfeli, U. O.; Stoeber, B. *Sci. Rep.* **2016,** *6,* 32074. doi:10.1038/srep32074
31. Pramudita, J. A.; Shimizu, Y.; Tanabe, Y.; Ito, M.; Watanabe, R. *J. Jpn. Soc. Exp. Mech.* **2014,** *14,* s245–s250. doi:10.11395/jjsem.14.s245
32. Shergold, O. A.; Fleck, N. A.; Radford, D. *Int. J. Impact Eng.* **2006,** *32,* 1384–1402. doi:10.1016/j.ijimpeng.2004.11.010
33. Meliga, S. C.; Coffey, J. W.; Crichton, M. L.; Flaim, C.; Veidt, M.; Kendall, M. A. F. *Acta Biomater.* **2017,** *48,* 341–356. doi:10.1016/j.actbio.2016.10.021
34. Levi, K.; Weber, R. J.; Do, J. Q.; Dauskardt, R. H. *Int. J. Cosmet. Sci.* **2010,** *32,* 276–293. doi:10.1111/j.1468-2494.2009.00557.x
35. Silver, F. H.; Seehra, G. P.; Freeman, J. W.; DeVore, D. *J. Appl. Polym. Sci.* **2002,** *86,* 1978–1985. doi:10.1002/app.11119
36. Beer, F. P.; Johnston, E. R., Jr.; DeWolf, J. T.; Mazurek, D. F. *Mechanics of Materials;* McGraw Hill: New York, NY, USA, 2015.
37. Gittard, S. D.; Chen, B.; Xu, H.; Ovsianikov, A.; Chichkov, B. N.; Monteiro-Riviere, N. A.; Narayan, R. J. *J. Adhes. Sci. Technol.* **2013,** *27,* 227–243. doi:10.1080/01694243.2012.705101
38. Kim, S.; Yang, H.; Eum, J.; Ma, Y.; Fakhraei Lahiji, S.; Jung, H. *Biomaterials* **2020,** *232,* 119733. doi:10.1016/j.biomaterials.2019.119733
39. Crichton, M. L.; Ansaldo, A.; Chen, X.; Prow, T. W.; Fernando, G. J. P.; Kendall, M. A. F. *Biomaterials* **2010,** *31,* 4562–4572. doi:10.1016/j.biomaterials.2010.02.022
40. Wang, P. M.; Cornwell, M.; Prausnitz, M. R. *Diabetes Technol. Ther.* **2005,** *7,* 131–141. doi:10.1089/dia.2005.7.131

License and Terms

This is an open access article licensed under the terms of the Beilstein-Institut Open Access License Agreement (https://www.beilstein-journals.org/bjnano/terms), which is identical to the Creative Commons Attribution 4.0 International License (https://creativecommons.org/licenses/by/4.0). The reuse of material under this license requires that the author(s), source and license are credited. Third-party material in this article could be subject to other licenses (typically indicated in the credit line), and in this case, users are required to obtain permission from the license holder to reuse the material.

The definitive version of this article is the electronic one which can be found at:
https://doi.org/10.3762/bjnano.13.55

BEILSTEIN JOURNAL OF NANOTECHNOLOGY

Microneedle-based ocular drug delivery systems – recent advances and challenges

Piotr Gadziński[1], Anna Froelich[1], Monika Wojtyłko[1], Antoni Białek[2], Julia Krysztofiak[2] and Tomasz Osmałek[*1]

Review

Open Access

Address:
[1]Chair and Department of Pharmaceutical Technology, Poznan University of Medical Sciences and [2]Student Research Group of Pharmaceutical Technology, Poznan University of Medical Sciences

Email:
Tomasz Osmałek[*] - tosmalek@ump.edu.pl

* Corresponding author

Keywords:
eye; microneedles; ocular drug delivery; ophthalmic drugs

Beilstein J. Nanotechnol. **2022,** *13,* 1167–1184.
https://doi.org/10.3762/bjnano.13.98

Received: 30 April 2022
Accepted: 28 September 2022
Published: 24 October 2022

This article is part of the thematic issue "Microneedles for vaccination and drug delivery".

Guest Editor: P. D. Prewett

© 2022 Gadziński et al.; licensee Beilstein-Institut.
License and terms: see end of document.

Abstract

Eye diseases and injuries constitute a significant clinical problem worldwide. Safe and effective delivery of drugs to the eye is challenging mostly due to the presence of ocular barriers and clearance mechanisms. In everyday practice, the traditional eye drops, gels and ointments are most often used. Unfortunately, they are usually not well tolerated by patients due to the need for frequent use as well as the discomfort during application. Therefore, novel drug delivery systems with improved biopharmaceutical properties are a subject of ongoing scientific investigations. Due to the developments in microtechnology, in recent years, there has been a remarkable advance in the development of microneedle-based systems as an alternative, non-invasive form for administering drugs to the eye. This review summarizes the latest achievements in the field of obtaining microneedle ocular patches. In the manuscript, the most important manufacturing technologies, microneedle classification, and the research studies related to ophthalmic application of microneedles are presented. Finally, the most important advantages and drawbacks, as well as potential challenges related to the unique anatomy and physiology of the eye are summarized and discussed.

Review

1 Introduction

Since its first appearance in biomedicine, microtechnology is rapidly entering the world of pharmaceutical sciences, including pharmaceutical technology [1-4]. Due to the impressive evolution of new manufacturing techniques, it offers completely new opportunities to develop very sophisticated and precise drug delivery tools [5,6]. A large number of concepts and implemented projects, which is reflected in a large number of scientific papers, consistently pushes pharmaceutical technolo-

gy to a new level of coping with various diseases, including those related to the eye [7-10].

Eye diseases and injuries are a major clinical problem worldwide, causing severe visual impairment or blindness in many millions of people [11-13]. According to World Health Organization, at least 2.2 billion people suffer from near or distance vision problems [14]. The most common factors that contribute to more or less severe vision loss include unaddressed refractive error, inflammation of the cornea, sclera and iris, conjunctivitis [15], dry eye syndrome [16], allergies [17], retinopathy [18,19], age-related macular degeneration [20], cataract [21], glaucoma [22], central retinal vein occlusion [23], and diabetic macular edema [24,25]. Depending on the prompt diagnosis and treatment, most of them can be completely or partially healed, but in the case of inappropriate or late therapy, irreversible changes may occur [26]. It is also worth mentioning the very high global annual costs of therapies reaching up to US$ 250 billion [14], though it has to be kept in mind that the incidence rate is closely related to such factors as gender, age, life quality, and socio-demographic index [27]. Most of the conditions mentioned require the use of pharmaceutical substances and their application in the surrounding of the eye, on its surface, or inside the eyeball. Also, in most cases, repeated drug applications for extended periods of time are required [28]. First of all, it should be taken into account that the eye is a very specialized sensory organ, separated from systemic circulation, with some distinctive pharmacodynamic and pharmacokinetic properties [29,30]. It is composed of various types of tissues including epithelia, connective tissue, smooth muscles, and vascular and neural network [31,32]. Undoubtedly, no other organ of the body, beside the skin, is so readily available or so easy to observe. However, due to the unique properties, there are specific opportunities but also difficulties in administering drugs to the eye [33]. Ophthalmic preparations represent an obvious alternative to the oral forms, which have many limitations such as low bioavailability due to hepatic circulation and potential food interactions, delayed onset of action, and systemic side-effects [34-36]. In addition, oral or intravenous administration require the use of higher doses in order to achieve the appropriate concentration of drugs in the area of the eyeball [37].

Taking into consideration the unique anatomy of the eye and the challenges related to drug delivery, a few important obstacles can be distinguished. Among the most important ones, physiological processes such as blinking and nasolacrimal drainage, anatomical barriers, efflux pumps, and metabolism in ocular tissues are responsible for drug elimination [38]. It is noteworthy that the tear film is completely replaced with a new one by the tear fluid secreted at a rate of 1.2 mL/min. The eye is also covered with a layer of mucin, which prevents exogenous substances from permeating to the deeper tissues. In the anterior segments of the eye, a few static barriers can be distinguished. The cornea (the corneal thickness is about 0.5 mm [39]) is covered with an epithelium layer consisting of 5–6 layers of closely packed cells equipped with tight junctions. Its thickness is approximately 50 μm [40], and it plays an important protective role. The posterior segment of the eye contains sclera, choroid, Bruch's membrane, and blood–retinal barrier, which further prevent drug permeation. The thickness of the sclera, a membrane composed of randomly scattered collagen fibers, ranges from 0.5 to 1 mm, depending on the region of occurrence [41]. While the sclera is another barrier preventing drug permeation, the choroid is responsible for drug elimination. The blood–retinal barrier is connected to the retinal vascular endothelium with tight junctions hampering the permeation of active ingredients to the intraocular area. When designing non-invasive ophthalmic drug dosage forms, the main aim is to improve the bioavailability by increasing the diffusion across sclera, cornea, and conjunctiva [42]. In the case of externally administered drugs, rate and degree of absorption depend on the time the drug remains at the application site [43]. Up to 95% of the eye surface is covered by the sclera, which is well permeable to substances smaller than 70 kDa, including neuroprotective, antioxidant, or anti-angiogenic agents. For comparison, the cornea permeates substances with a mass not greater than 1 kDa [28]. Unfortunately, transscleral absorption is often reduced by elimination via nasolacrimal drainage pathways, tear protein binding, or drug metabolism [44]. The treatment efficiency is also decreased by constant movement of the eyeball and eyelids, and irrigation with tear fluid [45,46]. For these reasons, in addition to the search for new active pharmaceutical ingredients (APIs), novel technologically advanced ophthalmic drug delivery systems are being developed each year [38,47,48].

Among the ophthalmic preparations, the most commonly used are eye drops [49-51], ointments [52,53], or gels [54,55], containing the drug in a dissolved or suspended form [56,57]. They are applied by medical personnel or by the patient himself to the surface of the eye, to the conjunctival sac, or on the eyelid. Their main disadvantage is the need for frequent dosing, which can be troublesome. Hence, the treatment regimen is rarely followed, leading to a reduction in the effectiveness of the therapy [58,59]. Therefore, apart from designing the vehicle/base composition, drugs are often incorporated into appropriate carriers or introduced into systems whose purpose is to provide the expected concentration in the treated tissue for the desired time period. The most frequently studied and described are liposomes [60,61], micelles [60,62], microparticles [63-65], nanoparticles [66,67], micro- [68,69], and nanoemulsions [70,71]. Unfortunately, it has to be noticed that most technological solu-

tions on the nanoscale are only promising at the laboratory stage. The transfer of such technologies to an industrial scale is often complicated and causes many difficulties [72-74].

Ophthalmic drugs can be also administered in the form of inserts. They are mostly solid or semi-solid forms with the appropriate size and shape, intended to be placed in the conjunctival sac. They consist of an active substance reservoir with a matrix structure or a film that regulates the rate of release of the API. Inserts are used less frequently because their application is difficult, they may cause visual disturbances, and the feeling of the presence of a foreign body in the eye causing discomfort of the patients [75,76]. Inserts can be divided into soluble (biodegradable or bioerodible) and insoluble (therapeutic systems) [77,78]. The advantage of soluble inserts is that they do not have to be removed from the eye. The rate of drug release is influenced by dissolution or erosion of the polymer matrix. Ophthalmic therapeutic systems belong to the group of non-biodegradable inserts from which the drug substance is released by diffusion at a constant controlled rate according to zero-order kinetics [79-81]. Drug-loaded soft contact lenses can be classified as non-dissolving implants [82,83]. Satisfactory results are also obtained with in situ gelling liquid implants [84,85] or film forming liquids [86-88].

In addition to the non-invasive methods mentioned above, there is a number of invasive techniques for the administration of ophthalmic drugs, mostly by injection into the vitreous or subsurface parts of the eye. Subconjunctival and retrobular injections can provide rapid or prolonged release, depending on the composition of the formulation. The most common side effects in this case include local toxicity, tissue damage, eyeball perforation, optic nerve injury, occlusion of central retinal artery or vein, direct retinal toxicity during accidental puncture of the muscles, just to mention the most important [89,90]. In contrast, intravitreal injection is defined as a short and painless procedure, performed under local (drip) anesthesia on an outpatient basis [91]. It is worth mentioning that, after the injection, it is not possible to stop the action of the drug when side or toxic effects occur, among which retinal inflammation is the most commonly described. In order to minimize tissue damage, reduce the disruption of the membrane continuity, eliminate the risk of pathogens infections, ensure faster regeneration and improve the overall safety, the tendency to minimize the size of the needles became a significant trend and led to introduction of microneedles [92-98]. Taking into account the rapid progress in production technologies, it is already possible to obtain needles with a length of less than 1 mm, however, it can be expected that nanometer-sized needles will soon appear in use and revolutionize the treatment of ophthalmic diseases [99]. However, due to the very small size, injections with the use of microneedles require properly trained specialists as well as the use of advanced equipment [95,100].

Simultaneously with the development of single-microneedle technologies, research is focused on microneedle systems/patches for ocular drug delivery. Initially, such arrays were considered as painless, non-invasive, and highly efficient alternative for transdermal, intradermal, and percutaneous delivery of drugs [8,101,102]. Recently, it has been found that they can be successfully applied to the cornea or sclera [103]. Microneedles in skin administration have been studied for many years, including delivery of various therapeutic agents. These included antibiotics [104,105] or antifungals [106] for the treatment of local skin infections but also other drugs intended to achieve systemic action, for example, non-steroidal anti-inflammatory drugs (NSAIDs) [107], antihypertensives [108], and lipid-lowering drugs [109]. Moreover, microneedles (MNs) are broadly investigated as very promising platforms for the delivery of large molecules such as insulin [110] or nucleic acids [111,112]. Another application for which MNs have great potential is vaccine delivery [113-116]. The use of MNs in ophthalmology can still be considered as a fledgling area, however, with great potential but also many unknowns. The presented review summarizes the current data on ophthalmic microneedle patches, their manufacturing techniques, and the obtained therapeutic efficacy. In addition to a number of advantages, the questionable aspects related to this dosage form are also discussed.

2 Types of microneedle: materials, fabrication and properties for drug delivery

2.1 Microneedle system types and properties

Microneedles applied for drug and vaccine delivery, as well as in diagnostics, can be classified according to several different criteria (Figure 1). The most common microneedle typifications are based on the geometry, the material applied to obtain the systems, the method of fabrication, the drug loading technique, and the mode of drug delivery [117]. Concerning the materials used to manufacture the microneedle arrays, the range of available substances is wide. The first material employed for this purpose was silicon. It is important to note that it offers versatile properties and the ability to form different microneedle geometries, which can be considered as an advantage. However, the manufacturing process can be complicated and the material is relatively expensive. Also, silicon is a brittle, non-compatible, and non-biodegradable material, which may cause skin irritation if the needles break and are deposited in the tissue [117,118]. Other non-degradable materials utilized to fabricate microneedles, include metals such as stainless steel [119] and titanium [120], ceramics, such as aluminum oxide [121], or synthetic polymers comprising polyvinylpyrrolidone (PVP) [122],

polyvinyl alcohol (PVA) [123], and polymethacrylates [118,124,125]. Among the biodegradable materials, carbohydrates, including maltose [126], trehalose [127], and sucrose [128], are frequently mentioned. Moreover, biodegradable polymers such as poly(lactic acid) (PLA) [129], poly(glycolic acid) (PGA) [130], and poly(lactic-*co*-glycolic)acid (PLGA) [131] are widely investigated as microneedle materials. Among them, there are hydrogel-forming agents swelling upon the contact with interstitial fluid in the skin during microneedle application. These polymers include poly(ethylene glycol) diacrylate (PEGDA) [132] and poly(acrylic-co-maleic) acid (PAMA) [133]. It is also important to notice that there are numerous studies describing the use of composite materials containing combinations of various substances, both organic and inorganic. For example, studies involving PLA and carbon nanotubes [134], calcium sulfate and gelatin [135], gelatin and hydroxyapatite [136], and PLGA microparticles combined with PLA [137] are available in the scientific literature.

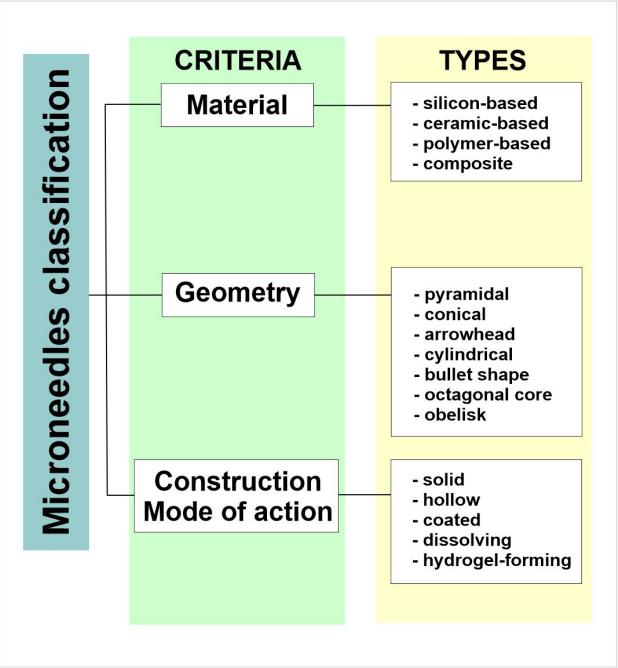


Figure 1: Microneedle classification criteria.

Taking into consideration the shape and geometry of microneedles, they can be categorized as pyramids, cones, arrowheads, cylinders, bullets, octagonal cones, or obelisks [117,138]. Another classification system describing microneedle types is related to their structure and the mode of action (Figure 2).

Solid microneedles are usually investigated in potential dermal drug delivery for skin pretreatment. The systems are used to perforate the epidermis layer and to form channels allowing for better drug permeation to deeper skin layers. In this way, the active ingredient may act locally or reach the capillary vessels in the dermis and enter systemic circulation [117]. A study performed by Wei-Ze et al. [140] revealed that microneedle geometry was important in terms of enhancement of drug permeation across the skin. It was shown that the needles with flat tips were more efficient than the ones with sharp endings. Also, the system efficiency did not correlate with the number of microneedles. Coated microneedles are similar to the previously described type but they have an additional drug-loaded layer at the surface. The active ingredient is deposited in the tissue pierced with the microneedles during the application. It is noteworthy that, in the case of these systems, the drug-loading capacity is usually low. The active layer can be obtained through dipping or spraying with the drug solution, which is usually obtained as a water-based formulation containing also surfactants, thickening agents, and stabilizers. These excipients are necessary to provide the desired properties of the coating layer [114]. Hollow microneedles are similar to conventional needles, with a channel located inside and a hole at the tip. These systems can be used to deliver liquid drug formulations to deeper skin layers, depending on the length of the needles [141]. They have higher drug incorporation capacity compared to the solid and coated systems. Moreover, as they are usually prepared from ceramic materials, silicon, or metal, they display higher stiffness than polymer-based systems. The risk of clogging the internal canals of the needles upon application is mentioned in the literature as a possible drawback of these systems [142]. Dissolving microneedles are intended to deliver active ingredients that are sensitive to heat, as these systems can be prepared from water-based polymer solutions at room temperature. The polymer dissolves in the tissue after the administration and the incorporated drug is released in this way. The dissolution time required to deliver the full amount of the drug is usually a few minutes; therefore, these microneedles are frequently designed to separate from the pedestal and remain in the tissue [114]. Among the most important disadvantages of dissolving microneedles, a low mechanical strength resulting in difficulties with piercing the tissues is mentioned. Some of the polymers employed in the manufacturing process are hygroscopic, which can also decrease the physical stability of the final product [143]. Other polymer-based microneedles are hydrogel-forming systems, which are obtained with the use of hydrophilic substance swelling upon the contact with the fluid at the administration site. It is noteworthy that the polymer matrix does not dissolve under physiological conditions and can be removed after the drug is released [117,144]. As the microneedles absorb interstitial fluid from the surrounding tissue, they can be utilized not only as drug delivery systems but also as minimally invasive diagnostic tools [145,146]. The advantages of hydrogel-forming systems include relatively high drug-loading capacity and the possibility to modify the drug

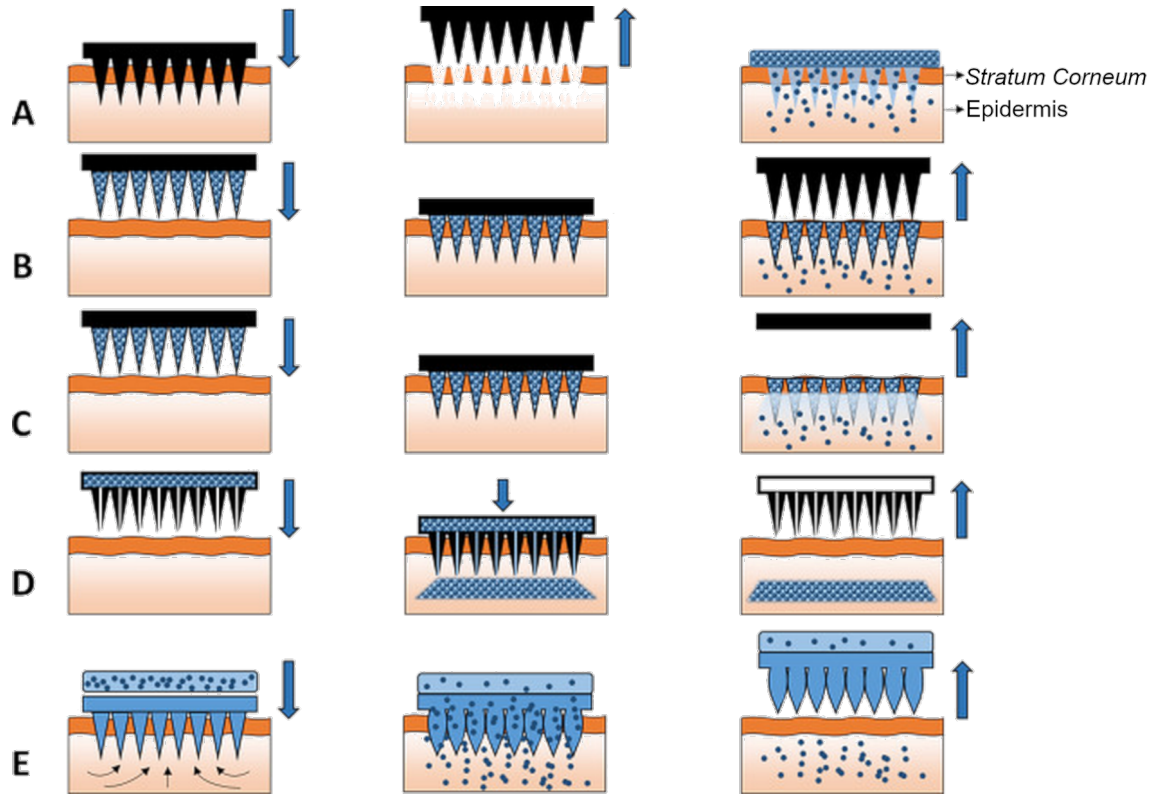


Figure 2: A schematic representation of five different MN types used to facilitate transdermal drug delivery. (A) Solid MNs for increasing the permeability of a drug formulation by creating microholes across the skin. (B) Coated MNs for rapid dissolution of the coated drug into the skin. (C) Dissolvable MNs for rapid or controlled release of the drug incorporated within the MNs. (D) Hollow MNs used to puncture the skin and enable the release of a liquid drug following active infusion or diffusion of the formulation through the needle bores. (E) Hydrogel-forming MNs take up interstitial fluids from the tissue, inducing diffusion of the drug located in a patch through the swollen microprojections. Figure 2 was reproduced from [139] (© 2016 E. Larraneta et al., published by Elsevier B.V., distributed under the terms of the Creative Commons Attribution 4.0 International License, https://creativecommons.org/licenses/by/4.0/).

release rate with respect to the individual needs, which is usually achieved through adjusting the polymer crosslinking ratio [147]. Moreover, the polymers usually employed in this type of formulation are biocompatible, which decreases the toxicity risk [144].

2.2 Microneedle manufacturing methods

The selection of a manufacturing technique should take into account the intended use of the microneedle system and the material from which it is to be made. In addition, the technique must be adapted to the properties of the drug.

The most common materials used in the production of microneedles are silicon, ceramics, and metals, such as stainless steel and titanium. Also, biodegradable polymers such as poly(lactic acid), poly(glycolic acid), and non-biodegradable polymers, for example, photolithographic epoxy resins are used [148]. The methods used for the production of microneedles include lithographic or laser techniques, casting, and 3D printing, to mention a few. The laser cutting technique can be used to produce microneedles from metals or polymers. The main part of the process is cutting microneedles out of a plate with a laser and then bending them. The alignment of the tips can be achieved by electropolishing [149]. A similar technique is laser ablation. In this case, the substrate, absorbing the laser beam, heats up and evaporates or sublimes, which yields engraved 3D patterns [150].

In the fused deposition modelling (FDM) method, the thermoplastic material is heated to its softening point, then extruded through a nozzle and applied layer by layer to the build plate where it quickly solidifies [151]. In the microstereolithographic method, a prepared polymer or a mixture of polymers undergoes polymerization under the influence of a high-energy light source (e.g., UV radiation) [150]. Digital light processing (DLP) is also a technology based on photopolymerization of photosensitive polymers, but in this case each layer of the polymer is projected as whole [152].

A more complicated method is two-photon polymerization (TPP), which uses a near-infrared beam instead of UV radiation. TPP initiates the polymerization of the resin by multiphoton absorption [153].

An alternative to methods using UV or heat is the droplet-born air blowing method (DAB). It is suitable for drug molecules that can be inactivated. In this method, polymer droplets are placed between two sheets. As the sheets are pulled apart, the droplets elongate and the resulting needle-shaped matrices are dried by the flowing air [154,155].

Another well-known method is photolithography. In this technique, a silicon wafer is covered with a photosensitive or photoresistant polymer. The plate is then exposed to UV radiation. A pattern is formed depending on the coverage of the photosensitive or photoresistant layer. The wafer is then etched. A distinction can be made between wet and dry etching. The wet etching process uses a potassium hydroxide solution, while dry etching includes the physical methods ion milling and sputtering and the chemical method high-pressure plasma [156]. Lithographic techniques can be also used to prepare molds for the micromolding method. Micromolding, also known as solvent casting, is quite popular due to cost-effectiveness and simplicity. This method uses a mold usually made of silicone. The prepared mold is filled with a polymer solution or mixture. Then, air voids are removed with a centrifuge or through vacuum and the mold is baked in the oven. After cooling down, the finished microneedles are removed from the matrix [151,156,157]. This type of method is chosen to obtain microneedles for ophthalmic use [158-160].

Methods of drug-loading depend on the type and construction of the manufactured microneedles, as well as the applied material. The properties of the drug must be carefully taken into consideration, as some active ingredients may decompose at higher temperatures or upon irradiation. In the case of solid microneedles prepared with the use of porous ceramic materials, the pores in the carrier material can be filled with the active ingredient in liquid or solid form. In the first case, the drug diffuses from the solution in the microneedle pores upon application. In the other case, the drug solution is loaded to the microneedles and in the next step the formulation is dried and the drug precipitates inside the pores. Upon application, the drug dissolves in a physiological fluid and, in this form, can permeate to the deeper tissues [161]. In the techniques involving polymers applied to obtain solid microneedles, the drug may be dissolved [162,163] or suspended [164] in the polymer or monomer solution. In the manufacturing of more complex systems, with the active ingredient incorporated in a specific compartment of a microneedle, more complex procedures involving both drug-loaded and drug-free solutions may be employed [165]. Hollow microneedles containing an empty canal inside are usually filled with active ingredient solution, either passively or with the use of pressure-driven methods [161]. In the systems using passive diffusion, the drug solution can be loaded to the canals inside the microneedles [141] or to an external compartment [166]. In pressure-driven systems, a reservoir with different pumping mechanisms is attached to the microneedle systems. Usually, manually operated syringes are reported [167,168], as well as micropumps [169] or actuator-equipped devices designed for self-injection [170].

In coated microneedles the drug is deposited in the form of a thin layer on the external surface of the microneedle. Various coating techniques have been reported in the literature and summarized elsewhere [171-173]. The simplest method is dip coating, in which the microneedle array is immersed in the coating liquid and left to dry afterwards. The drying procedure can be accelerated with the aid of gas-jet drying. Another technique involves spray coating, which is technologically similar to the coating of oral solid dosage forms. Electrohydrodynamic atomisation (EHDA), in which electrically charged droplets are deposited on the microneedle surface, has been mentioned. As in piezoelectric inkjet printing, the droplets are released from the nozzle as a result of the application of an electrical field to a piezoelectric crystal, which distorts and pushes the liquid out. The most important techniques applied in microneedle coating are depicted in Figure 3 [171].

3 An overview of microneedle systems for ocular drug delivery

Considering the construction and the mechanism of action, four types of MNs used to deliver a drug to the eye can be distinguished in the scientific literature: (i) Solid MNs, used mostly for puncturing a biological membrane and forming pores, which are further used as canals for drug delivery. In the next step, MNs are removed and the pores are filled with a drug-loaded formulation. (ii) Drug-coated MNs with a drug-loaded layer deposited on the surface; the coating layer dissolves in physiological fluids upon administration and the active ingredient diffuses to the deeper regions. (iii) Dissolving MNs that contain the active ingredient dispersed in the MN matrix. The matrix is prepared with the use of soluble or biodegradable materials, and, upon insertion, the matrix-forming agent gradually dissolves or is hydrolyzed and the drug is released. (iv) Hollow MNs that contain an empty space inside. Usually, these devices are attached to a pressure-driven unit that pushes the drug-loaded liquid through the canal into the target site [174].

All microneedle systems administered to the eye are currently at the stage of development and basic research, but the interest in

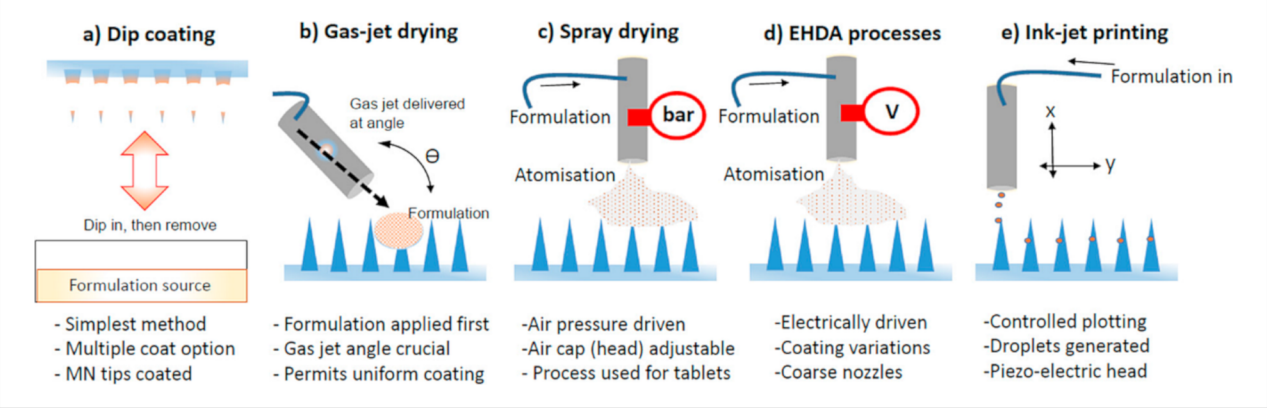


Figure 3: Illustrated examples of techniques used to coat MNs. (a) Dip coating. (b) Gas-jet drying. (c) Spray drying. (d) EHDA processes. (e) Ink-jet printing. Figure 3 was reproduced from [171] (© 2015 R. Haj-Ahmad et al., published by MDPI, distributed under the terms of the Creative Commons Attribution 4.0 International License, https://creativecommons.org/licenses/by/4.0/).

them is systematically growing, which is reflected in numerous scientific and popular science publications. Microneedle ocular patches for the delivery of pilocarpine, a model drug usually employed in the treatment of glaucoma, was developed by Roy et al. The MN matrix consisted of PVA and PVP and contained 1 mg of the drug. The patches were fabricated by micromolding and mimicked the shape of commercial contact lenses (Figure 4). The patches were tested ex vivo with the use of excised human cornea and porcine eye globe. The amount of the drug that permeated across the cornea was distinctly higher from the microneedle system in comparison to the standard solution [160].

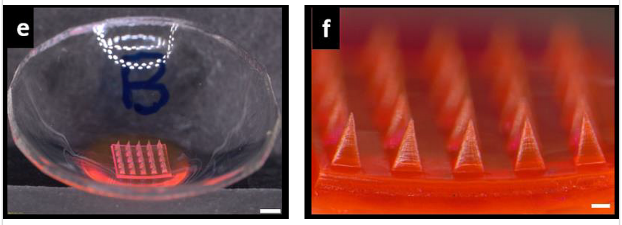


Figure 4: Stereomicroscopic image of the microneedle patch (e) and magnification of the microneedles (f), scalebars represent 1 mm and 200 µm respectively. Figure 4 was reproduced from [160] ("Microneedle ocular patch: fabrication, characterization, and ex-vivo evaluation using pilocarpine as model drug", by G. Roy et al., Drug Development and Industrial Pharmacy, published on 11 Jun 2020 by Taylor & Francis Ltd), reprinted by permission of the publisher (Taylor & Francis Ltd, http://www.tandfonline.com). This content is not subject to CC BY 4.0.

In a subsequent work, the authors presented two types of patches for the delivery of triamcinolone acetonide (TA), a model steroidal drug applied in numerous inflammatory conditions to the posterior segment of the eye. A microneedle scleral patch (MSP) and a microneedle corneal patch (MCP) were obtained by micromolding with the use of PVP. The ex vivo experiments performed on porcine eye globe showed that, in comparison to MCP and TA nanosuspension, MSP yielded much greater TA concentrations in the vitreous humor and choroid-retinal complex after 5 min of application. Moreover, the patches were tested with a rabbit eye model. In this case, after 24 h, significantly higher TA accumulation was observed for MSP in comparison to MCP and intravitreal injection [175].

Albadr et al. designed a rapidly dissolving MN patch for ocular delivery of amphotericin B for the treatment of corneal fungal infections (Figure 5). The patch was manufactured from a blend of PVP and hyaluronic acid (HA) by molding. The components of the MN matrix ensured a very fast dissolution, approximately 30 s, in which the active substance was completely released, followed by a rapid onset of action. At the same time, it was emphasized that the manufacturing process did not reduce the antifungal activity of the drug [176].

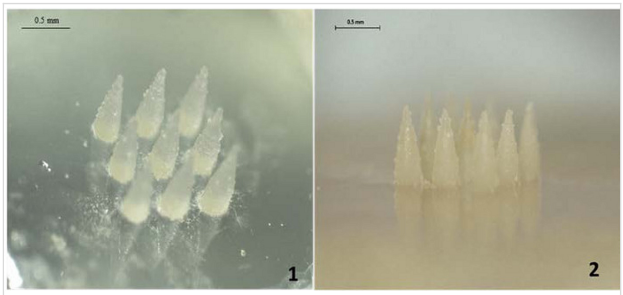


Figure 5: Microscopic image of dissolving MNs manufactured by Albadr and co-workers. Figure 5 was reproduced from [176] (© 2021 A. A. Albadr et al., distributed under the terms of the Creative Commons Attribution 4.0 International License, https://creativecommons.org/licenses/by/4.0/).

Shi et al. proposed PLA/HA MNs for the ocular delivery of fluconazole, a widely known antifungal agent, employed in this formulation for potential keratitis treatment. As justification for the use of PLA, the authors indicated poor mechanical proper-

ties of HA and the associated risk of needle deformation during production and application. PLA served both as a scaffold to increase the matrix stability and to provide prolonged drug release. It was observed that the patches penetrated the rabbit corneal epidermis without irritation and, after removal, total recovery was observed after 12 h. The developed patch showed great potential as an alternative to ocular injection [177]. Amer and Chen fabricated PVA hydrogel-based microneedle arrays for the delivery of immunoglobin G1, a model protein resembling bevacizumab, a monoclonal antibody applied in the treatment of age-related macular degeneration (AMD) (Figure 6). First, the master mold was produced with the use of a light processing-based 3D printing technique. Then its shape was imprinted in the elastomer (Sylgard® 184) and the prepared form was used to obtain the final microneedles by molding. The in vitro tests with the use of a Parafilm/polyethylene/nylon membrane equivalent and a fluid mimicking vitreous humor showed extended release of the active compound, compared to the rapid release after injection. The authors indicated that the MN arrays show a much more uniform drug release profile than the single injections [178].

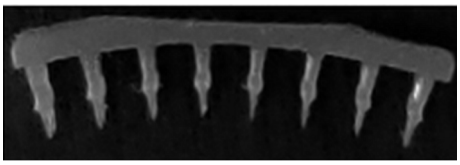


Figure 6: Microscopic image of the MNs obtained by Amer and Chen. Figure 6 was adapted from [178], M. Amer; R. K. Chen, "Hydrogel-Forming Microneedle Arrays for Sustained and Controlled Ocular Drug Delivery", Journal of Engineering and Science in Medical Diagnostics and Therapy, with permission from ASME. Copyright 2020 ASME. This content is not subject to CC BY 4.0.

As a continuation of the previous studies the authors created stimuli-sensitive bifunctional hydrogel microneedle arrays. In the first stage, after placing the patch on the eyeballs and piercing the membrane, the needles swelled and, as a result, wedged. Then, after the drug was released, the patch had to be irradiated by UV light (365 nm, 10 mW/m^2) for 14 min with an OmniCure S2000 Spot Curing System (Excelitas Technologies, Waltham, MA) to cause the needles to shrink by about 20%, so they could be easily removed without the risk of damaging the eye. The MN matrix contained a mixture of PVA and spiropyran-conjugated *N*-isopropylacrylamide (NIPPAM) [179].

Suriyaamporn et al. employed a computer-aided design for the optimization of microneedle systems based on hyaluronic acid and a copolymer of methyl vinyl ether and maleic anhydride (Gantrez®S-97) produced by micromolding (Figure 7). Fluorescein sodium (FS) was used as a model compound with hydrophilic properties. Multiple parameters were evaluated, namely the physical and mechanical properties, ocular permeation, FS remaining in ocular tissue, dissolution time, insertion force, insertion depth, and ex vivo ocular drug delivery. The permeation studies on porcine eyeballs showed that, after application of the MN patches, the total amount of released dye was close to 18%, whereas from flat patches only 1% was released after 24 h [180].

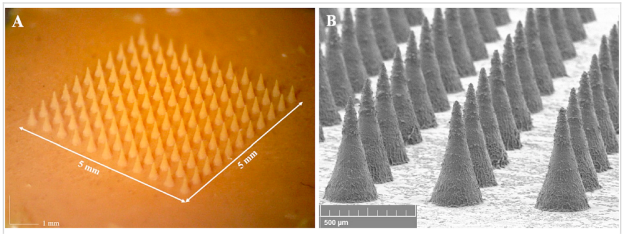


Figure 7: The physical appearance of 20.06% GAN + 5% HA + 1% FS under (A) digital microscope and (B) scanning electron microscope (×131). Figure 7 was reprinted from [180], Journal of Drug Delivery Science and Technology, vol. 61, by P. Suriyaamporn; P. Opanasopit; T. Ngawhirunpat; W. Rangsimawong, “Computer-aided rational design for optimally Gantrez® S-97 and hyaluronic acid-based dissolving microneedles as a potential ocular delivery system“, article no. 102319, Copyright (2021), with permission from Elsevier. This content is not subject to CC BY 4.0.

Li et al. fabricated PVP-based MNs for the ocular delivery of the insoluble drug brinzolamide, a carbonic anhydrase inhibitor applied in the treatment of glaucoma. The authors coated the microneedle matrix with a mixture of the drug with PVP and ethanol. Then, after evaporation of the solvent and solidification of the polymer with the drug, demolding was performed. In vivo studies on an animal model (rat) showed rapid in vitro drug release with 93% accumulative release at 2 h and a high corneal permeation of the drug [181]. Bhatnagar et al. employed micromolding techniques for the preparation of dissolving MNs for the corneal delivery of besifloxacin hydrochloride, a fluoroquinolone antibiotic useful in the treatment of bacterial infections. Due to blending of PVA and PVP, the obtained material revealed an appropriate mechanical strength to reach penetration depth up to 200 µm. The degree of drug penetration across human excised cornea after 24 h was assessed for the traditional suspension used for 5 min or 24 h and after 5 min of contact with the microneedles. The suspension used for 5 min was almost five times less effective than the MNs [158]. Nanoparticle-loaded bilayer dissolving microneedle arrays for the sustained delivery of proteins to the posterior region of the eye were developed by Wu and co-workers (Figure 8). Ovalbumin, a model protein, was encapsulated in PLGA-based nanoparticles by a water-in-oil-in-water double emulsion method. The nanoparticles were used to form microneedles in combination with various types of PVA. Then, after drying, a

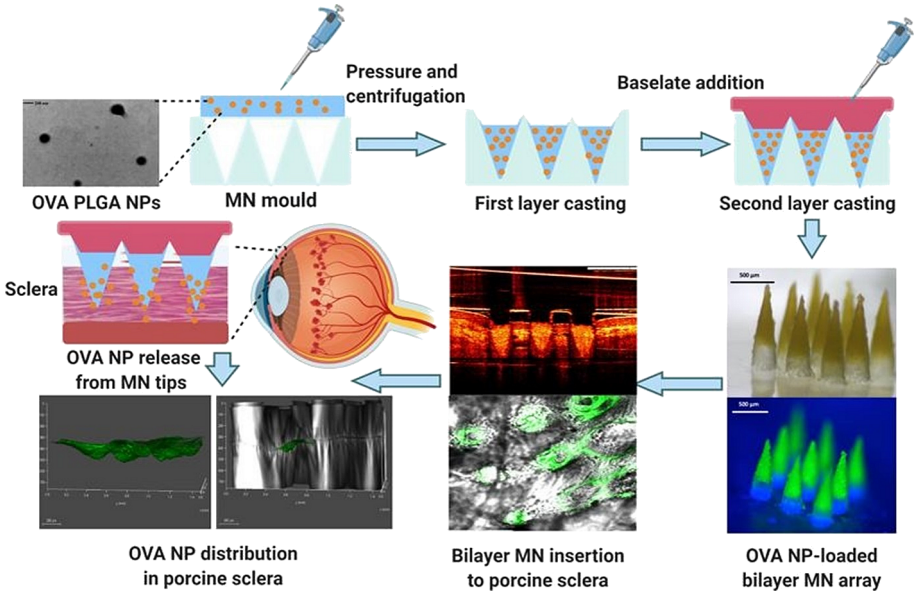


Figure 8: Individual steps in the production and use of microneedles containing nanoparticles developed by Wu and co-workers. Figure 8 was reprinted from [182], European Journal of Pharmaceutics and Biopharmaceutics, vol. 165, by Y. Wu; L. K. Vora; Y. Wang; M. F. Adrianto; I. A. Tekko; D. Waite; R. F. Donnelly; R. R. S. Thakur, "Long-acting nanoparticle-loaded bilayer microneedles for protein delivery to the posterior segment of the eye", pages 306-318, Copyright (2021), with permission from Elsevier. This content is not subject to CC BY 4.0.

base layer made of an aqueous hydrogel was attached. It turned out that the MNs had adequate mechanical stability to puncture the sclera and then degraded very quickly releasing the nanoparticles (NPs) in less than 3 min. In turn, the slow disintegration of the NP-forming matrices resulted in the release of the active ingredient in a prolonged manner [182].

Lee et al. drew attention to the inconvenience of applying the MN patches to the surface of the eye, resulting from the constant movements of the eyeball and eyelid. The authors also pointed to the potential risk of hypoxia of the eye surface as a result of long presence of the patches on its surface necessary to assure the therapeutic effect. As a solution, the authors proposed administering the drug in the form of a single microneedle with detachable tip, which remains in the cornea for a certain period of time, ensuring sustained release (Figure 9). Two model drugs were used, namely FITC-dextran for the determination of release profiles and polyhexamethylene biguanide, an antimicrobial agent, for in vivo assessment of therapeutic efficiency. The drug-containing tip after optimization was delivered to the mouse cornea and efficiently reduced the progression of keratitis [183].

The same group developed another rapidly detachable MN. The new idea was to modify the previously described concept by adding an additional fast dissolving layer separating the drug tip from the microneedle base. The layer consisted of a porous

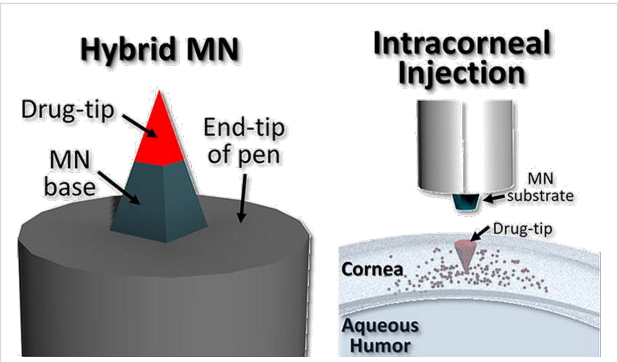


Figure 9: The hybrid detachable microneedle developed by Lee et al. Figure 9 was adapted from [183], Acta Biomaterialia, vol. 80, by K. Lee; H. B. Song; W. Cho; J. H. Kim; J. H. Kim; W. H. Ryu, "Intracorneal injection of a detachable hybrid microneedle for sustained drug delivery", pages 48-57, Copyright (2018), with permission from Elsevier. This content is not subject to CC BY 4.0.

blend of PVA/PVP. Optimization of the composition and manufacturing process enabled almost immediate release of the tip upon contact with tear fluid and placing it at the appropriate depth applying manual pressure (Figure 10) [184].

Than et al. fabricated corneal patches (2 × 2 mm) with self-implantable needle-shape microreservoirs (Figure 11). The microneedles were obtained by a simple micromolding method. The outer layer consisted of methacrylated hyaluronic acid (MeHA), while the interior was filled with unmodified HA. The

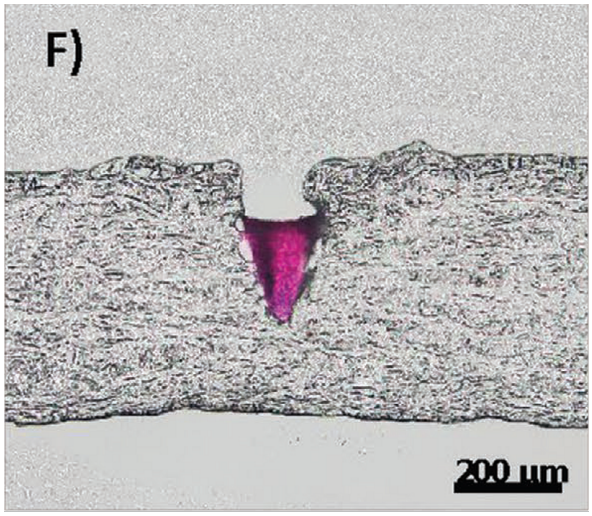


Figure 10: Cryo-sectioned optical image of a MN tip (stained with rhodamine B) embedded in the sclera by Lee et al. Figure 10 was reproduced from [184], Y. Lee et al., "Rapidly Detachable Microneedles Using Porous Water-Soluble Layer for Ocular Drug Delivery", Advanced Materials Technologies, with permission from John Wiley and Sons. © 2020 WILEY-VCH Verlag GmbH & Co. KGaA, Weinheim. This content is not subject to CC BY 4.0.

needles were, in turn, attached to the HA patch. This design ensured the needles to detach immediately after application. Then, the inner layer of HA quickly degraded and the drug was released, while the MeHA shell acted as a depot form. Describing in vivo experiments with the use of animal (rat) corneal neovascularization as a disease model, the authors presented that delivering an anti-angiogenic monoclonal antibody (DC101) by such an eye patch caused a reduction of the area of neovascularization by about 90%. Moreover, due to the double compartment structure of the MNs, the rapid release of the anti-inflammatory compound (diclofenac) from the fast dissolving HA-based core provided a synergistic effect with the sustained release of DC101 from the outer layer. The authors also emphasized that it is possible to produce needles containing more than two compartments with different drugs [185].

In order to improve the transport of the steroidal drug diflupredate, applied in the treatment of anterior uveitis, to posterior regions of eye, Shelley et al. developed detachable two-component MN patches for extended release of the drug. The microneedles were made of Resomer, while the detachable layer was made of poly(acrylic acid) (PAA) [186]. This combination ensured that the needles were quickly inserted into the eye space followed by a slow release of the drug.

Datta et al. fabricated a lens-shaped MN patch of PVP for rapid corneal delivery of the macromolecular drug cyclosporine A (CsA) applied against uveitis, corneal injuries, vernal keratoconjunctivitis, and other diseases with underlying inflammatory processes. Due to the composition, the MNs degraded and entirely dissolved within 60 s. The ex vivo experiments on pig excised cornea showed that, in comparison to Cyclomune eye drops, the application of the MNs resulted in higher values of drug flux and retention. CsA was evenly distributed within interior parts of the eye [187].

The presented studies indicate that the most important scientific research directions related to microneedles applied in ophthalmic drug delivery are focusing on hydrophilic matrices, mostly obtained with the use of PVP, PVA, and hyaluronic acid or its derivatives via molding techniques. It was shown that with these materials both suitable mechanical parameters and quick drug release can be obtained, which is crucial in terms of therapeutic efficacy and patient comfort. The obtained systems were either planar patches or were shaped into a contact lens, which provides ease of administration. It is also noteworthy that some of the presented dosage forms were rapidly dissolving microneedles and did not require prolonged contact with the eyeball surface thereby decreasing eye irritation and discomfort during application. However, this issue should be thoroughly investigated before releasing any microneedle array-based formulation to the pharmaceutical market. As can be concluded from the presented studies, the current state of knowledge is related mostly to physicochemical parameters and the number of

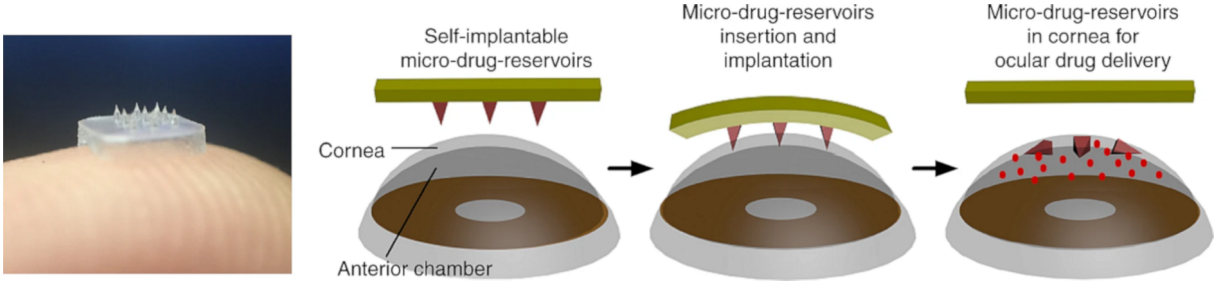


Figure 11: The photography and the principle of operation of patches developed by Than et al. Figure 11 was reproduced from [185] (© 2018 A. Than et al., distributed under the terms of the Creative Commons Attribution 4.0 International License, https://creativecommons.org/licenses/by/4.0/).

studies performed with the use of in vivo models is rather limited. It is also noteworthy that the available data refer to animals and, to the best of our knowledge, no studies performed with human volunteers have been published so far.

4 Advantages and disadvantages of microneedle systems for ophthalmic drug delivery

Microneedle arrays as potential drug delivery systems offer numerous advantages, including ease of administration without professional assistance, the ability to overcome the external barriers of the human body decreasing the effectiveness of topical formulations, and minimal invasiveness. Ocular drug administration is usually associated with many challenges; poor bioavailability is among the most important ones [188]. Specific physiological conditions present in this body region are responsible for quick drug removal from the surface of the eyeball and for relatively short residence times of the formulation after administration. Reaching the posterior eye segment is even more difficult due to its poor accessibility and natural barriers of the eye [189]. According to the available scientific reports, microneedles offer some possible therapeutic improvements compared with the conventional formulations, which is accompanied by a better patient acceptability when classical intraocular injections are taken into consideration. However, it must be emphasized that dealing with this sensitive organ is usually associated with possible discomfort, even in the case of relatively soft formulations, like eye drops, gels and contact lenses. It is also important to note that even though the described microneedle systems are minimally invasive, there is a risk of infection and inflammation at the administration site, which may result in further discomfort and pain. One of the most appropriate directions seems to be the design of patches with easily detachable or dissolving microneedles. This is due to the fact that leaving the patch on the surface of the eye for a long time is certain to cause discomfort to patients. It is also extremely interesting to be able to produce such patches using 3D printing techniques, which repeatedly enable the introduction of appropriate doses of APIs, but also allow the amount to be adjusted to the requirements of a given disease and for a specific patient. In order to evaluate the actual relevance of the described systems, clinical trials involving human volunteers are crucial, as it was already mentioned by Dugam and co-workers [8]. However, to the best of our knowledge, all completed clinical studies related to microneedle-based formulations do not involve microneedle arrays but single microneedle devices [190]. It is obvious that further investigations are necessary to define the directions of formulation development and to find the most important limitations of these systems. The currently available reports describe mostly formulation studies and the results of in vivo tests employing animal models. It must be emphasized that the results are usually promising and show the potential for scientific and clinical development of microneedle arrays.

5 Future directions

As was shown in the reviewed studies, the advantages of microneedles as ocular drug delivery systems are indisputable, even though there are also some important drawbacks. Taking into consideration the materials and methods employed in the literature studies, it is obvious that the most important trends in this area focus on quickly dissolving systems obtained with the use of hydrophilic polymers. These formulations are intended for short residence times at the eye surface to minimize the discomfort and the risk of side effects, including irritation, tissue damage, infection, and inflammation. However, the data regarding the possible risk related to ophthalmic microneedles is still insufficient and this area requires further investigation. As most of the safety issues still need to be studied in detail, there are currently no attempts to introduce any microneedle-based ophthalmic formulation to the pharmaceutical market, except for those containing a single microneedle instead of microneedle arrays. However, some important lessons can be learned from the studies describing single microneedle injections. Depending on the number of parameters, including, for example, the injected liquid volume, the formulation can be perceived by the patient as painful or acceptable [98]. Therefore, all these factors must be carefully considered and optimized. As we already mentioned, there is also a need for randomized clinical studies using microneedle arrays.

Another important challenge related to ophthalmic drug delivery systems in general is sterility. In order to provide the drug stability but also the stability of the polymers applied to obtained system, an appropriate sterilization method must be selected and optimized. So far, this issue has not been properly addressed and thoroughly investigated, as can be concluded from the limited scientific literature on this subject.

Conclusion

The treatment of ocular diseases, especially those localized in the deeper tissues, can be challenging due to the poor accessibility of eye tissues, as well as anatomical and physiological barriers present in the eyeball. The conventional therapeutic approaches, including topical formulations such as eye drops and gels, as well as systemic ones, frequently prove to be ineffective, which is related to poor bioavailability of the drug. As an alternative, direct injections into the eye tissues have been proposed. However, this approach is associated with significant side effects and poor acceptability by the patient due to the high invasiveness. Microneedles can be considered as a minimally invasive compromise between the topical formulations, which

are acceptable but reveal poor effectiveness, and direct injections, which are more effective but invasive. With this novel approach, the active ingredient can be delivered to the target site with good precision and minimized risk of tissue damage, pain, and infection [98]. This article presents the most important difficulties that must be taken into consideration regarding ophthalmic drug delivery, as well as the current research directions explored in the field of MNs investigated as drug delivery systems. As it was already mentioned, the presented studies indicate that these novel systems reveal an enormous potential related mostly to their minimal invasiveness and the possibility to administer them without any professional assistance. These advantages are extremely important in terms of patient compliance and may significantly contribute to the improvement of treatment efficacy. Table 1 summarizes the most important information about the research described in this review.

Table 1: Summary table containing the most important information discussed in the review, sorted chronologically.

API/active agent (activity, condition treated)	MN system	Matrix composition	Fabrication technique	Effects/conclusions	Ref.
FITC-dextran (model drug) and polyhexamethylene biguanide (model antimicrobial)	detachable hybrid MN pen	MN base: SU-8 resin detachable tip: PLGA	premolding/ pressure-assisted transfer molding	drug containing tip after optimization was delivered to the mouse cornea and efficiently reduced progression of keratitis	[183]
immunoglobulin G (model antiagiogenic agent)	self-implantable microneedle patch	methacrylated HA	cross-linking, molding	due to the double compartment structure of the MNs the rapid release of the anti-inflammatory compound (diclofenac) from the fast dissolving HA-based core provided the synergistic effect with the sustained release of DC101 from the outer layer	[185]
besifloxacin HCl (antibiotic, bacterial infections)	hydrogel MNs	PVA/PVP	micromolding	sufficient mechanical strength to reach 200 µm penetration depth; MNs were much more efficient than traditional suspension	[158]
pilocarpine (reduction of intraocular pressure, glaucoma)	contact lens-shaped MN system	PVA/PVP	micromolding	better permeation across the cornea in vivo in comparison to drug solution	[160]
immunoglobulin G1 (model for bevacizumab molecule)	self-adhesive MN patch	PVA	micromolding with the use of 3D printed master mold	prolonged in vitro release up to 4 weeks in comparison to injection	[178]
—	rapidly detachable MN pen	MN base: SU-8 resin dissolving layer: PVA/PVP detachable tip: PLGA	micromolding	optimization of the composition and manufacturing process enabled almost immediate release of the tip upon contact with tear fluid	[184]
—	Photo-responsive hydrogel MN system	polyvinyl alcohol and spiropyran-conjugated N-isopropylacrylamide	micromolding	easy detachment of the patch after drug release due to the light-induced shrinkage of the matrix	[179]
ovalbumin encapsulated in NPs (model)	fast dissolving MN bilayer patch	PVA	molding, high speed centrifugation	rapid dissolution of MNs, less than 3 min	[182]

Table 1: Summary table containing the most important information discussed in the review, sorted chronologically. (continued)

fluorescein sodium (model compound)	dissolving MNs	HA/Gantrez® S-97	micromolding	permeation studies on porcine eyeballs showed that due to application of the MN patches the total amount of released dye was close to 18%, whereas from flat patches only 1% was determined after 24 h	[180]
brinzolamide (carbonic anhydrase inhibitor; glaucoma treatment)	dissolving MNs	PVP K90	casting/demolding	rapid in vitro drug release at 2 h, high corneal permeation	[181]
amphotericin B (antifungal)	rapid dissolving MN patch	PVP/HA	micromolding	degradation of the MN up to 30 s, fast onset of drug action	[176]
fluconazole (antifungal)	dissolving MN array patch	PLA/HA	micromolding	satisfactory drug intracorneal pentration with no irritation and tissue recovery up to 12 h	[177]
difluprednate (anti-inflammatory)	rapid dissolving MNs	poly(D,L-lactide-co-glycolide)	micromolding	matrix diffusion-controlled release over the 7-day	[186]
triamcinolone acetonide (anti-inflammatory)	microneedle scleral patch	PVP	micromolding	greater safety score compared with intravitreal injection	[191]
cyclosporine A (immunosupressant, uveitis and other inflammatory conditions)	dissolving MNs	PVP	micromolding	completely dissolve in the cornea within 60 s, enhanced flux and retention of the drug	[187]

ORCID® iDs

Piotr Gadziński - https://orcid.org/0000-0001-7577-7410
Anna Froelich - https://orcid.org/0000-0002-1491-1329
Monika Wojtyłko - https://orcid.org/0000-0002-2672-6171
Antoni Białek - https://orcid.org/0000-0001-8838-2805
Julia Krysztofiak - https://orcid.org/0000-0002-7158-4870
Tomasz Osmałek - https://orcid.org/0000-0002-6939-2888

References

1. Chirra, H. D.; Desai, T. A. *Adv. Drug Delivery Rev.* **2012,** *64,* 1569–1578. doi:10.1016/j.addr.2012.08.013
2. Herrero-Vanrell, R.; Vicario de la Torre, M.; Andrés-Guerrero, V.; Barbosa-Alfaro, D.; Molina-Martínez, I. T.; Bravo-Osuna, I. *J. Drug Delivery Sci. Technol.* **2013,** *23,* 75–102. doi:10.1016/s1773-2247(13)50016-5
3. Sun, J.; Yang, Z.; Teng, L. *Dose-Response* **2020,** *18,* 1559325820907810. doi:10.1177/1559325820907810
4. Sanjay, S. T.; Dou, M.; Fu, G.; Xu, F.; Li, X. *Curr. Pharm. Biotechnol.* **2016,** *17,* 772–787. doi:10.2174/1389201017666160127110440
5. Meng, E.; Sheybani, R. *Ther. Delivery* **2014,** *5,* 1167–1170. doi:10.4155/tde.14.90
6. Sadikot, R. T. *Adv. Drug Delivery Rev.* **2014,** *77,* 27–31. doi:10.1016/j.addr.2014.07.004
7. Andrés-Guerrero, V.; Bravo-Osuna, I.; Pastoriza, P.; Molina-Martinez, I. T.; Herrero-Vanrell, R. *J. Drug Delivery Sci. Technol.* **2017,** *42,* 181–192. doi:10.1016/j.jddst.2017.07.001
8. Dugam, S.; Tade, R.; Dhole, R.; Nangare, S. *Future J. Pharm. Sci.* **2021,** *7,* 19. doi:10.1186/s43094-020-00176-1
9. Khandan, O.; Kahook, M. Y.; Rao, M. P. *Sens. Actuators, B* **2016,** *223,* 15–23. doi:10.1016/j.snb.2015.09.071
10. Kim, H. M.; Woo, S. J. *Pharmaceutics* **2021,** *13,* 108. doi:10.3390/pharmaceutics13010108
11. Foreman, J.; Xie, J.; Keel, S.; van Wijngaarden, P.; Taylor, H. R.; Dirani, M. *Sci. Rep.* **2017,** *7,* 8757. doi:10.1038/s41598-017-09421-9
12. Mondal, K.; Mandal, N. Role of Bioactive Sphingolipids in Inflammation and Eye Diseases. In *The Role of Bioactive Lipids in Cancer, Inflammation and Related Disease;* Honn, K. V.; Zeldin, D. C., Eds.; Advances in Experimental Medicine and Biology; Springer International Publishing: Cham, 2019; pp 149–167. doi:10.1007/978-3-030-21735-8_14
13. Pascolini, D.; Mariotti, S. P. *Br. J. Ophthalmol.* **2012,** *96,* 614–618. doi:10.1136/bjophthalmol-2011-300539
14. Vision impairment and blindness https://www.who.int/news-room/fact-sheets/detail/blindness-and-visual-impairment (accessed Jul 19, 2022).

15. Mesquida, M.; Drawnel, F.; Fauser, S. *Semin. Immunopathol.* **2019,** *41,* 427–445. doi:10.1007/s00281-019-00750-7
16. Lollett, I. V.; Galor, A. *Clin. Ophthalmol.* **2018,** *12,* 125–139. doi:10.2147/opth.s126668
17. Pall, B.; Gomes, P.; Yi, F.; Torkildsen, G. *Cornea* **2019,** *38,* 713–717. doi:10.1097/ico.0000000000001911
18. Moisseiev, E.; Loewenstein, A.; Yiu, G. *Clin. Ophthalmol.* **2016,** *10,* 173–178. doi:10.2147/opth.s89784
19. Nielsen, B. R.; Alberti, M.; Bjerrum, S. S.; la Cour, M. *Acta Ophthalmol.* **2020,** *98,* 603–606. doi:10.1111/aos.14380
20. Ammar, M. J.; Hsu, J.; Chiang, A.; Ho, A. C.; Regillo, C. D. *Curr. Opin. Ophthalmol.* **2020,** *31,* 215–221. doi:10.1097/icu.0000000000000657
21. Wielders, L. H. P.; Schouten, J. S. A. G.; Winkens, B.; van den Biggelaar, F. J. H. M.; Veldhuizen, C. A.; Findl, O.; Murta, J. C. N.; Goslings, W. R. O.; Tassignon, M.-J.; Joosse, M. V.; Henry, Y. P.; Rulo, A. H. F.; Güell, J. L.; Amon, M.; Kohnen, T.; Nuijts, R. M. M. A. *J. Cataract Refractive Surg.* **2018,** *44,* 429–439. doi:10.1016/j.jcrs.2018.01.029
22. Sharma, R.; Sircar, P.; Pachori, R. B.; Bhandary, S. V.; Acharya, U. R. *J. Mech. Med. Biol.* **2019,** *19,* No. 1940011. doi:10.1142/s0219519419400116
23. Chan, E. W.; Eldeeb, M.; Sun, V.; Thomas, D.; Omar, A.; Kapusta, M. A.; Galic, I. J.; Chen, J. C. *Ophthalmol. Retina* **2019,** *3,* 83–92. doi:10.1016/j.oret.2018.07.008
24. Tan, G. S.; Cheung, N.; Simó, R.; Cheung, G. C. M.; Wong, T. Y. *Lancet Diabetes Endocrinol.* **2017,** *5,* 143–155. doi:10.1016/s2213-8587(16)30052-3
25. Zur, D.; Iglicki, M.; Loewenstein, A. *Ophthalmic Res.* **2019,** *62,* 231–236. doi:10.1159/000499540
26. Whitcher, J. P.; Srinivasan, M.; Upadhyay, M. P. *Bull. W. H. O.* **2001,** *79,* 214–221.
27. Yang, X.; Chen, H.; Zhang, T.; Yin, X.; Man, J.; He, Q.; Lu, M. *Aging* **2021,** *13,* 19614–19642. doi:10.18632/aging.203374
28. Kang-Mieler, J. J.; Rudeen, K. M.; Liu, W.; Mieler, W. F. *Eye (London, U. K.)* **2020,** *34,* 1371–1379. doi:10.1038/s41433-020-0809-0
29. Cometto-Muñiz, J. E.; Cain, W. S.; Hudnell, H. K. *Percept. Psychophysics* **1997,** *59,* 665–674. doi:10.3758/bf03206014
30. Debbasch, C.; Ebenhahn, C.; Dami, N.; Pericoi, M.; Van den Berghe, C.; Cottin, M.; Nohynek, G. J. *Food Chem. Toxicol.* **2005,** *43,* 155–165. doi:10.1016/j.fct.2004.09.004
31. Addo, E.; Bamiro, O. A.; Siwale, R. Anatomy of the Eye and Common Diseases Affecting the Eye. In *Ocular Drug Delivery: Advances, Challenges and Applications;* Addo, R. T., Ed.; Springer International Publishing: Cham, 2016; pp 11–25. doi:10.1007/978-3-319-47691-9_2
32. Chinnery, H. R.; McMenamin, P. G.; Dando, S. J. *Pfluegers Arch.* **2017,** *469,* 501–515. doi:10.1007/s00424-017-1947-5
33. Wróblewska, K. B.; Milanowski, B.; Kucińska, M.; Plewa, S.; Długaszewska, J.; Muszalska-Kolos, I. *Pharmaceuticals* **2021,** *14,* 849. doi:10.3390/ph14090849
34. Kim, S. J.; Flach, A. J.; Jampol, L. M. *Surv. Ophthalmol.* **2010,** *55,* 108–133. doi:10.1016/j.survophthal.2009.07.005
35. Nieminen, T.; Lehtimäki, T.; Mäenpää, J.; Ropo, A.; Uusitalo, H.; Kähönen, M. *Scand. J. Clin. Lab. Invest.* **2007,** *67,* 237–245. doi:10.1080/00365510601034736
36. Sponsel, W. E.; Paris, G.; Trigo, Y.; Pena, M.; Weber, A.; Sanford, K.; Mckinnon, S. *Am. J. Ophthalmol.* **2002,** *133,* 11–18. doi:10.1016/s0002-9394(01)01286-7
37. Gaudana, R.; Ananthula, H. K.; Parenky, A.; Mitra, A. K. *AAPS J.* **2010,** *12,* 348–360. doi:10.1208/s12248-010-9183-3
38. Gorantla, S.; Krishna Rapalli, V.; Waghule, T.; Prakash Singh, P.; Kumar Dubey, S.; Saha, R. N.; Singhvi, G. *RSC Adv.* **2020,** *10,* 27835–27855. doi:10.1039/d0ra04971a
39. Ehlers, N.; Hjortdal, J. *Exp. Eye Res.* **2004,** *78,* 543–548. doi:10.1016/j.exer.2003.09.017
40. Li, Y.; Tan, O.; Brass, R.; Weiss, J. L.; Huang, D. *Ophthalmology* **2012,** *119,* 2425–2433. doi:10.1016/j.ophtha.2012.06.023
41. Norman, R. E.; Flanagan, J. G.; Rausch, S. M. K.; Sigal, I. A.; Tertinegg, I.; Eilaghi, A.; Portnoy, S.; Sled, J. G.; Ethier, C. R. *Exp. Eye Res.* **2010,** *90,* 277–284. doi:10.1016/j.exer.2009.11.001
42. Bachu, R. D.; Chowdhury, P.; Al-Saedi, Z. H. F.; Karla, P. K.; Boddu, S. H. S. *Pharmaceutics* **2018,** *10,* 28. doi:10.3390/pharmaceutics10010028
43. Wróblewska, K. B.; Jadach, B.; Muszalska-Kolos, I. *Int. J. Pharm.* **2021,** *607,* 121012. doi:10.1016/j.ijpharm.2021.121012
44. Cabrera, F. J.; Wang, D. C.; Reddy, K.; Acharya, G.; Shin, C. S. *Drug Discovery Today* **2019,** *24,* 1679–1684. doi:10.1016/j.drudis.2019.05.035
45. Saraswathy, K.; Agarwal, G.; Srivastava, A. *J. Appl. Polym. Sci.* **2020,** *137,* 49285. doi:10.1002/app.49285
46. Stjernschantz, J.; Astin, M. Anatomy and Physiology of the Eye. Physiological Aspects of Ocular Drug Therapy. *Biopharmaceutics of Ocular Drug Delivery;* CRC Press, 1983.
47. Gote, V.; Sikder, S.; Sicotte, J.; Pal, D. *J. Pharmacol. Exp. Ther.* **2019,** *370,* 602–624. doi:10.1124/jpet.119.256933
48. Souto, E. B.; Dias-Ferreira, J.; López-Machado, A.; Ettcheto, M.; Cano, A.; Camins Espuny, A.; Espina, M.; Garcia, M. L.; Sánchez-López, E. *Pharmaceutics* **2019,** *11,* 460. doi:10.3390/pharmaceutics11090460
49. Jumelle, C.; Gholizadeh, S.; Annabi, N.; Dana, R. *J. Controlled Release* **2020,** *321,* 1–22. doi:10.1016/j.jconrel.2020.01.057
50. López-Machado, A.; Díaz, N.; Cano, A.; Espina, M.; Badía, J.; Baldomà, L.; Calpena, A. C.; Biancardi, M.; Souto, E. B.; García, M. L.; Sánchez-López, E. *Int. J. Pharm.* **2021,** *609,* 121188. doi:10.1016/j.ijpharm.2021.121188
51. Yadav, M.; Schiavone, N.; Guzman-Aranguez, A.; Giansanti, F.; Papucci, L.; Perez de Lara, M. J.; Singh, M.; Kaur, I. P. *Drug Delivery Transl. Res.* **2020,** *10,* 919–944. doi:10.1007/s13346-020-00733-4
52. Benaim, D.; Tétart, F.; Bauvin, O.; Delcampe, A.; Joly, P.; Muraine, M.; Gueudry, J. *J. Fr. Ophtalmol.* **2019,** *42,* e147–e151. doi:10.1016/j.jfo.2019.02.003
53. Heikal, M. A.; Soliman, T. T.; Abousaif, W. S.; Shebl, A. A. *Graefe's Arch. Clin. Exp. Ophthalmol.* **2022,** *260,* 353–361. doi:10.1007/s00417-021-05356-0
54. Al-Kinani, A. A.; Zidan, G.; Elsaid, N.; Seyfoddin, A.; Alani, A. W. G.; Alany, R. G. *Adv. Drug Delivery Rev.* **2018,** *126,* 113–126. doi:10.1016/j.addr.2017.12.017
55. Krtalić, I.; Radošević, S.; Hafner, A.; Grassi, M.; Nenadić, M.; Cetina-Čižmek, B.; Filipović-Grčić, J.; Pepić, I.; Lovrić, J. *J. Pharm. Sci.* **2018,** *107,* 1562–1571. doi:10.1016/j.xphs.2018.01.019
56. McDonald, M. B.; Protzko, E. E.; Brunner, L. S.; Morris, T. W.; Haas, W.; Paterno, M. R.; Comstock, T. L.; Usner, D. W. *Ophthalmology* **2009,** *116,* 1615–1623. doi:10.1016/j.ophtha.2009.05.014

57. Verin, P.; Allewaert, R.; Joyaux, J. C.; Piozzi, E.; Koliopoulos, J.; Bloch-Michel, E. *Eur. J. Ophthalmol.* **2001,** *11,* 120–125. doi:10.1177/112067210101100203
58. Maulvi, F. A.; Shetty, K. H.; Desai, D. T.; Shah, D. O.; Willcox, M. D. P. *Int. J. Pharm.* **2021,** *608,* 121105. doi:10.1016/j.ijpharm.2021.121105
59. Shastri, D.; Shelat, P.; Shukla, A.; Patel, P. *Syst. Rev. Pharm.* **2010,** *1,* 113. doi:10.4103/0975-8453.75042
60. Chang, M.-C.; Luo, T.-Y.; Huang, C.-Y.; Peng, C.-L.; Chen, K.-Y.; Yeh, L.-K. *Biomed. Phys. Eng. Express* **2020,** *6,* 045017. doi:10.1088/2057-1976/ab97a2
61. López-Cano, J. J.; González-Cela-Casamayor, M. A.; Andrés-Guerrero, V.; Herrero-Vanrell, R.; Molina-Martínez, I. T. *Expert Opin. Drug Delivery* **2021,** *18,* 819–847. doi:10.1080/17425247.2021.1872542
62. Sai, N.; Dong, X.; Huang, P.; You, L.; Yang, C.; Liu, Y.; Wang, W.; Wu, H.; Yu, Y.; Du, Y.; Leng, X.; Yin, X.; Qu, C.; Ni, J. *Molecules* **2020,** *25,* 81. doi:10.3390/molecules25010081
63. Ding, D.; Kundukad, B.; Somasundar, A.; Vijayan, S.; Khan, S. A.; Doyle, P. S. *ACS Appl. Bio Mater.* **2018,** *1,* 561–571. doi:10.1021/acsabm.8b00041
64. Elsaid, N.; Jackson, T. L.; Elsaid, Z.; Alqathama, A.; Somavarapu, S. *Mol. Pharmaceutics* **2016,** *13,* 2923–2940. doi:10.1021/acs.molpharmaceut.6b00335
65. Korhonen, E.; Rönkkö, S.; Hillebrand, S.; Riikonen, J.; Xu, W.; Järvinen, K.; Lehto, V.-P.; Kauppinen, A. *Eur. J. Pharm. Biopharm.* **2016,** *100,* 1–8. doi:10.1016/j.ejpb.2015.11.020
66. Otake, H.; Goto, R.; Ogata, F.; Isaka, T.; Kawasaki, N.; Kobayakawa, S.; Matsunaga, T.; Nagai, N. *Int. J. Nanomed.* **2021,** *16,* 5343–5356. doi:10.2147/ijn.s317046
67. Xin, G.; Zhang, M.; Zhong, Z.; Tang, L.; Feng, Y.; Wei, Z.; Li, S.; Li, Y.; Zhang, J.; Zhang, B.; Zhang, M.; Rowell, N.; Chen, Z.; Niu, H.; Yu, K.; Huang, W. *ACS Appl. Mater. Interfaces* **2020,** *12,* 57710–57720. doi:10.1021/acsami.0c17296
68. Gao, Y. *Chin. Pharm. J.* **2019,** *54,* 390–399.
69. Rashid, M. A.; Naz, T.; Abbas, M.; Nazir, S.; Younas, N.; Majeed, S.; Qureshi, N.; Akhtar, M. N. *Colloid Interface Sci. Commun.* **2019,** *28,* 41–48. doi:10.1016/j.colcom.2018.11.006
70. Choradiya, B. R.; Patil, S. B. *J. Mol. Liq.* **2021,** *339,* 116751. doi:10.1016/j.molliq.2021.116751
71. Shah, J.; Nair, A. B.; Jacob, S.; Patel, R. K.; Shah, H.; Shehata, T. M.; Morsy, M. A. *Pharmaceutics* **2019,** *11,* 230. doi:10.3390/pharmaceutics11050230
72. Grumezescu, A. M. *Nanoscale Fabrication, Optimization, Scale-up and Biological Aspects of Pharmaceutical Nanotechnology;* William Andrew, 2017.
73. Kim, N. J.; Harris, A.; Elghouche, A.; Gama, W.; Siesky, B. Ocular Permeation Enhancers. In *Nano-Biomaterials For Ophthalmic Drug Delivery;* Pathak, Y.; Sutariya, V.; Hirani, A. A., Eds.; Springer International Publishing: Cham, 2016; pp 177–209. doi:10.1007/978-3-319-29346-2_9
74. Zheng, C.; Li, M.; Ding, J. *BIO Integr.* **2021,** *2,* 57–60. doi:10.15212/bioi-2021-0016
75. El-Emam, G. A.; Girgis, G. N. S.; El-Sokkary, M. M. A.; El-Azeem Soliman, O. A.; Abd El Gawad, A. E. G. H. *Int. J. Nanomed.* **2020,** *15,* 7825–7840. doi:10.2147/ijn.s268208
76. Saettone, M. F.; Salminen, L. *Adv. Drug Delivery Rev.* **1995,** *16,* 95–106. doi:10.1016/0169-409x(95)00014-x
77. Di Prima, G.; Licciardi, M.; Carfì Pavia, F.; Lo Monte, A. I.; Cavallaro, G.; Giammona, G. *Int. J. Pharm.* **2019,** *567,* 118459. doi:10.1016/j.ijpharm.2019.118459
78. Polat, H. K.; Bozdağ Pehlivan, S.; Özkul, C.; Çalamak, S.; Öztürk, N.; Aytekin, E.; Fırat, A.; Ulubayram, K.; Kocabeyoğlu, S.; İrkeç, M.; Çalış, S. *Int. J. Pharm.* **2020,** *585,* 119552. doi:10.1016/j.ijpharm.2020.119552
79. Devhadrao, N. V.; Siddhaia, M. *J. Drug Delivery Ther.* **2018,** *8,* 115–121. doi:10.22270/jddt.v8i5-s.1991
80. Jervis, L. P. *J. Bioequivalence Bioavailability* **2016,** *09*. doi:10.4172/jbb.1000318
81. Omer, S.; Zelkó, R. *Pharmaceutics* **2021,** *13,* 1637. doi:10.3390/pharmaceutics13101637
82. Hui, A.; Bajgrowicz-Cieslak, M.; Phan, C.-M.; Jones, L. *Clin. Ophthalmol.* **2017,** *11,* 1657–1665. doi:10.2147/opth.s141404
83. Pulliero, A.; Profumo, A.; Rosano, C.; Izzotti, A.; Saccà, S. C. *Appl. Sci.* **2021,** *11,* 1931. doi:10.3390/app11041931
84. Abdelkader, H.; Wertheim, D.; Pierscionek, B.; Alany, R. G. *Pharmaceutics* **2020,** *12,* 1158. doi:10.3390/pharmaceutics12121158
85. Shukr, M. H. *J. Microencapsulation* **2016,** *33,* 71–79. doi:10.3109/02652048.2015.1128489
86. Mahajan, H. S.; Deshmukh, S. R. *Carbohydr. Polym.* **2015,** *122,* 243–247. doi:10.1016/j.carbpol.2015.01.018
87. Tighsazzadeh, M.; Mitchell, J. C.; Boateng, J. S. *Int. J. Pharm.* **2019,** *566,* 111–125. doi:10.1016/j.ijpharm.2019.05.059
88. Wafa, H. G.; Essa, E. A.; El-Sisi, A. E.; El Maghraby, G. M. *Drug Delivery Transl. Res.* **2021,** *11,* 1084–1095. doi:10.1007/s13346-020-00825-1
89. Ghasemi Falavarjani, K.; Nguyen, Q. D. *Eye (London, U. K.)* **2013,** *27,* 787–794. doi:10.1038/eye.2013.107
90. Intravitreal Injections: Complications https://www.aao.org/focalpointssnippetdetail.aspx?id=98770d1b-875e-4f4e-8bc6-3bcabcf46ad2 (accessed Jan 7, 2022).
91. Baumal, C. R.; Spaide, R. F.; Vajzovic, L.; Freund, K. B.; Walter, S. D.; John, V.; Rich, R.; Chaudhry, N.; Lakhanpal, R. R.; Oellers, P. R.; Leveque, T. K.; Rutledge, B. K.; Chittum, M.; Bacci, T.; Enriquez, A. B.; Sund, N. J.; Subong, E. N. P.; Albini, T. A. *Ophthalmology* **2020,** *127,* 1345–1359. doi:10.1016/j.ophtha.2020.04.017
92. Chiang, B.; Wang, K.; Ethier, C. R.; Prausnitz, M. R. *Invest. Ophthalmol. Visual Sci.* **2017,** *58,* 545–554. doi:10.1167/iovs.16-20679
93. Chiang, B.; Venugopal, N.; Grossniklaus, H. E.; Jung, J. H.; Edelhauser, H. F.; Prausnitz, M. R. *Invest. Ophthalmol. Visual Sci.* **2017,** *58,* 555–564. doi:10.1167/iovs.16-20377
94. Chiang, B.; Venugopal, N.; Edelhauser, H. F.; Prausnitz, M. R. *Exp. Eye Res.* **2016,** *153,* 101–109. doi:10.1016/j.exer.2016.10.011
95. Gonenc, B.; Chae, J.; Gehlbach, P.; Taylor, R. H.; Iordachita, I. *Sensors* **2017,** *17,* 2195. doi:10.3390/s17102195
96. Prausnitz, M. R.; Jiang, N.; Edelhauser, H. F. Method for Drug Delivery to Ocular Tissue Using Microneedle. WO2007131050A3, Feb 14, 2008.
97. Prausnitz, M. R.; Jiang, J.; Patel, S. R.; Gill, H. S.; Ghate, D.; McCarey, B. E.; Geroski, D. H.; Edelhauser, H. F. *Invest. Ophthalmol. Visual Sci.* **2007,** *48,* 3191.
98. Thakur Singh, R. R.; Tekko, I.; McAvoy, K.; McMillan, H.; Jones, D.; Donnelly, R. F. *Expert Opin. Drug Delivery* **2017,** *14,* 525–537. doi:10.1080/17425247.2016.1218460
99. Hartman, R. R.; Kompella, U. B. *J. Ocul. Pharmacol. Ther.* **2018,** *34,* 141–153. doi:10.1089/jop.2017.0121

100. Jung, J. H.; Chiang, B.; Grossniklaus, H. E.; Prausnitz, M. R. *J. Controlled Release* **2018,** *277,* 14–22. doi:10.1016/j.jconrel.2018.03.001
101. Jeong, H.-R.; Lee, H.-S.; Choi, I.-J.; Park, J.-H. *J. Drug Targeting* **2017,** *25,* 29–40. doi:10.1080/1061186x.2016.1200589
102. Moussi, K.; Bukhamsin, A.; Hidalgo, T.; Kosel, J. *Adv. Eng. Mater.* **2020,** *22,* 1901358. doi:10.1002/adem.201901358
103. Moffatt, K.; Wang, Y.; Raj Singh, T. R.; Donnelly, R. F. *Curr. Opin. Pharmacol.* **2017,** *36,* 14–21. doi:10.1016/j.coph.2017.07.007
104. Jamaledin, R.; Yiu, C. K. Y.; Zare, E. N.; Niu, L.-N.; Vecchione, R.; Chen, G.; Gu, Z.; Tay, F. R.; Makvandi, P. *Adv. Mater. (Weinheim, Ger.)* **2020,** *32,* 2002129. doi:10.1002/adma.202002129
105. Sabri, A. H. B.; Anjani, Q. K.; Utomo, E.; Ripolin, A.; Donnelly, R. F. *Int. J. Pharm.* **2022,** *617,* 121593. doi:10.1016/j.ijpharm.2022.121593
106. Zan, P.; Than, A.; Duong, P. K.; Song, J.; Xu, C.; Chen, P. *Adv. Ther.* **2019,** *2,* 1900064. doi:10.1002/adtp.201900064
107. Amodwala, S.; Kumar, P.; Thakkar, H. P. *Eur. J. Pharm. Sci.* **2017,** *104,* 114–123. doi:10.1016/j.ejps.2017.04.001
108. Pineda-Álvarez, R. A.; Bernad-Bernad, M. J.; Rodríguez-Cruz, I. M.; Escobar-Chávez, J. J. *J. Pharm. Innovation* **2022,** *17,* 71–84. doi:10.1007/s12247-020-09494-6
109. Castañeda, P. S.; Escobar-Chávez, J. J.; Vázquez, J. A.; Cruz, I. M. R.; Contreras, L. M. M. *Iran. J. Pharm. Res.* **2020,** *19,* 127–133. doi:10.22037/ijpr.2019.1100914
110. Martanto, W.; Davis, S. P.; Holiday, N. R.; Wang, J.; Gill, H. S.; Prausnitz, M. R. *Pharm. Res.* **2004,** *21,* 947–952. doi:10.1023/b:pham.0000029282.44140.2e
111. Koh, K. J.; Liu, Y.; Lim, S. H.; Loh, X. J.; Kang, L.; Lim, C. Y.; Phua, K. K. L. *Sci. Rep.* **2018,** *8,* 11842. doi:10.1038/s41598-018-30290-3
112. Saurer, E. M.; Flessner, R. M.; Sullivan, S. P.; Prausnitz, M. R.; Lynn, D. M. *Biomacromolecules* **2010,** *11,* 3136–3143. doi:10.1021/bm1009443
113. Hassan, J.; Haigh, C.; Ahmed, T.; Uddin, M. J.; Das, D. B. *Pharmaceutics* **2022,** *14,* 1066. doi:10.3390/pharmaceutics14051066
114. Kim, Y.-C.; Park, J.-H.; Prausnitz, M. R. *Adv. Drug Delivery Rev.* **2012,** *64,* 1547–1568. doi:10.1016/j.addr.2012.04.005
115. Li, J.; Zeng, M.; Shan, H.; Tong, C. *Curr. Med. Chem.* **2017,** *24,* 2413–2422. doi:10.2174/0929867324666170526124053
116. Rodgers, A. M.; Cordeiro, A. S.; Donnelly, R. F. *Med. Devices: Evidence Res.* **2019,** *12,* 379–398. doi:10.2147/mder.s198220
117. Bhatnagar, S.; Gadeela, P. R.; Thathireddy, P.; Venuganti, V. V. K. *J. Chem. Sci.* **2019,** *131,* 90. doi:10.1007/s12039-019-1666-x
118. Nagarkar, R.; Singh, M.; Nguyen, H. X.; Jonnalagadda, S. *J. Drug Delivery Sci. Technol.* **2020,** *59,* 101923. doi:10.1016/j.jddst.2020.101923
119. Vinayakumar, K. B.; Kulkarni, P. G.; Nayak, M. M.; Dinesh, N. S.; Hegde, G. M.; Ramachandra, S. G.; Rajanna, K. *J. Micromech. Microeng.* **2016,** *26,* 065013. doi:10.1088/0960-1317/26/6/065013
120. Li, J.; Liu, B.; Zhou, Y.; Chen, Z.; Jiang, L.; Yuan, W.; Liang, L. *PLoS One* **2017,** *12,* e0172043. doi:10.1371/journal.pone.0172043
121. de Groot, A. M.; Platteel, A. C. M.; Kuijt, N.; van Kooten, P. J. S.; Vos, P. J.; Sijts, A. J. A. M.; van der Maaden, K. *Front. Immunol.* **2017,** *8,* 10.3389/fimmu.2017.01789. doi:10.3389/fimmu.2017.01789
122. Chen, W.; Wang, C.; Yan, L.; Huang, L.; Zhu, X.; Chen, B.; Sant, H. J.; Niu, X.; Zhu, G.; Yu, K. N.; Roy, V. A. L.; Gale, B. K.; Chen, X. *J. Mater. Chem. B* **2014,** *2,* 1699–1705. doi:10.1039/c3tb21698e
123. Nguyen, H. X.; Bozorg, B. D.; Kim, Y.; Wieber, A.; Birk, G.; Lubda, D.; Banga, A. K. *Eur. J. Pharm. Biopharm.* **2018,** *129,* 88–103. doi:10.1016/j.ejpb.2018.05.017
124. Choi, S.-O.; Kim, Y. C.; Park, J.-H.; Hutcheson, J.; Gill, H. S.; Yoon, Y.-K.; Prausnitz, M. R.; Allen, M. G. *Biomed. Microdevices* **2010,** *12,* 263–273. doi:10.1007/s10544-009-9381-x
125. Kusama, S.; Sato, K.; Matsui, Y.; Kimura, N.; Abe, H.; Yoshida, S.; Nishizawa, M. *Nat. Commun.* **2021,** *12,* 658. doi:10.1038/s41467-021-20948-4
126. Lee, K.; Lee, C. Y.; Jung, H. *Biomaterials* **2011,** *32,* 3134–3140. doi:10.1016/j.biomaterials.2011.01.014
127. Tian, Y.; Lee, J.; van der Maaden, K.; Bhide, Y.; de Vries-Idema, J. J.; Akkerman, R.; O'Mahony, C.; Jiskoot, W.; Frijlink, H. W.; Huckriede, A. L. W.; Hinrichs, W. L. J.; Bouwstra, J. A.; Beukema, M. *J. Pharm. Sci.* **2022,** *111,* 1070–1080. doi:10.1016/j.xphs.2022.01.033
128. Martin, C. J.; Allender, C. J.; Brain, K. R.; Morrissey, A.; Birchall, J. C. *J. Controlled Release* **2012,** *158,* 93–101. doi:10.1016/j.jconrel.2011.10.024
129. Khosraviboroujeni, A.; Mirdamadian, S. Z.; Minaiyan, M.; Taheri, A. *Drug Delivery Transl. Res.* **2022,** *12,* 1195–1208. doi:10.1007/s13346-021-01006-4
130. Zhang, J.; Wang, Y.; Jin, J. Y.; Degan, S.; Hall, R. P.; Boehm, R. D.; Jaipan, P.; Narayan, R. J. *JOM* **2016,** *68,* 1128–1133. doi:10.1007/s11837-016-1841-1
131. Nguyen, H. X.; Banga, A. K. *Pharm. Res.* **2018,** *35,* 68. doi:10.1007/s11095-018-2369-6
132. Gao, Y.; Hou, M.; Yang, R.; Zhang, L.; Xu, Z.; Kang, Y.; Xue, P. *J. Mater. Chem. B* **2019,** *7,* 7515–7524. doi:10.1039/c9tb01994d
133. Aung, N. N.; Ngawhirunpat, T.; Rojanarata, T.; Patrojanasophon, P.; Pamornpathomkul, B.; Opanasopit, P. *Int. J. Pharm.* **2020,** *586,* 119508. doi:10.1016/j.ijpharm.2020.119508
134. Skaria, E.; Patel, B. A.; Flint, M. S.; Ng, K. W. *Anal. Chem. (Washington, DC, U. S.)* **2019,** *91,* 4436–4443. doi:10.1021/acs.analchem.8b04980
135. Yu, W.; Jiang, G.; Liu, D.; Li, L.; Chen, H.; Liu, Y.; Huang, Q.; Tong, Z.; Yao, J.; Kong, X. *Mater. Sci. Eng., C* **2017,** *71,* 725–734. doi:10.1016/j.msec.2016.10.063
136. Yu, W.; Jiang, G.; Liu, D.; Li, L.; Tong, Z.; Yao, J.; Kong, X. *Mater. Sci. Eng., C* **2017,** *73,* 425–428. doi:10.1016/j.msec.2016.12.111
137. DeMuth, P. C.; Garcia-Beltran, W. F.; Ai-Ling, M. L.; Hammond, P. T.; Irvine, D. J. *Adv. Funct. Mater.* **2013,** *23,* 161–172. doi:10.1002/adfm.201201512
138. Kang, N.-W.; Kim, S.; Lee, J.-Y.; Kim, K.-T.; Choi, Y.; Oh, Y.; Kim, J.; Kim, D.-D.; Park, J.-H. *Expert Opin. Drug Delivery* **2021,** *18,* 929–947. doi:10.1080/17425247.2021.1828860
139. Larrañeta, E.; Lutton, R. E. M.; Woolfson, A. D.; Donnelly, R. F. *Mater. Sci. Eng., R* **2016,** *104,* 1–32. doi:10.1016/j.mser.2016.03.001
140. Wei-Ze, L.; Mei-Rong, H.; Jian-Ping, Z.; Yong-Qiang, Z.; Bao-Hua, H.; Ting, L.; Yong, Z. *Int. J. Pharm.* **2010,** *389,* 122–129. doi:10.1016/j.ijpharm.2010.01.024
141. Waghule, T.; Singhvi, G.; Dubey, S. K.; Pandey, M. M.; Gupta, G.; Singh, M.; Dua, K. *Biomed. Pharmacother.* **2019,** *109,* 1249–1258. doi:10.1016/j.biopha.2018.10.078

142. Cárcamo-Martínez, Á.; Mallon, B.; Domínguez-Robles, J.; Vora, L. K.; Anjani, Q. K.; Donnelly, R. F. *Int. J. Pharm.* **2021,** *599,* 120455. doi:10.1016/j.ijpharm.2021.120455
143. Ita, K. *Biomed. Pharmacother.* **2017,** *93,* 1116–1127. doi:10.1016/j.biopha.2017.07.019
144. Turner, J. G.; White, L. R.; Estrela, P.; Leese, H. S. *Macromol. Biosci.* **2021,** *21,* 2000307. doi:10.1002/mabi.202000307
145. Eltayib, E.; Brady, A. J.; Caffarel-Salvador, E.; Gonzalez-Vazquez, P.; Zaid Alkilani, A.; McCarthy, H. O.; McElnay, J. C.; Donnelly, R. F. *Eur. J. Pharm. Biopharm.* **2016,** *102,* 123–131. doi:10.1016/j.ejpb.2016.03.009
146. Liu, G.-S.; Kong, Y.; Wang, Y.; Luo, Y.; Fan, X.; Xie, X.; Yang, B.-R.; Wu, M. X. *Biomaterials* **2020,** *232,* 119740. doi:10.1016/j.biomaterials.2019.119740
147. Larrañeta, E.; Lutton, R. E. M.; Brady, A. J.; Vicente-Pérez, E. M.; Woolfson, A. D.; Thakur, R. R. S.; Donnelly, R. F. *Macromol. Mater. Eng.* **2015,** *300,* 586–595. doi:10.1002/mame.201500016
148. Faraji Rad, Z.; Prewett, P. D.; Davies, G. J. *Beilstein J. Nanotechnol.* **2021,** *12,* 1034–1046. doi:10.3762/bjnano.12.77
149. Amarnani, R.; Shende, P. *Biomed. Microdevices* **2022,** *24,* 4. doi:10.1007/s10544-021-00604-w
150. Jung, J. H.; Jin, S. G. *J. Pharm. Invest.* **2021,** *51,* 503–517. doi:10.1007/s40005-021-00512-4
151. Tucak, A.; Sirbubalo, M.; Hindija, L.; Rahić, O.; Hadžiabdić, J.; Muhamedagić, K.; Čekić, A.; Vranić, E. *Micromachines* **2020,** *11,* 961. doi:10.3390/mi11110961
152. Krieger, K. J.; Bertollo, N.; Dangol, M.; Sheridan, J. T.; Lowery, M. M.; O'Cearbhaill, E. D. *Microsyst. Nanoeng.* **2019,** *5,* 42. doi:10.1038/s41378-019-0088-8
153. Serbin, J.; Egbert, A.; Ostendorf, A.; Chichkov, B. N.; Houbertz, R.; Domann, G.; Schulz, J.; Cronauer, C.; Fröhlich, L.; Popall, M. *Opt. Lett.* **2003,** *28,* 301–303. doi:10.1364/ol.28.000301
154. Indermun, S.; Luttge, R.; Choonara, Y. E.; Kumar, P.; du Toit, L. C.; Modi, G.; Pillay, V. *J. Controlled Release* **2014,** *185,* 130–138. doi:10.1016/j.jconrel.2014.04.052
155. Kim, J. D.; Kim, M.; Yang, H.; Lee, K.; Jung, H. *J. Controlled Release* **2013,** *170,* 430–436. doi:10.1016/j.jconrel.2013.05.026
156. Dharadhar, S.; Majumdar, A.; Dhoble, S.; Patravale, V. *Drug Dev. Ind. Pharm.* **2019,** *45,* 188–201. doi:10.1080/03639045.2018.1539497
157. McCrudden, M. T. C.; Alkilani, A. Z.; McCrudden, C. M.; McAlister, E.; McCarthy, H. O.; Woolfson, A. D.; Donnelly, R. F. *J. Controlled Release* **2014,** *180,* 71–80. doi:10.1016/j.jconrel.2014.02.007
158. Bhatnagar, S.; Saju, A.; Cheerla, K. D.; Gade, S. K.; Garg, P.; Venuganti, V. V. K. *Drug Delivery Transl. Res.* **2018,** *8,* 473–483. doi:10.1007/s13346-017-0470-8
159. Palakurthi, N. K.; Correa, Z. M.; Augsburger, J. J.; Banerjee, R. K. *J. Ocul. Pharmacol. Ther.* **2011,** *27,* 151–156. doi:10.1089/jop.2010.0037
160. Roy, G.; Galigama, R. D.; Thorat, V. S.; Garg, P.; Venuganti, V. V. K. *Drug Dev. Ind. Pharm.* **2020,** *46,* 1114–1122. doi:10.1080/03639045.2020.1776317
161. Ita, K. *J. Drug Delivery Sci. Technol.* **2018,** *44,* 314–322. doi:10.1016/j.jddst.2018.01.004
162. Mönkäre, J.; Reza Nejadnik, M.; Baccouche, K.; Romeijn, S.; Jiskoot, W.; Bouwstra, J. A. *J. Controlled Release* **2015,** *218,* 53–62. doi:10.1016/j.jconrel.2015.10.002
163. Sullivan, S. P.; Murthy, N.; Prausnitz, M. R. *Adv. Mater. (Weinheim, Ger.)* **2008,** *20,* 933–938. doi:10.1002/adma.200701205
164. Sadeqi, A.; Kiaee, G.; Zeng, W.; Rezaei Nejad, H.; Sonkusale, S. *Sci. Rep.* **2022,** *12,* 1853. doi:10.1038/s41598-022-05912-6
165. Qiu, Y.; Li, C.; Zhang, S.; Yang, G.; He, M.; Gao, Y. *Int. J. Pharm.* **2016,** *508,* 1–9. doi:10.1016/j.ijpharm.2016.05.006
166. Yadav, V.; Sharma, P. K.; Murty, U. S.; Mohan, N. H.; Thomas, R.; Dwivedy, S. K.; Banerjee, S. *Int. J. Pharm.* **2021,** *605,* 120815. doi:10.1016/j.ijpharm.2021.120815
167. Bolton, C. J. W.; Howells, O.; Blayney, G. J.; Eng, P. F.; Birchall, J. C.; Gualeni, B.; Roberts, K.; Ashraf, H.; Guy, O. J. *Lab Chip* **2020,** *20,* 2788–2795. doi:10.1039/d0lc00567c
168. Papich, M. G.; Narayan, R. J. *Drug Delivery Transl. Res.* **2022,** *12,* 376–383. doi:10.1007/s13346-021-01096-0
169. Economidou, S. N.; Uddin, M. J.; Marques, M. J.; Douroumis, D.; Sow, W. T.; Li, H.; Reid, A.; Windmill, J. F. C.; Podoleanu, A. *Addit. Manuf.* **2021,** *38,* 101815. doi:10.1016/j.addma.2020.101815
170. Burton, S. A.; Ng, C.-Y.; Simmers, R.; Moeckly, C.; Brandwein, D.; Gilbert, T.; Johnson, N.; Brown, K.; Alston, T.; Prochnow, G.; Siebenaler, K.; Hansen, K. *Pharm. Res.* **2011,** *28,* 31–40. doi:10.1007/s11095-010-0177-8
171. Haj-Ahmad, R.; Khan, H.; Arshad, M. S.; Rasekh, M.; Hussain, A.; Walsh, S.; Li, X.; Chang, M.-W.; Ahmad, Z. *Pharmaceutics* **2015,** *7,* 486–502. doi:10.3390/pharmaceutics7040486
172. Ingrole, R. S. J.; Gill, H. S. *J. Pharmacol. Exp. Ther.* **2019,** *370,* 555–569. doi:10.1124/jpet.119.258707
173. Tarbox, T. N.; Watts, A. B.; Cui, Z.; Williams, R. O., III. *Drug Delivery Transl. Res.* **2018,** *8,* 1828–1843. doi:10.1007/s13346-017-0466-4
174. Huang, D.; Chen, Y.-S.; Rupenthal, I. D. *Adv. Drug Delivery Rev.* **2018,** *126,* 96–112. doi:10.1016/j.addr.2017.09.008
175. Roy, G.; Garg, P.; Venuganti, V. V. K. *Int. J. Pharm.* **2022,** *612,* 121305. doi:10.1016/j.ijpharm.2021.121305
176. Albadr, A. A.; Tekko, I. A.; Vora, L. K.; Ali, A. A.; Laverty, G.; Donnelly, R. F.; Thakur, R. R. S. *Drug Delivery Transl. Res.* **2022,** *12,* 931–943. doi:10.1007/s13346-021-01032-2
177. Shi, H.; Zhou, J.; Wang, Y.; Zhu, Y.; Lin, D.; Lei, L.; Vakal, S.; Wang, J.; Li, X. *Small* **2022,** *18,* 2104657. doi:10.1002/smll.202104657
178. Amer, M.; Chen, R. K. *ASME J. Eng. Sci. Med. Diagn. Ther.* **2020,** *3*. doi:10.1115/1.4048481
179. Amer, M.; Ni, X.; Xian, M.; Chen, R. K. *ASME J. Eng. Sci. Med. Diagn. Ther.* **2021,** *5,* No. 011001. doi:10.1115/1.4052627
180. Suriyaamporn, P.; Opanasopit, P.; Ngawhirunpat, T.; Rangsimawong, W. *J. Drug Delivery Sci. Technol.* **2021,** *61,* 102319. doi:10.1016/j.jddst.2020.102319
181. Li, M.-s.; Yu, X.; Jin, Y.-g.; Wu, Z.-h. *Acta Pharm. Sin.* **2021,** 849–854.
182. Wu, Y.; Vora, L. K.; Wang, Y.; Adrianto, M. F.; Tekko, I. A.; Waite, D.; Donnelly, R. F.; Thakur, R. R. S. *Eur. J. Pharm. Biopharm.* **2021,** *165,* 306–318. doi:10.1016/j.ejpb.2021.05.022
183. Lee, K.; Song, H. B.; Cho, W.; Kim, J. H.; Kim, J. H.; Ryu, W. *Acta Biomater.* **2018,** *80,* 48–57. doi:10.1016/j.actbio.2018.09.039
184. Lee, Y.; Park, S.; Kim, S. I.; Lee, K.; Ryu, W. *Adv. Mater. Technol. (Weinheim, Ger.)* **2020,** *5,* 1901145. doi:10.1002/admt.201901145
185. Than, A.; Liu, C.; Chang, H.; Duong, P. K.; Cheung, C. M. G.; Xu, C.; Wang, X.; Chen, P. *Nat. Commun.* **2018,** *9,* 4433. doi:10.1038/s41467-018-06981-w

186. Shelley, H.; Annaji, M.; Grant, M.; Fasina, O.; Babu, R. J. *J. Ocul. Pharmacol. Ther.* **2022,** *38,* 449–458. doi:10.1089/jop.2021.0089
187. Datta, D.; Roy, G.; Garg, P.; Venuganti, V. V. K. *J. Drug Delivery Sci. Technol.* **2022,** *70,* 103211. doi:10.1016/j.jddst.2022.103211
188. Achouri, D.; Alhanout, K.; Piccerelle, P.; Andrieu, V. *Drug Dev. Ind. Pharm.* **2013,** *39,* 1599–1617. doi:10.3109/03639045.2012.736515
189. Panda, A.; Matadh, V. A.; Suresh, S.; Shivakumar, H. N.; Murthy, S. N. *Drug Delivery Transl. Res.* **2022,** *12,* 67–78. doi:10.1007/s13346-021-00922-9
190. Clearside Biomedical, Inc. *Open-Label, Safety and Tolerability Study of Suprachoroidal Triamcinolone Acetonide Via Microneedle in Subjects With Non-Infectious Uveitis*; Clinical trial registration results/NCT01789320; https://clinicaltrials.gov/ct2/show/NCT01789320; 2021.
191. Roy, G.; Garg, P.; Venuganti, V. V. K. *Int. J. Pharm.* **2022,** *612,* 121305. doi:10.1016/j.ijpharm.2021.121305

License and Terms

This is an open access article licensed under the terms of the Beilstein-Institut Open Access License Agreement (https://www.beilstein-journals.org/bjnano/terms), which is identical to the Creative Commons Attribution 4.0 International License (https://creativecommons.org/licenses/by/4.0). The reuse of material under this license requires that the author(s), source and license are credited. Third-party material in this article could be subject to other licenses (typically indicated in the credit line), and in this case, users are required to obtain permission from the license holder to reuse the material.

The definitive version of this article is the electronic one which can be found at: https://doi.org/10.3762/bjnano.13.98

BEILSTEIN JOURNAL OF NANOTECHNOLOGY

Industrial perspectives for personalized microneedles

Remmi Danae Baker-Sediako*, Benjamin Richter, Matthias Blaicher, Michael Thiel and Martin Hermatschweiler

Perspective

Open Access

Address:
Nanoscribe Gmbh & Co, Hermann-von-Helmholtz-Platz 6, 76344 Eggenstein-Leopoldshafen, Germany

Email:
Remmi Danae Baker-Sediako* - baker@nanoscribe.com

* Corresponding author

Keywords:
3D printing; microfabrication; microneedles; personalized medicine; transdermal drug delivery; two-photon polymerization

Beilstein J. Nanotechnol. **2023,** *14,* 857–864.
https://doi.org/10.3762/bjnano.14.70

Received: 13 January 2023
Accepted: 02 August 2023
Published: 15 August 2023

This article is part of the thematic issue "Microneedles for vaccination and drug delivery".

Guest Editor: P. D. Prewett



© 2023 Baker-Sediako et al.; licensee Beilstein-Institut.
License and terms: see end of document.

Abstract

Microneedles and, subsequently, microneedle arrays are emerging miniaturized medical devices for painless transdermal drug delivery. New and improved additive manufacturing methods enable novel microneedle designs to be realized for preclinical and clinical trial assessments. However, current literature reviews suggest that industrial manufacturers and researchers have focused their efforts on one-size-fits-all designs for transdermal drug delivery, regardless of patient demographic and injection site. In this perspective article, we briefly review current microneedle designs, microfabrication methods, and industrialization strategies. We also provide an outlook where microneedles may become personalized according to a patient's demographic in order to increase drug delivery efficiency and reduce healing times for patient-centric care.

Introduction

The oldest and most common form of needling stems from tattooing, with the oldest recorded tools dating back over 3600 years [1] and the oldest recovered tattooed body being approximately 5000 years old [2]. However, it was not until the 1840s that Francis Rynd invented the first modern-day (i.e., synthetically fabricated) hypodermic needle [3]. Less than a decade later, hypodermic needles would be incorporated with syringe plungers to create a transdermal drug delivery device [4].

Clinicians rapidly adopted transdermal drug delivery (TDD) devices; however, this technique has drawbacks. The most known drawback to TDD needles is trypanophobia, a fear of needles. Roughly 3.5–20.0% of the general population suffers from trypanophobia to various degrees [5,6]. Additionally, healthcare workers are continuously at risk for sharps-related injuries, and hollow-bore needles account for 56% of all sharps injuries [7]. An estimated two million hospital-based workers suffer from work-related needle injuries, adding burdensome financial cost and infection risks to healthcare systems [8,9].

With the advent of advanced additive manufacturing techniques, we can miniaturize needles (microneedles) to overcome

challenges with trypanophobia and hospital-based needle injuries. Today's needles penetrate the deepest parts of the dermis, where discomfort or pain may occur [10]; however, today, we know that the stratum corneum is the only dermal layer clinicians need to penetrate to deliver non-intravenous medicine effectively [5,10-12]. To penetrate the stratum corneum, the length of a needle only needs to be of the order of tens to hundreds of micrometers, which gives rise to their name, microneedles.

Perspective

According to current literature, TDD microneedles have relatively simple shapes, packing orders, and similar aspect ratios. A typical microneedle is either conical or pyramidal with a base of 100–300 μm, heights ranging from 600 to 1000 μm, and a base-to-base spacing between 100 and 500 μm (Figure 1). These simple geometries are advantageous for commercialization because the molds can be micromachined or etched and then used for mass production. One of the most common examples of commercialized TDD microneedles are over-the-counter anti-aging eye patches. Anti-aging eye patches consisting of 200–2000 dissolvable conical microneedles. These dissolvable microneedles are typically a variant of crosslinked hydrogels infused with hyaluronic acid, salicylic acid, caffeine, various vitamins (B3, C, and E), and a blend of various peptides.

Beyond cosmetic applications, microneedle patches are also being investigated for vaccine delivery. The most notable example of vaccine-loaded microneedles comes from the Australian company Vaxxas. Pty. Ltd. Vaxxas has developed a non-dissolving microneedle patch, called the Nanopatch [13-15]. In the Nanopatch, the microneedles are coated in a dry vaccine powder, and upon insertion, the microneedles leave pores in the skin where the powder particles can be bioabsorbed [14,15].

A closer inspection of TDD microneedles for cosmetic and medical applications reveals a lack of diversity when assessing their effectiveness. Namely, studies consist of small populations with participants of similar sex, age, body mass index, and ethnic background. For TDD via microneedles, it is crucial to consider that structural skin properties (e.g., transepidermal water loss, skin elasticity, dermal layer thicknesses, and ceramide content) differ among these groups [16-18], or else results give an incomplete picture. Several studies have also reported that the various demographic groups (e.g., ethnicity and age) heal at different rates [16,19]. Therefore, it is also critical to consider differences in skin penetration, drug absorption, and healing processes among different populations when assessing the effectiveness of drug-delivering microneedles.

In today's age of personalized medicine, it is possible to develop optimized microneedles for different populations and injection areas at scale. For example, microneedles are a promising alternative to oral and systemic medications for pain relief [20-22]. Chronic and acute pain can occur anywhere in the body; however, if we divide the body into mobile areas (i.e., joints) and passive areas (e.g., volar forearm), then a one-size-fits-all microneedle design may not satisfy the requirements for both applications [18]. This builds upon previous work from Rougier et al. [23], who demonstrated that drug absorption differs across the body. Their results agree with previous studies demonstrating that microneedles yield different penetrations depending on the injection site [24,25], whereby the closing of residual micropores and the pharmacokinetics may differ [26]. In the context of drug-loaded microneedle patches for joint-pain management, the microneedle patches will experience dynamic loads and may dislodge before delivering drugs. Thus, microneedles need to be engineered to bear the dynamic loads to last for the duration of treatment.

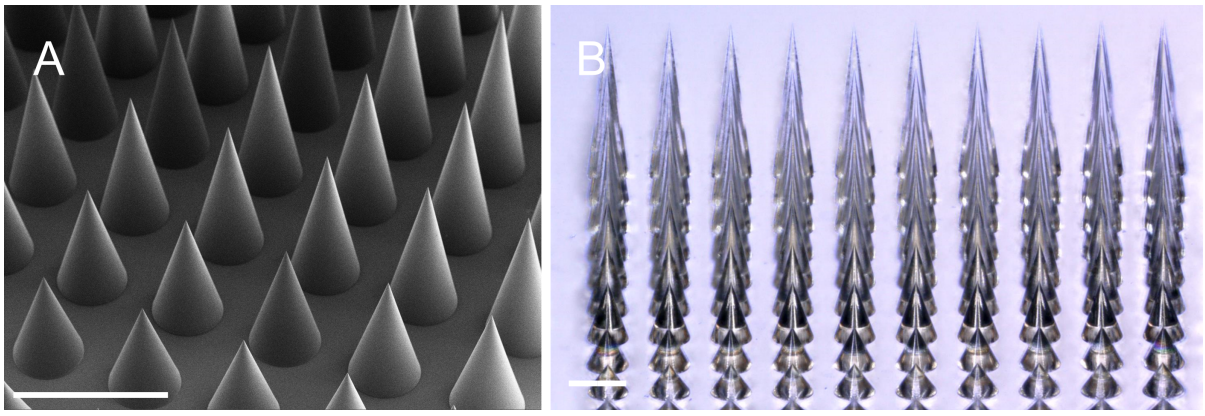


Figure 1: Conical microneedles with varying heights were printed via two-photon polymerization on a "Quantum X shape" lithography system, and the 10 × 10 microneedle array was printed in 130 min. The scale bar is 1 mm in both images. (A) Scanning electron microscopy image of microcones. (B) Optical microscopy image of transparent microcones.

Recent advances in microfabrication readily enable complex microneedle designs that can overcome these challenges [27]. Specifically, light-based 3D printing techniques such as stereolithography (SLA), digital light processing (DLP), and two-photon polymerization (2PP) simplify the rapid prototyping workflow when compared to traditional micro- and nanofabrication methods [28-31] (Figure 2). Thus, the greatest challenge is not fabricating but engineering improved microneedle designs to withstand evolving environments.

Researchers do not need to reinvent the wheel when thinking about new microneedle designs; rather they can adapt what nature has perfected over millennia. For instance, inspiration can come from insects [33,34], especially the approximately 100 species that have developed a preference for human hosts [35]. For example, mosquitos have an approximately 2 mm long proboscis that diverges into six stylets and easily penetrates skin [36,37], and there are several subspecies of mosquitos, such as *Aedes aegypti*, that have evolved to specialize in human hosts [35]. An adapted design would be advantageous for painless transdermal delivery of macromolecules or biological sampling [38]. Adult ticks, as another example, live on their hosts for 7–10 days and can occupy mobile areas, such as the back of the knee, without being disturbed. The strong attachment is possible because the backward-facing teeth lining their proboscis make it extremely difficult to remove, even under dynamic loads. A recent study from Liu et al. demonstrated improved tissue anchoring in barbed microneedles when compared to smooth microneedles [34]. Thus, it would be exciting to design microneedles, particularly those for pain management in joints, that are able to withstand a patient's movements.

Bio-inspired designs do not need to be an exact replica of their animal muse to realize greater efficacy while also maintaining scalability. For example, snake fangs are hollow and asymmetrically grooved teeth optimized to deliver liquid venom. Researchers can use the bio-inspired hollow design to transdermally deliver drugs that must remain in liquid form during administration [39,40] (Figure 3). As with most bio-inspired microneedles, they require miniaturization, shape accuracy, and reproducibility for clinical applications.

As mentioned above, light-based 3D printing (SLA, DLP, and 2PP) are the newest methods for fabricating microneedles. Each method has its own advantages and disadvantages; for brevity, we encourage readers to access previous review papers that cover in depth light-based fabrication techniques [41-43]. SLA and DLP are by far the most common techniques for fabricating microneedles, with approximately eight times as many publications as publications regarding microneedles fabricated via 2PP. We hypothesize that the availability SLA and DLP sytems, the low cost, and the sheer number of systems present at any given institution, are the main driving factors behind the difference in publication quantity. SLA or DLP 3D printers may only cost a few thousand dollars (2500+ USD) when new, but these cost-effective printers are aimed at hobbyists and lack the resolution necessary for microneedle development (Figure 4). Professional SLA or DLP printers are more suitable for

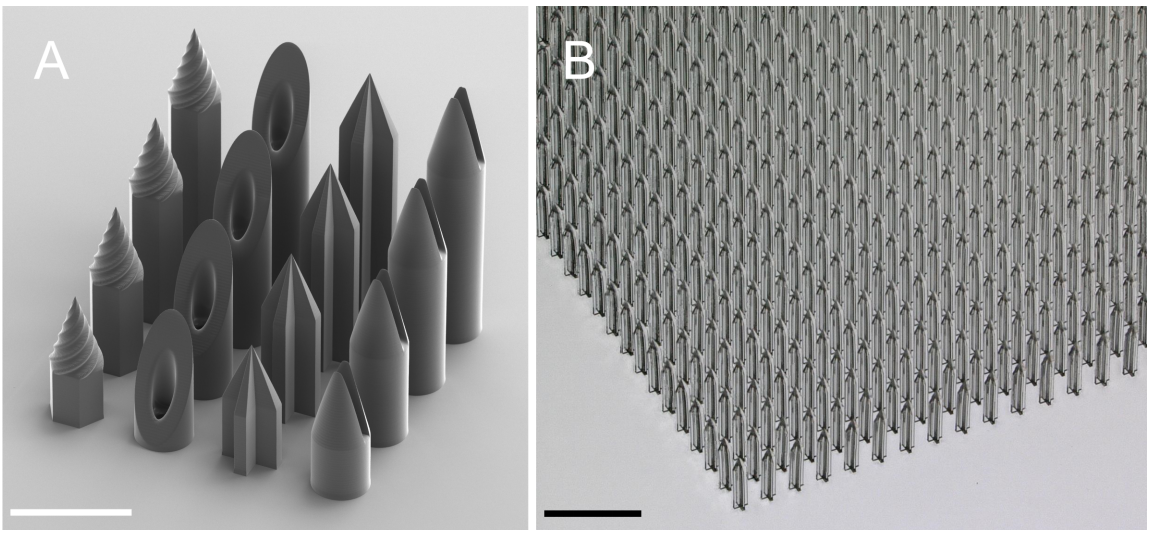


Figure 2: Various solid and hollow microneedle designs printed via two-photon polymerization on a "Quantum X shape" lithography system. (A) Scanning electron microscopy image of a 4 × 4 array consisting of both solid and hollow microneedles. The designs were inspired by Mizuno et al. [32] and Cordeiro et al. [29]. The scale bar is 500 µm. (B) Optical microscopy image of a large 2 cm × 2 cm array with 1746 individual microneedles. The microneedles are 1200 µm tall, 250 µm wide at the base, and spaced 500 µm apart. The large microneedle array was printed in 18 h. The scale bar is 1 mm.

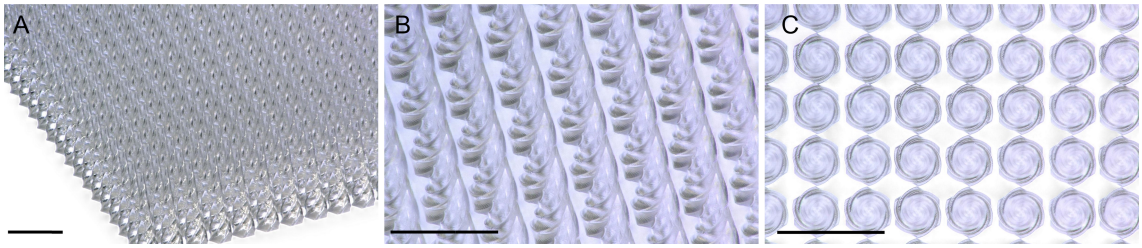


Figure 3: Simple twisted microneedles inspired by snake fangs and Bae et al. [39]. The microneedle array was printed via two-photon polymerization on a "Quantum X shape" lithography system. All scale bars are 500 µm. (A) Zoomed-out image of the microneedle array. (B) Closer inspection of optically transparent twisted microneedles. (c) Top-down view of the twisted microneedle array.

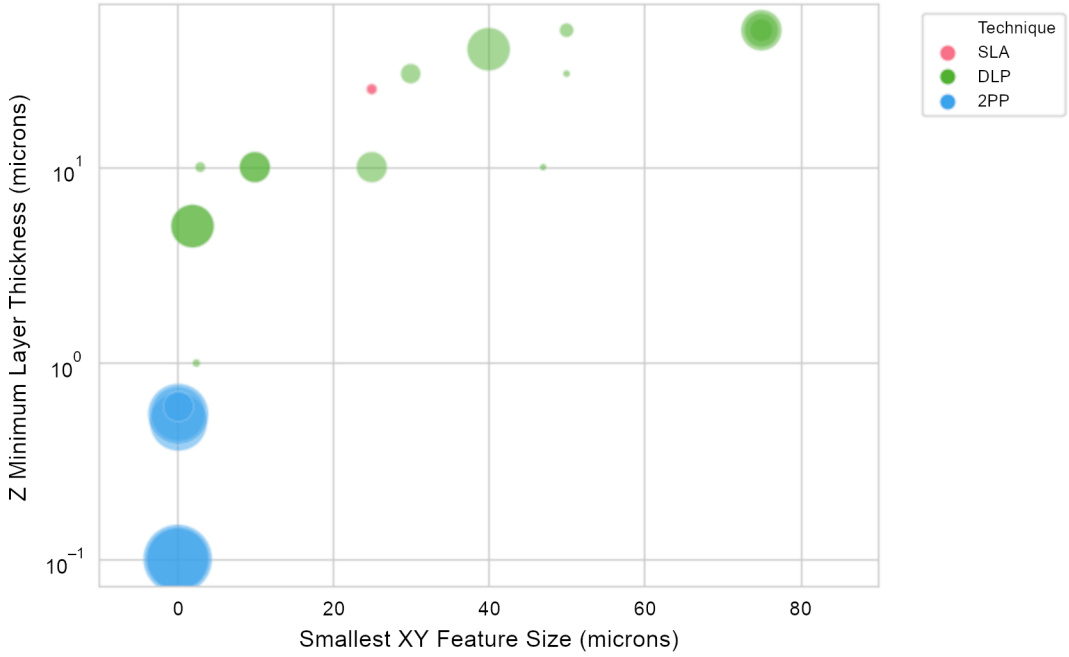


Figure 4: A graphical plot comparing the light-based printing microfabrication techniques SLA, DLP, and 2PP. This relationship plot compares the smallest feature sizes in the *XY* plane and the *Z* axis of commercial instruments. The bubble size represents the approximate cost of the instrument. We see a trend that when small feature sizes of the order of micrometers need to be obtained, the cost of the instrument substantially increases.

microneedle development because they can achieve feature sizes of the order of a few micrometers; however, these professional systems can cost upwards of 250,000+ USD.

The financial differences for acquiring a commercial 2PP system are not so different from those regarding professional-grade DLP or SLA printers. On average, a commercial 2PP instrument may cost a few hundred thousand dollars (400,000+ USD) for a single device (Figure 4). Custom-built 2PP systems are also an option; these are custom systems either retrofitted onto an existing microscope [44] or developed on optical tables [45,46] in the lab to keep the cost low. Commercial retrofits (e.g., positioning stages or electronics) can add up to 50,000+ USD, and this price does not include the femtosecond laser or anti-vibration systems. Custom-built 2PP systems also require extensive optical expertise for the initial installation and are typically a major milestone for several doctoral students. In general, custom-built 2PP systems are constantly evolving instruments to enable one or two particular applications at a time before they are modified again for one or two different applications [46]. In this context, custom-built 2PP systems, while potentially cheaper than commercial instruments, are not particularly suitable for microneedle development and clinical translation.

Despite SLA and DLP being cost-effective entry points for fabricating bio-inspired microneedles, both techniques often suffer from rough surfaces and poor shape accuracy. Specifi-

cally, SLA and DLP 3D printers suffer from the staircase effect, which is an artifact from slicing the computer-aided design (CAD) into layers [47,48]. The staircase effect leads to increased surface roughness of the order of micrometers, and high surface roughness on the microneedles will require substantially more pressure to penetrate the skin. These slicing artifacts ultimately impede quality control [49]. Finally, DLP- and SLA-fabricated microneedles are often dull with a low aspect ratio [50], and this again affects their performance (e.g., penetration).

Hence, 3D printing via 2PP is currently the best commercially available microfabrication method to enable miniaturization, shape accuracy, smooth surfaces, and high aspect ratios [51-54]. In the last decade, 2PP instruments have evolved from slow (albeit versatile) microfabrication instruments (e.g., the first generation 2008–2012 Photonic Professional) suitable for proofs of concept to industrialized 3D printers (e.g., Nanoscribe Quantum X platforms) producing polymer masters. The increased scan speed and throughput are the result of new supporting technologies coming to market, such as replacing piezoelectric stages with galvanometric mirrors. These new technologies continue to decrease the gap in volumetric throughput between DLP or SLA printers and 2PP instruments.

In conjunction with new hardware, there have also been incremental changes in 2PP fabrication strategies. These strategies are based on voxel (volumetric pixel in x,y,z) control. Current 2PP software can be utilized to classify parts of the structure for either fine or coarse slicing, such as Nanoscribe's "Smart Slicing" and "Shell & Scaffold" [55]. "Smart Slicing" can be applied to optimize print times for microneedle arrays by defining bulks areas, such as the base, with coarse slicing, and assigning finer slicing to the penetrating tips. "Shell & Scaffold" is leveraged to print hollow rather than solid structures, thereby polymerizing less internal volumes to speed up the printing process. Important to note, structures made by "Shell & Scaffold" require a post-development UV curing for a few minutes to polymerize the internal photoresin.

A third fabrication strategy leverages the combination of DLP and 2PP fabrication techniques. Sarker et al. [56] recently demonstrated the strength of combining fabrication techniques for microneedles. They used DLP to fabricate the bulky base and 2PP for microneedle fabrication, akin to Nanoscribe's "Smart Slicing" feature. All strategies, either software or combined fabrication methods, drastically reduce printing time and, ultimately, production cost.

Even with software and hardware advances, 2PP is still a layer-by-layer approach, similar to DLP and SLA, such that we see the staircase effect, albeit on a smaller scale. The staircase effect affects the surface quality and shape accuracy for complex geometries found in bio-inspired microneedles. It may also limit design freedom, such as the structural quality of overhanging features. Taking inspiration from similar challenges in microoptic fabrication, grayscale lithography offers a solution to mitigate the staircase effect. Grayscale lithography is a novel approach in photolithography for 2.5D patterning (x,y,z) with ultrasmooth surfaces that exhibits improved shape accuracy [57,58]. In 2019, Nanoscribe GmbH & Co launched the Quantum X platform that commercialized maskless grayscale lithography for microoptics made via 2PP, a process called "Two-Photon Grayscale Lithography" (2GL®) [59,60]. 2GL® differs from traditional 2PP and 1PP lithography because the laser or exposure dosage in individual voxels is controlled in three dimensions with high spatial resolution, which lends itself to continuous rather than discrete printing [59,61]. A key result of 2PP grayscale printing is that the technique is, on average, five to ten times faster than the common 2PP layer-by-layer approach [52]. Thiel et al. successfully applied 2GL® to free-standing 3D structures for the first time [62]. They also demonstrated that 3D printing by 2GL® was faster with better surface quality and shape accuracy than 2PP layer-by-layer methods [62]. Currently, Nanoscribe GmbH & Co is exploring 2GL® in three dimensions, and we look forward to the technique being commercially available to researchers and industry.

While microfabrication techniques have improved over the years in terms of cost, throughput, and quality, there is still a "valley of death" to cross when translating microneedle technologies from the lab to manufacturers. Specifically, proofs of concept require only a few pieces to be printed, compared to the millions or billions needed to be produced for a commercial product. For example, more than three billion people have received at least one COVID-19 vaccination [63]. Harro Höfliger and Vaxxas estimated that they would have had to produce tens of millions of Nanopatches per week for COVID-19 vaccination [64,65]. If companies were to personalize and optimize microneedles (including design, dosage, and vaccine composition) for COVID-19 or influenza vaccination based on ethnicities [66], those manufacturers would have to produce millions of pieces for each ethnic population.

Today, there are mass production methods using light-based 3D printing that mitigate the risks associated with scaling up production, namely (1) polymer masters for solid microneedle replication and (2) direct printing of hollow microneedles

The first approach to fabricate solid microneedles from polymer masters is more favorable for mass production because soft and

hard molds can be generated rapidly [50,67]. From these molds, medical device manufacturers can mass-produce drug-loaded microneedle arrays, which lowers the overall production cost [50]. The original polymer masters can be reused to generate new molds as necessary for production. Important to note, there are caveats regarding the lifetime of the polymer masters that depend on the exact replication technique, such as soft PDMS molding [68] or plastic microinjection molding [10]. The lifetime of a polymer master needs to be considered for the overall cost of production and product. Using polymer masters and mold techniques also follows accepted and well-established processes from regulatory bodies and manufacturers in adjacent medical market segments. This method also enables the production of either dissolving or non-dissolving drug-loaded microneedles.

The second approach is better suited for pure medical devices, that is, microneedles that are not loaded with drugs. While this article has not discussed the applications of hollow microneedles, it is worth mentioning that hollow microneedles are most often directly printed onto the medical device and aligned to specific features, such as pores, on the device. Direct microneedle printing has its own set of extensive requirements (e.g., biocompatibility of the material, mechanical robustness, and surface adhesion). Also, FDA's 510(k) criteria need to be considered early on in the conceptual phase. Furthermore, direct fabrication is more costly than creating molds from a polymer master, and the fabrication cost is a crucial factor when a new medical device is launched onto the market.

Conclusion

Microneedles are emerging as a new medical device for administering drugs and collecting biological fluids, all while reducing sharps-related risks to healthcare professionals. To date, microneedle patches are relatively simple with a one-size-fits-all approach, regardless of patient demographic and injection site. 3D microfabrication instruments enable the investigation of complex microneedle shapes and arrangements that can be personalized for patients. Microfabrication instruments based on 2PP can rapidly prototype bio-inspired microneedles and can be utilized in production. Importantly, using the same instrument for prototyping and production is advantageous for reducing design transfer and going to market faster. Microneedle fabrication is a rapidly evolving field that is overcoming traditional fabrication challenges and opening the door for personalized medicine.

Methods

All microneedle arrays in the presented images were 3D printed on a "Quantum X shape" lithography system (Nanoscribe GmbH & Co, Karlsruhe, Germany) following printing and post-printing protocols from NanoGuide. Post-printing protocols begin by removing unpolymerized material via two-step washing with either propylene glycol methyl ether acetate or mr-Dev for 15–20 min, followed by an isopropyl alcohol bath for 2–5 min. Afterwards, the microneedles were allowed to dry in air before UV curing for 20–40 min.

The microneedles were fabricated from proprietary and commercially available negative-tone IPX-Q and negative-tone IP-S with the medium (ZEISS 25x NA 0.8 objective) and large (ZEISS 10x NA 0.8 objective) feature sets. IPX-Q and IP-S are methacrylate photoresins; after polymerization, both materials are non-cytotoxic, as certified via external ISO-10993-5 commissioning.

IP-S is a photoresin optimized for printing smooth microoptics with the medium solution set (ZEISS 25x NA 0.8 objective). However, IP-S has been extensively used for microneedle molds and direct microneedle fabrication. IP-S is compatible with both Photonic Professional and Quantum X systems. IPX-Q is the newest formulation from the original IP-Q. It is optimized for printing 3D structures with the large solution set (ZEISS 10x NA 0.8 objective) on the Quantum X systems. IPX-Q is preferred over IP-S for microneedle applications as IPX-Q, on average, prints faster than IP-S. This is a result of the IPX-Q formulation being optimized for 3D structures.

Nanoscribe GmbH & Co is not a manufacturer of either medical devices or molds made from polymer masters. Users of the Nanoscribe Photonic Professional systems have extensively used IP-S and IP-Q for direct microneedle fabrication and molding. Given IPX-Q is the newest formulation of IP-Q, we expect similar results to those previously published.

We utilized Google Scholar to calculate the number of microneedle publications from 2015 to 2023 across different techniques. We did not include citations and patents in this search. For DLP and SLA microfabrication we used the keywords "microneedle DLP", "microneedle Digital Light Processing", "microneedle SLA", and "microneedle Stereolithography". Similarly, we used the following keywords for 2PP-fabricated microneedles: "microneedle 2-photon polymerization", "microneedle 2-photon polymerisation", "microneedle 2PP", "microneedle TPP", and "microneedle multiphoton lithography".

Acknowledgements

This article was supported by Nanoscribe GmbH & Co. We would like to thank Mr. Joerg Smolenski at Nanoscribe, Dr. Anton D. Sediako at ZEISS, and F.D. Valyn and F.D. Begemot for their editorial support.

ORCID® iDs

Remmi Danae Baker-Sediako - https://orcid.org/0000-0002-8901-4489

References

1. Deter-Wolf, A.; Peres, T. M.; Karacic, S. *J. Archaeol. Sci.: Rep.* **2021,** *37,* 103002. doi:10.1016/j.jasrep.2021.103002
2. Deter-Wolf, A.; Robitaille, B.; Krutak, L.; Galliot, S. *J. Archaeol. Sci.: Rep.* **2016,** *5,* 19–24. doi:10.1016/j.jasrep.2015.11.007
3. D'Alessandro, A.; Giardina, B.; Gevi, F.; Timperio, A. M.; Zolla, L. *Blood Transfus.* **2012,** *10* (Suppl. 2), s19–s24. doi:10.2450/2012.005s
4. Brunton, D. *J. R. Coll. Physicians Edinburgh* **2000,** *30,* 349–351. doi:10.1177/147827150003000414
5. Detamornrat, U.; McAlister, E.; Hutton, A. R. J.; Larrañeta, E.; Donnelly, R. F. *Small* **2022,** *18,* 2106392. doi:10.1002/smll.202106392
6. McLenon, J.; Rogers, M. A. M. *J. Adv. Nurs.* **2019,** *75,* 30–42. doi:10.1111/jan.13818
7. CDC. Sharps injury prevention workbook: workbook for designing, implementing, and evaluating a sharps injury prevention program. https://cdc.gov/sharpssafety/pdf/sharpsworkbook_2008.pdf (accessed Aug 1, 2023).
8. Bouya, S.; Balouchi, A.; Rafiemanesh, H.; Amirshahi, M.; Dastres, M.; Moghadam, M. P.; Behnamfar, N.; Shyeback, M.; Badakhsh, M.; Allahyari, J.; Al Mawali, A.; Ebadi, A.; Dezhkam, A.; Daley, K. A. *Ann. Global Health* **2020,** *86,* 35. doi:10.5334/aogh.2698
9. Wilburn, S. Q.; Eijkemans, G. *Int. J. Occup. Environ. Health* **2004,** *10,* 451–456. doi:10.1179/oeh.2004.10.4.451
10. Aldawood, F. K.; Andar, A.; Desai, S. *Polymers (Basel, Switz.)* **2021,** *13,* 2815. doi:10.3390/polym13162815
11. Gill, H. S.; Denson, D. D.; Burris, B. A.; Prausnitz, M. R. *Clin. J. Pain* **2008,** *24,* 585–594. doi:10.1097/ajp.0b013e31816778f9
12. Henry, S.; McAllister, D. V.; Allen, M. G.; Prausnitz, M. R. *J. Pharm. Sci.* **1998,** *87,* 922–925. doi:10.1021/js980042+
13. Fernando, G. J. P.; Hickling, J.; Jayashi Flores, C. M.; Griffin, P.; Anderson, C. D.; Skinner, S. R.; Davies, C.; Witham, K.; Pryor, M.; Bodle, J.; Rockman, S.; Frazer, I. H.; Forster, A. H. *Vaccine* **2018,** *36,* 3779–3788. doi:10.1016/j.vaccine.2018.05.053
14. Guillermet, E.; Alfa, D. A.; Phuong Mai, L. T.; Subedi, M.; Demolis, R.; Giersing, B.; Jaillard, P. *Vaccine* **2019,** *37,* 4435–4443. doi:10.1016/j.vaccine.2019.02.079
15. Fernando, G. J. P.; Zhang, J.; Ng, H.-I.; Haigh, O. L.; Yukiko, S. R.; Kendall, M. A. F. *J. Controlled Release* **2016,** *237,* 35–41. doi:10.1016/j.jconrel.2016.06.045
16. Ogunjimi, A. T.; Carr, J.; Lawson, C.; Ferguson, N.; Brogden, N. K. *Sci. Rep.* **2020,** *10,* 18963. doi:10.1038/s41598-020-75246-8
17. Ogunjimi, A. T.; Lawson, C.; Carr, J.; Patel, K. K.; Ferguson, N.; Brogden, N. K. *Skin Pharmacol. Physiol.* **2021,** *34,* 214–228. doi:10.1159/000515454
18. Laurent, A.; Mistretta, F.; Bottigioli, D.; Dahel, K.; Goujon, C.; Nicolas, J. F.; Hennino, A.; Laurent, P. E. *Vaccine* **2007,** *25,* 6423–6430. doi:10.1016/j.vaccine.2007.05.046
19. Kelchen, M. N.; Siefers, K. J.; Converse, C. C.; Farley, M. J.; Holdren, G. O.; Brogden, N. K. *J. Controlled Release* **2016,** *225,* 294–300. doi:10.1016/j.jconrel.2016.01.051
20. Kochhar, J. S.; Lim, W. X. S.; Zou, S.; Foo, W. Y.; Pan, J.; Kang, L. *Mol. Pharmaceutics* **2013,** *10,* 4272–4280. doi:10.1021/mp400359w
21. Tas, C.; Joyce, J. C.; Nguyen, H. X.; Eangoor, P.; Knaack, J. S.; Banga, A. K.; Prausnitz, M. R. *J. Controlled Release* **2017,** *268,* 159–165. doi:10.1016/j.jconrel.2017.10.021
22. Xie, X.; Pascual, C.; Lieu, C.; Oh, S.; Wang, J.; Zou, B.; Xie, J.; Li, Z.; Xie, J.; Yeomans, D. C.; Wu, M. X.; Xie, X. S. *ACS Nano* **2017,** *11,* 395–406. doi:10.1021/acsnano.6b06104
23. Rougier, A.; Dupuis, D.; Lotte, C.; Roguet, R.; Wester, R. C.; Maibach, H. I. *Arch. Dermatol. Res.* **1986,** *278,* 465–469. doi:10.1007/bf00455165
24. Enfield, J. G.; O'Connell, M.-L.; Lawlor, K.; Jonathan, E.; O'Mahony, C.; Leahy, M. J. *J. Biomed. Opt.* **2010,** *15,* 046001. doi:10.1117/1.3463002
25. Nguyen, T. T.; Park, J. H. *Expert Opin. Drug Delivery* **2018,** *15,* 235–245. doi:10.1080/17425247.2018.1410138
26. Milewski, M.; Brogden, N. K.; Stinchcomb, A. L. *Expert Opin. Drug Delivery* **2010,** *7,* 617–629. doi:10.1517/17425241003663228
27. Donnelly, R. F.; Singh, T. R. R.; Woolfson, A. D. *Drug Delivery* **2010,** *17,* 187–207. doi:10.3109/10717541003667798
28. Makvandi, P.; Maleki, A.; Shabani, M.; Hutton, A. R. J.; Kirkby, M.; Jamaledin, R.; Fang, T.; He, J.; Lee, J.; Mazzolai, B.; Donnelly, R. F.; Tay, F. R.; Chen, G.; Mattoli, V. *Matter* **2022,** *5,* 390–429. doi:10.1016/j.matt.2021.11.021
29. Cordeiro, A. S.; Tekko, I. A.; Jomaa, M. H.; Vora, L.; McAlister, E.; Volpe-Zanutto, F.; Nethery, M.; Baine, P. T.; Mitchell, N.; McNeill, D. W.; Donnelly, R. F. *Pharm. Res.* **2020,** *37,* 174. doi:10.1007/s11095-020-02887-9
30. Dabbagh, S. R.; Sarabi, M. R.; Rahbarghazi, R.; Sokullu, E.; Yetisen, A. K.; Tasoglu, S. *iScience* **2021,** *24,* 102012. doi:10.1016/j.isci.2020.102012
31. Faraji Rad, Z.; Prewett, P. D.; Davies, G. J. *Manuf. Lett.* **2021,** *30,* 39–43. doi:10.1016/j.mfglet.2021.10.007
32. Mizuno, Y.; Takasawa, K.; Hanada, T.; Nakamura, K.; Yamada, K.; Tsubaki, H.; Hara, M.; Tashiro, Y.; Matsuo, M.; Ito, T.; Hikima, T. *Biomed. Microdevices* **2021,** *23,* 38. doi:10.1007/s10544-021-00576-x
33. Jaffar-Bandjee, M.; Casas, J.; Krijnen, G. *Curr. Opin. Insect Sci.* **2018,** *30,* 79–85. doi:10.1016/j.cois.2018.09.011
34. Liu, S.; Chu, S.; Banis, G. E.; Beardslee, L. A.; Ghodssi, R. Biomimetic barbed microneedles for highly robust tissue anchoring. In *2020 IEEE 33rd International Conference on Micro Electro Mechanical Systems (MEMS),* IEEE, 2020; pp 885–888.
35. McBride, C. S.; Baier, F.; Omondi, A. B.; Spitzer, S. A.; Lutomiah, J.; Sang, R.; Ignell, R.; Vosshall, L. B. *Nature* **2014,** *515,* 222–227. doi:10.1038/nature13964
36. Ramasubramanian, M. K.; Barham, O. M.; Swaminathan, V. *Bioinspiration Biomimetics* **2008,** *3,* 046001. doi:10.1088/1748-3182/3/4/046001
37. Kong, X. Q.; Wu, C. W. *J. Bionic Eng.* **2009,** *6,* 143–152. doi:10.1016/s1672-6529(08)60111-0
38. Suzuki, M.; Sawa, T.; Takahashi, T.; Aoyagi, S. *Int. J. Automation Technol.* **2015,** *9,* 655–661. doi:10.20965/ijat.2015.p0655
39. Bae, W.-G.; Ko, H.; So, J.-Y.; Yi, H.; Lee, C.-H.; Lee, D.-H.; Ahn, Y.; Lee, S.-H.; Lee, K.; Jun, J.; Kim, H.-H.; Jeon, N. L.; Jung, W.; Song, C.-S.; Kim, T.; Kim, Y.-C.; Jeong, H. E. *Sci. Transl. Med.* **2019,** *11,* eaaw3329. doi:10.1126/scitranslmed.aaw3329
40. Faraji Rad, Z.; Nordon, R. E.; Anthony, C. J.; Bilston, L.; Prewett, P. D.; Arns, J.-Y.; Arns, C. H.; Zhang, L.; Davies, G. J. *Microsyst. Nanoeng.* **2017,** *3,* 17034. doi:10.1038/micronano.2017.34
41. Bagheri, A.; Jin, J. *ACS Appl. Polym. Mater.* **2019,** *1,* 593–611. doi:10.1021/acsapm.8b00165
42. Waheed, S.; Cabot, J. M.; Macdonald, N. P.; Lewis, T.; Guijt, R. M.; Paull, B.; Breadmore, M. C. *Lab Chip* **2016,** *16,* 1993–2013. doi:10.1039/c6lc00284f

43. Pagac, M.; Hajnys, J.; Ma, Q.-P.; Jancar, L.; Jansa, J.; Stefek, P.; Mesicek, J. *Polymers (Basel, Switz.)* **2021,** *13,* 598. doi:10.3390/polym13040598
44. Li, L.; Fourkas, J. T. *Mater. Today* **2007,** *10,* 30–37. doi:10.1016/s1369-7021(07)70130-x
45. Pisanello, M.; Zheng, D.; Balena, A.; Pisano, F.; De Vittorio, M.; Pisanello, F. *PLoS One* **2022,** *17,* e0265678. doi:10.1371/journal.pone.0265678
46. Pearre, B. W.; Michas, C.; Tsang, J.-M.; Gardner, T. J.; Otchy, T. M. *Addit. Manuf.* **2019,** *30,* 100887. doi:10.1016/j.addma.2019.100887
47. Unkovskiy, A.; Schmidt, F.; Beuer, F.; Li, P.; Spintzyk, S.; Kraemer Fernandez, P. *J. Clin. Med.* **2021,** *10,* 1070. doi:10.3390/jcm10051070
48. Janusziewicz, R.; Tumbleston, J. R.; Quintanilla, A. L.; Mecham, S. J.; DeSimone, J. M. *Proc. Natl. Acad. Sci. U. S. A.* **2016,** *113,* 11703–11708. doi:10.1073/pnas.1605271113
49. Vitale, A.; Cabral, J. T. *Materials* **2016,** *9,* 760. doi:10.3390/ma9090760
50. Krieger, K. J.; Bertollo, N.; Dangol, M.; Sheridan, J. T.; Lowery, M. M.; O'Cearbhaill, E. D. *Microsyst. Nanoeng.* **2019,** *5,* 42. doi:10.1038/s41378-019-0088-8
51. Faraji Rad, Z.; Prewett, P. D.; Davies, G. J. *Microsyst. Nanoeng.* **2021,** *7,* 71. doi:10.1038/s41378-021-00298-3
52. Aderneuer, T.; Fernández, O.; Ferrini, R. *Opt. Express* **2021,** *29,* 39511–39520. doi:10.1364/oe.440251
53. Bunea, A.-I.; del Castillo Iniesta, N.; Droumpali, A.; Wetzel, A. E.; Engay, E.; Taboryski, R. *Micro* **2021,** *1,* 164–180. doi:10.3390/micro1020013
54. Niesler, F.; Hermatschweiler, M. *Laser Tech. J.* **2015,** *12,* 44–47. doi:10.1002/latj.201500019
55. Marschner, D. E.; Pagliano, S.; Huang, P.-H.; Niklaus, F. *Addit. Manuf.* **2023,** *66,* 103474. doi:10.1016/j.addma.2023.103474
56. Sarker, S.; Colton, A.; Wen, Z.; Xu, X.; Erdi, M.; Jones, A.; Kofinas, P.; Tubaldi, E.; Walczak, P.; Janowski, M.; Liang, Y.; Sochol, R. D. *Adv. Mater. Technol. (Weinheim, Ger.)* **2023,** *8,* 2201641. doi:10.1002/admt.202201641
57. Grushina, A. *Adv. Opt. Technol.* **2019,** *8,* 163–169. doi:10.1515/aot-2019-0024
58. Smith, M. A.; Berry, S.; Parameswaran, L.; Holtsberg, C.; Siegel, N.; Lockwood, R.; Chrisp, M. P.; Freeman, D.; Rothschild, M. *J. Micro/Nanolithogr., MEMS, MOEMS* **2019,** *18,* 043507. doi:10.1117/1.jmm.18.4.043507
59. Bertoncini, A.; Tanguy, Y.; Tungal, A.; Lindenmann, N.; Sartor, T.; Reiner, R.; Blaicher, M.; Fisher, S.; Taghdiri, M.; Niesler, F. B.; Radke, A.; Thiel, M. Advancement in two-photon grayscale lithography. In *3D Printed Optics and Additive Photonic Manufacturing III,* 2020; PC1213501.
60. Rodríguez, S. *PhotonicsViews* **2020,** *17,* 36–39. doi:10.1002/phvs.202000003
61. Gonzalez-Hernandez, D.; Varapnickas, S.; Bertoncini, A.; Liberale, C.; Malinauskas, M. *Adv. Opt. Mater.* **2023,** *11,* 2201701. doi:10.1002/adom.202201701
62. Thiel, M.; Bertoncini, A.; Hoose, T.; Blaicher, M. Advancement in two-photon grayscale lithography. In *Advanced Fabrication Technologies for Micro/Nano Optics and Photonics XVI,* SPIE, 2023; PC124330B.
63. Rashedi, R.; Samieefar, N.; Masoumi, N.; Mohseni, S.; Rezaei, N. *J. Med. Virol.* **2022,** *94,* 1294–1299. doi:10.1002/jmv.27463
64. Creelman, B.; Frivold, C.; Jessup, S.; Saxon, G.; Jarrahian, C. *Drug Delivery Transl. Res.* **2022,** *12,* 368–375. doi:10.1007/s13346-021-01076-4
65. Weiss, P. *Engineering (Beijing, China)* **2021,** *7,* 1661–1664. doi:10.1016/j.eng.2021.11.010
66. Jethwa, H.; Wong, R.; Abraham, S. *Vaccine* **2021,** *39,* 3541–3543. doi:10.1016/j.vaccine.2021.05.017
67. Nguyen, T. T.; Oh, Y.; Kim, Y.; Shin, Y.; Baek, S.-K.; Park, J.-H. *Hum. Vaccines Immunother.* **2021,** *17,* 316–327. doi:10.1080/21645515.2020.1767997
68. Pillai, M. M.; Ajesh, S.; Tayalia, P. *MethodsX* **2023,** *10,* 102025. doi:10.1016/j.mex.2023.102025

License and Terms

This is an open access article licensed under the terms of the Beilstein-Institut Open Access License Agreement (https://www.beilstein-journals.org/bjnano/terms), which is identical to the Creative Commons Attribution 4.0 International License (https://creativecommons.org/licenses/by/4.0). The reuse of material under this license requires that the author(s), source and license are credited. Third-party material in this article could be subject to other licenses (typically indicated in the credit line), and in this case, users are required to obtain permission from the license holder to reuse the material.

The definitive version of this article is the electronic one which can be found at:
https://doi.org/10.3762/bjnano.14.70